Doctoral Dissertation

博士論文

Understanding Atmospheric Escape of Hot Jupiters Using Radiation Hydrodynamics Simulations

（輻射流体シミュレーションを用いたホットジュピターの大気散逸過程の理解）

A Dissertation Submitted for the Degree of Doctor of Philosophy

December 2022

令和4年12月博士（理学）申請

Department of Physics, Graduate School of Science,
The University of Tokyo

東京大学大学院 理学系研究科物理学専攻

Hiroto Mitani

三谷　啓人

Abstract

About 5000 exoplanets have been discovered since the first discovery of the exoplanet around a sun-like star in 1995. There are many exoplanets that are not analogous to our solar system. Hot Jupiters are close-in gas giant planets. In order to understand planetary systems in general, including planets in our solar system, it is necessary to understand the formation and evolutionary processes of such close-in planets. Due to the intense UV light from the host star, the upper atmosphere of hot Jupiters hydrodynamically escapes. Such an escape process has a significant impact on the evolution of close-in planets. In order to comprehend the thermo-chemical structure of the atmosphere and atmospheric escape, detailed radiation hydrodynamics models are required. We can study transit signatures to track these escape outflows. Lyman-α transit absorption is a useful tracer of the atmospheric escape of hot Jupiters. Theoretically, radiation hydrodynamics simulations are needed to understand the structure of the outflow from the observational transit signals.

The radiation hydrodynamics simulation is used to comprehend the composition and structure of the upper atmosphere. Classical theoretical models have investigated the extreme-ultraviolet radiation as a dominant heating process. We investigate far-ultraviolet as another heating process. We find that far-ultraviolet heating is significant in planets around hot stars. The classical photoionization heating drives the escape around cooler stars, such as solar type stars. Our results suggest that the close-in planets around hot stars experience intense mass loss and evolve very differently from the typical hot Jupiters. Far-ultraviolet heating may be an origin of the observed paucity of low-mass, close-in planets around relatively hot stars.

We also study the observational signals of the atmospheric escape. In order to interpret the observational signals of the planetary outflow, it is necessary to understand the geometry of the outflow. Stellar winds from the host star can change the shape of the outflow. We perform hydrodynamics simulations of the planetary outflow with the strong stellar wind in a self-consistent manner. We find that the Lyman-α absorption depth due to the outflow strongly depends on the strength of the wind because the strong stellar wind can confine the atmosphere. Interestingly, the mass-loss rate is almost independent of the wind. We also investigate Hα absorption which can be observed by ground-based telescopes. We find that the Hα transit depth is almost independent of the wind strength because the lower layers of atmosphere contribute to the absorption. Our results suggest that the observations of both lines are useful to determine the stellar wind parameters and the high energy ultraviolet flux around planets. We also discuss the effect of time-dependent stellar activities on the observational signals.

Finally, we study the physics which dominates the structure of the upper atmosphere and the escape. We introduce the relevant temperatures and timescales of the planetary gravity, the photoheating, and the gas expansion. We clarify the physical conditions that classify the atmospheric escape. One of the conditions relates to the transition point between the energy-limited and the recombination-limited regime which are the classification of the atmospheric mass loss driven by UV radiation. We also calculate the planetary evolution with the mass loss of the atmospheric escape due to the UV heating and find that the mass loss regime changes with the evolution of the planet and the host star.

Contents

Chapter 1

Introduction

1.1 Discovery of close-in exoplanets

Since the first discovery of an exoplanet around a sun-like star (Mayor and Queloz 1995), observations have discovered about 5000 exoplanets (Figure 1.1), revealing a diversity of exoplanets that are not analogous to our solar system. Before the first discovery, we only knew the solar system as a planetary system and the theory of formation and evolution focused on the solar system (Kyoto model, Hayashi et al. 1985). After the discovery of exoplanets such as close-in gas giant planets, we knew the diversity of the planetary system and found that the previous classical theory was not sufficient.

Among the exoplanets discovered, close-in gas giants are called hot Jupiters. The first discovered exoplanet, 51 Pegasi b, is a hot Jupiter. The name comes from the high surface temperature due to the intense radiation from the host star. The orbital separation of hot Jupiters is typically about 0.05 AU and the orbital period is about less than 10 days. Although there is no strict definition of mass, a planet with a mass greater than 0.1 Jupiter mass ($> 0.1\,M_J$) is called a hot Jupiter, and a planet with a mass of 0.03-0.1 ($0.03 - 0.1\,M_J$) Jupiter mass ($M_J = 1.898 \times 10^{30}\,\mathrm{g}$, from https://ssd.jpl.nasa.gov/planets/phys_par.html) is called a hot Neptune. Most hot Jupiters are tidally locked, with the same side facing to the host star. Hot Jupiters are known to have large radii relative to their mass, but the reason for this is not known. Understanding their formation and evolution is important for understanding the origin of planetary systems in general, including our solar system.

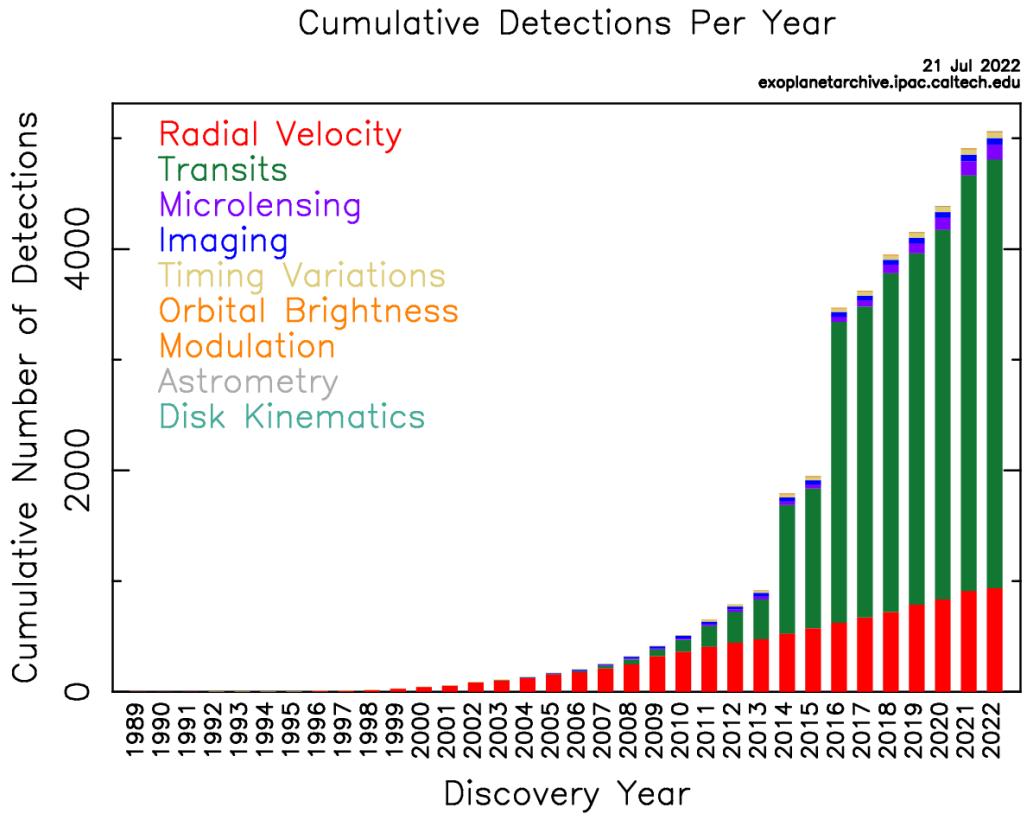

Fig 1.1: The cumulative number of planets discovered versus the year of discovery. The color represents the detection method. The data are taken from https://exoplanetarchive.ipac.caltech.edu/index.html.

Not only the giant planets but also the small rocky planets have been discovered (e.g. *Kepler* mission, Borucki et al. 2011; Dressing and Charbonneau 2015). The environments of such planets may be habitable for life (e.g. TRAPPIST-1 system, Gillon et al. 2017). Some rocky planets have been found in a habitable zone where the liquid water can exist (Gillon et al. 2017). The formation and evolution of such small planets may be influenced by the presence of close-in gas giants. In this sense, the formation and evolution process of hot Jupiters are fundamental objects also in the context of astrobiology.

Such close-in planets can be detected by transit methods (e.g. HD 209458 b, Henry et al. 2000; Charbonneau et al. 2000; Castellano et al. 2000). There are many other methods to detect exoplanets. For example, the radial velocity method uses the variation of the

radial velocity of the star due to the presence of planets. This method is also common in observations of exoplanets and was used to discover of the first exoplanet around the sun-like star (51 Pegasi b, Mayor and Queloz 1995). We can know the mass of the planet from the radial velocity. As we can see in Figure 1.1, most of the planets have been discovered using the transit method or the radial velocity. The recent development of the observation allows us to detect exoplanets by direct imaging (Lagrange et al. 2010), but the number of direct imaging detections is still small because the low contrast makes it difficult to detect the planets.

We focus on the transit method in this thesis because of the high detectability of close-in planets. The transit method uses the fact that the observed flux from the host star decreases as the planet crosses in front of the star (Figure 1.2). We can see that the Kepler space telescope (NASA) has detected $\sim$ 3000 planets using the transit method.

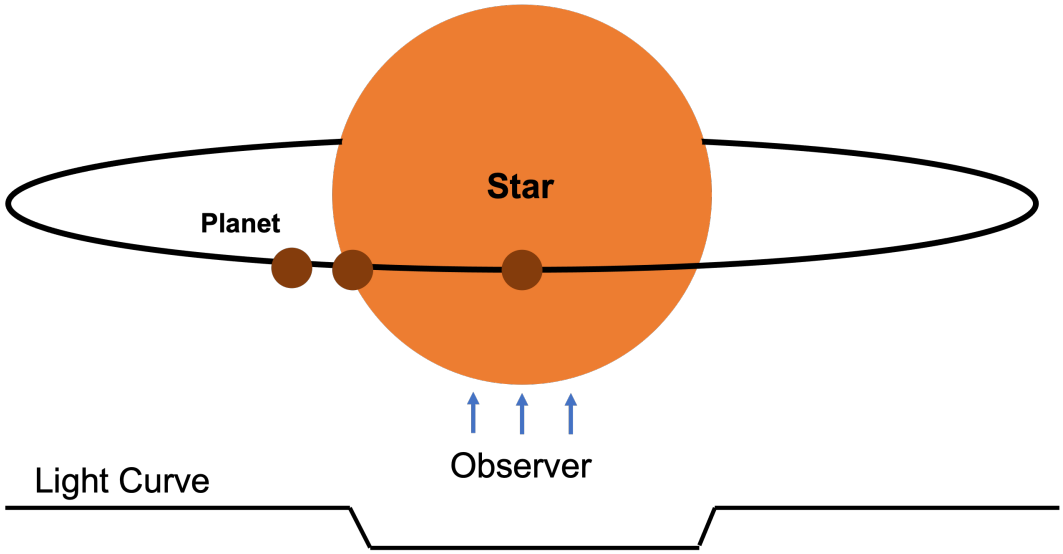

Fig 1.2: The schematic figure of the transit method. The light curve of the star changes due to the transiting planets. When a planet crosses in front of a star, the flux from the star decreases periodically.

1.2 Statistical properties of exoplanets

There are many discovered exoplanets and we can use the statistical properties of exoplanets to understand their formation and evolution. The metallicity dependence of hot

Jupiters is one of the most important features. In the context of astronomy, the term "metal" refers to elements heavier than helium (such as carbon, oxygen, and iron). The metallicity Z is defined as the mass ratio of elements other than hydrogen and helium. The mass ratio of hydrogen and helium are also denoted as X, Y. These values satisfy $X + Y + Z = 1$. The solar values are $X_\odot = 0.7381, Y_\odot = 0.2485, Z_\odot = 0.0134$ from the recent observations (Asplund et al. 2009), mainly from the solar spectroscopy and the modeling of the photosphere. The metallicity of stars is sometimes given as the ratio of the abundance of iron and hydrogen in the star compared to the ratio of iron and hydrogen in the sun as:

$$[\mathrm{Fe/H}] = \log(\mathrm{Fe/H})_* - \log(\mathrm{Fe/H})_\odot \tag{1.1}$$

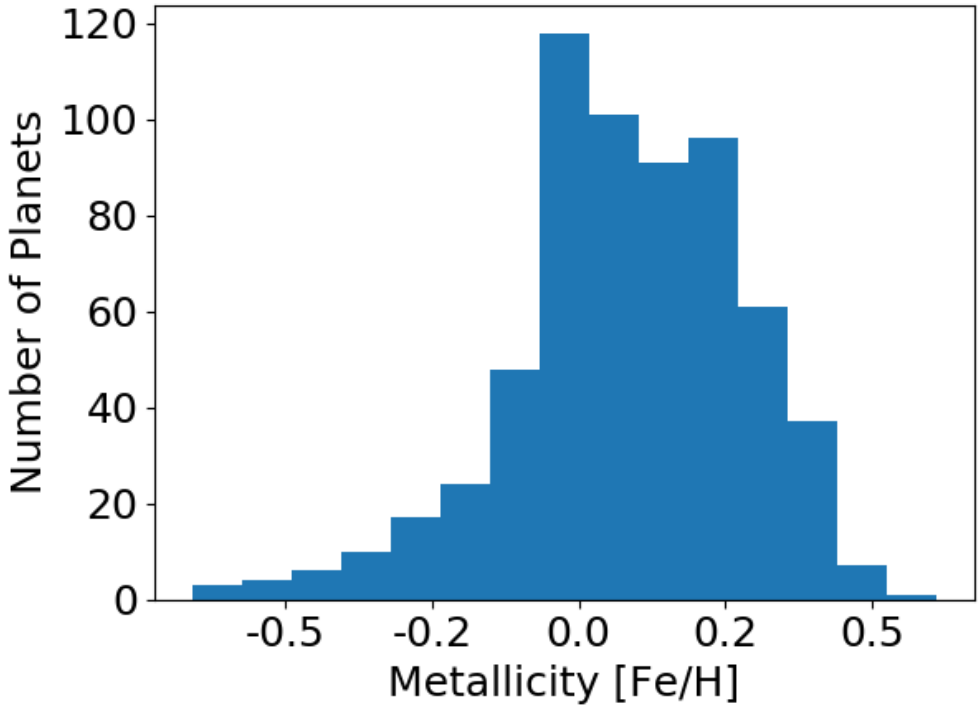

Fig 1.3: Metallicity distribution of hot Jupiter host stars.

For the star with the same metallicity as the sun, $[\mathrm{Fe/H}] = 0$. Metallicity is an impor-

tant property of the host star and the planet-metallicity correlation has been extensively investigated in many studies (Gonzalez 1997; Laughlin 2000; Mortier et al. 2013). Figure 1.3 shows the metallicity distribution of hot Jupiter host stars. Metal-rich stars tend to have hot Jupiters. The metallicity correlation can be explained by the self-enrichment or by planetary formation in the protoplanetary disk. In the self-enrichment scenario, the accretion of rocky material due to the migration of hot Jupiters pollutes the surface of the host star. In the planetary formation scenario, giant planets may form more easily in the metal-rich protoplanetary disk. The results of the recent studies have supported the protoplanetary disk origin scenario (Johnson et al. 2010; Adibekyan 2019).

The democracy of the exoplanets is helpful in understanding how the environment affects the planetary evolution and formation. We note that the observational bias and/or the correlation of parameters can be an origin of the statistical properties. For example, young stars are born in the metal-rich environments, and thus the young stars tend to have high metallicity. The planet-metallicity correlation in hot Jupiters may be a result of the age-metallicity correlation. According to the recent study, both the metallicity and the age of the host star affect the occurrence rate of the hot Jupiters. The relatively high occurrence rate of observed hot Jupiters around young stars (Hamer and Schlaufman 2019) suggests that planetary evolution affects the democracy of hot Jupiters. One of the possible scenario is orbital decay. Hot Jupiters can lose the angular momentum within the lifetime of their host stars. The large transit depth of hot Jupiters is useful for observing and testing theoretical models of the atmosphere.

1.3 Atmosphere of close-in planets

Detailed transit spectroscopy allows us not only to detect the existence of planets but also to study the physical and chemical quantities of the planets and the structure of the atmosphere (e.g. Charbonneau et al. 2002). The wavelength dependence of the transit depth reflects the atmospheric thermo-chemical structure of the atmosphere, such as the atmospheric composition and the temperature profile. The chemical composition is related to the formation and the evolution process. Hydrogen dominates the gas composition of the protoplanetary disk similar to the composition of the solar photosphere. The composition of the atmospheres of rocky planets such as the earth is different from that of the sun. The primordial atmosphere may have similar composition because the gas of the protoplanetary disk accretes onto the planet. In the case of relatively low-mass planets (rocky planets), the planets lose the primordial atmosphere. In the case of the gas giants, the hydrogen

dominates the atmosphere because they can retain much of the primordial atmosphere.

The upper atmosphere of the close-in planets is heated by the intense radiation from the host star and escapes hydrodynamically (Watson et al. 1981). The hydrodynamic escape is a key process in the atmospheric evolution. Such an escaping atmosphere has been observed using the transit method (Vidal-Madjar et al. 2004). We need the theoretical atmospheric structure to obtain the mass-loss rate of the planets from the transit light curve. Detailed hydrodynamics simulations with photochemistry of the atmospheric escape are needed to understand the planetary evolution and the observed transit signature. The chemical composition of the atmosphere is difficult to determine because we cannot determine the composition by the simple chemical equilibrium for some species. In the case of the chemical equilibrium, we can obtain the number density of each species by minimizing the Gibbs free energy. However, the photochemistry and advection make the composition more complex. In this sense, the hydrostatic calculation is not sufficient.

As observations have progressed, the statistical properties of exoplanets have become clearer, and many have been studied in the context of planetary formation and evolution. We are now able to link physical models to observed planetary properties, not only for individual planets, but also for planets in general. In the case of the close-in planets, the escape process has a significant impact on the evolution. It is necessary to reveal the detailed structure of the upper atmosphere of hot Jupiters by hydrodynamics simulations before further UV observations by future space telescopes.

1.4 Aims and structure of the dissertation

In this thesis, we perform radiation hydrodynamics simulations of the atmospheric escape of close-in planets to understand the thermo-chemical structure of the upper atmosphere and the observational transit signals. We review the basics of the atmospheric escape and the observational signature in Chapter 2. We introduce the problems in the previous theoretical models and observations that cannot be explained by the classical models.

We describe our radiation hydrodynamics model in Chapter 3. In Chapter 3, we focus mainly on the far-ultraviolet (FUV) radiation heating process which determines the atmospheric escape rate of hot Jupiters around hot stars. The classical models have only considered extreme-ultraviolet (EUV) radiation and have not dealt with the FUV heating. We use the detailed radiation hydrodynamics simulations with FUV heating to investigate the atmospheric structure of exoplanets around hot stars that emit intense FUV radiation. The aim of the Chapter 3 is to understand the mass loss in hot Jupiters in general.

The shape of the escaping atmosphere depends not only on stellar radiation but also on the stellar wind. The hydrodynamics simulations with the stellar wind are essential for the interpretation of the observational transit signals. There are some previous theoretical studies of the effect of the stellar wind on the atmosphere. Many of the previous studies have not calculated the structure of the planetary outflow and the wind simultaneously or have not followed the multi-dimensional effect (Christie et al. 2016; Esquivel et al. 2019; Matsakos et al. 2015; Schneiter et al. 2016; Vidotto and Cleary 2020; Villarreal D'Angelo et al. 2014, 2021). Our model investigates the interplay between the wind and the planetary atmosphere using self-consistent hydrodynamics simulations. We discuss the model with the wind in Chapter 4. We can use the model to study the escaping outflow that absorbs the stellar radiation. We develop the models about not only for the mass loss but also for the outflow structure with the stellar wind effect. We also study the wind effect on the Hα transit absorption which has been observed by recent ground-based telescopes but has not been investigated by theoretical models. We propose a combination of observational transit signals that can be used to understand the stellar wind and the high-energy ultraviolet from the host stars.

We discuss the relevant physics of the upper atmosphere and the classification of the observed close-in planets in terms of the physical conditions governing the escape of the atmosphere in Chapter 5. There are many theoretical simulations of the atmospheric escape of close-in planets. The physical conditions that determine the strength of the planetary atmospheric escape and the observed transit signals are not clear. We first derive the physical conditions for the atmospheric escape. We apply our theoretical framework to the observed close-in planets and investigate the underlying physics of the observed atmospheric escape process. We also investigate the planetary mass and orbital evolution in Chapter 5. The aim of Chapter 5 is to understand the atmospheric structure of the simulations based on physics.

Chapter 2

Atmospheric escape of exoplanets

In this chapter, we review the atmospheric escape processes in exoplanets. The mass loss due to the atmospheric escape alters the planetary evolution. An understanding of such escape processes is necessary to understand the observed statistical properties that may reflect the evolution and formation process of planetary systems. In the previous chapter, the huge number of discovered planets makes it possible to investigate the statistical properties as an essential tool. The escape process is a key process in the planetary evolution especially for the close-in planets. We also explain the problems of the classical theoretical models revealed by recent observations.

2.1 Basics of atmospheric escape

Planets lose their atmospheres through many processes. We review the theoretical and observational understanding of the thermal escape processes in this section. Non-thermal processes can be important in some planetary atmospheres. For example, the charge exchange process where a collision between an ion and an atom transfers the kinetic energy to the atom dominates the hydrogen loss in the earth. There are many possible non-thermal escape processes and they play a critical role in particularly cooler planets and heavier elements. In such environments, elements cannot escape by thermal processes because of their higher mass and lower thermal energy. Many observed exoplanets are close-in, and the heating by the intense radiation from the host star is significant. The atmospheric evolution and the structure of the outflow are dominated by the thermal processes. We focus on the thermal processes in this thesis.

2.1.1 Jeans escape

Atoms and molecules in the upper atmosphere can escape if the velocity exceeds the escape velocity.

$$\sqrt{\frac{2kT}{m}} > \sqrt{\frac{2GM_p}{R_p}} \tag{2.1}$$

where k is Boltzmann's constant, T is the gas temperature, m is the mass of atoms or molecules, M_p is the planetary mass and R_p is the planetary radius. This escaping process is called hydrostatic escape (Jeans escape, Jeans 2009; Catling and Zahnle 2009). Such escape process can be occurred at the point where the mean free path equals to the scale height as:

$$\frac{1}{\sigma_a n_a} \sim \frac{kT}{mg} \tag{2.2}$$

where σ_a is the collisional cross section, n_a is the number density, and g is the planetary gravitational acceleration. In the case of hydrogen at earth, the temperature is $T \sim 1000$ K and the cross section is $\sigma_{\rm H} \sim 4.5 \times 10^{16}\,{\rm cm}^2$. The density at the exobase becomes $n_{\rm H} \sim 3 \times 10^7\,{\rm cm}^{-3}$.

We can define the escaping parameter as:

$$\lambda = \frac{GM_p m}{kTR_p} \tag{2.3}$$

This parameter is the ratio of the gravitational potential and the thermal energy. In the case of the Jeans escape, $\lambda \gg 1$.

In reality, the particles in the high velocity tail of a Maxwell distribution can escape. The escaping flux Φ can be calculated by integrating over the Maxwell distribution $f(v)dv$ (Seager and Deming 2010; Tian 2015).

$$\Phi = \int_{v_{\rm esc}}^{\infty}\int_0^{2\pi}\int_{\pi/2}^{0} f(v)\cos\theta\sin\theta d\theta d\phi dv \tag{2.4}$$

$$= \frac{nv_{\rm th}}{2\sqrt{\pi}}\left(\frac{v_{\rm esc}^2}{v_{\rm th}^2}+1\right)\exp\left(-\frac{v_{\rm esc}^2}{v_{\rm th}^2}\right) \tag{2.5}$$

$$\propto \sqrt{1/T_{\rm exo}}\exp\left(-\frac{GM_p m}{kT_{\rm exo}r_{\rm exo}}\right) \tag{2.6}$$

where the subscript *exo* represents the physical quantities at the exobase where the particles are collisionless due to the low density as expressed in the above equation, and v_{th} is the thermal velocity. If we consider the hydrogen escape in the earth, we can find that the

escape flux is $\Phi \sim 10^{10}\,\mathrm{cm^{-2}\,s^{-1}}$ and the mass-loss rate is $\dot{M}_{\mathrm{H}} \sim 10^5\,\mathrm{g/s}$. Diffusion is a bottleneck for the real hydrogen escape in the earth because it limits the downward supply of hydrogen. The mass-loss rate is larger than the real value. We can also find that the Jeans escape is negligible for heavier elements because the thermal velocity is low. For example, the thermal velocity of oxygen atoms is about one fourth of that of hydrogen atoms and the exponential term becomes very small.

We can apply the same procedure for hot Jupiters $M_p = M_J, R_p = 10^{10}\,\mathrm{cm}, T = 10000\,\mathrm{K}$. The density is $n_{\mathrm{H}} = 4 \times 10^6\,\mathrm{cm^{-3}}$ and the mass-loss rate is $\dot{M}_p \sim 10^4\,\mathrm{g/s}$. This value is quite smaller than that of hydrodynamic escape rate in the next section. Previous studies have also investigated the effect of the Jeans escape in the context of hot Jupiters (Lecavelier des Etangs et al. 2004). They have found that the Jeans escape rates were not large enough to have an effect on the planetary evolution.

2.1.2 Hydrodynamic escape

Intense radiation from the host star heats the upper atmosphere and the gas expansion causes the escape. In this process, the planetary gravity cannot stop the hydrodynamic outflow. We will introduce the detailed heating and cooling processes that determine the thermo-chemical structure of the atmosphere and the escaping process. Typically, Extreme-Ultraviolet (EUV;$> 13.6\,\mathrm{eV}$) radiation is a dominant heating source in the upper atmosphere because the upper atmosphere is optically thin for ultraviolet in many cases. EUV photons photoionize hydrogen atoms and the photoelectrons thermalize into the gas by the reaction:

$$\mathrm{H} + h\nu(>13.6\,\mathrm{eV}) \longrightarrow \mathrm{H^+} + \mathrm{e^-} \tag{2.7}$$

Not only hydrogen atoms but also metal atoms provide photoelectrons and contribute to the heating. In this thesis we focus on the gas giants whose upper atmosphere consists of mostly hydrogen atoms and we only consider the photoionization heating due to the hydrogen.

The hydrodynamic outflow is similar to the solar corona as discussed by Parker 1958. The velocity of the outflow becomes supersonic at a critical point. If we consider the isothermal outflow, the critical point is given by

$$r_s \sim \frac{GM_p}{2c_s^2} \tag{2.8}$$

where c_s is the sound speed. The continuity equation and the equation of motion can be

given as:

$$4\pi r^2 \rho v = const \tag{2.9}$$

$$v\frac{dv}{dr} + \frac{1}{\rho}\frac{dp}{dr} = -\frac{GM_p}{r^2} \tag{2.10}$$

where we assume spherical symmetry. From these equations, we have

$$\frac{1}{v}\frac{dv}{dr}\left(1 - \frac{v^2}{c_s^2}\right) = \frac{2r_s}{r^2} - \frac{2}{r} \tag{2.11}$$

and this equation has a transonic solution as:

$$\log\frac{v}{c_s} - \frac{1}{2}\frac{v_2}{c_s^2} + \frac{2r_s}{r} + 2\log\frac{r}{r_s} = \frac{3}{2} \tag{2.12}$$

And we can derive the density profile from the continuity equation:

$$\rho = \rho_s \exp\left(\frac{2r_s}{r} - \frac{3}{2} - \frac{v^2}{2c_s^2}\right) \tag{2.13}$$

In this solution, the velocity of the gas v is subsonic at $r < r_s$ and becomes supersonic at $r > r_s$. In the case of the solar wind, the velocity reaches the sonic speed at $r_s \sim 8 \times 10^6$ km. In the above equations, we assume the isothermal but the temperature of the real atmosphere depends on the altitude because of the cooling by the radiation and the gas expansion.

It is important for understanding the evolution of close-in planets to estimate the mass-loss rate due to the hydrodynamic escape. Classically the simple well-known equation of the mass-loss rate equation below (Watson et al. 1981) is widely used for planetary population synthesis models:

$$\dot{M} = \pi\frac{\epsilon F_{EUV} R_p R_{EUV}^2}{GM_p} \tag{2.14}$$

where ϵ is the efficiency, F_{EUV} is the EUV flux, and R_{EUV} is the effective planetary radius for EUV where the optical depth $\tau_{\rm EUV}$ becomes ~ 1. The heating efficiency is about 10% and does not exceed 25% (Ionov and Shematovich 2015). In the case of the Earth, the EUV flux is about 1 erg/s/cm^2. The flux is proportional to the inverse square of the orbital separation a^{-2} and $\sim$ 400erg/s/cm^2 for close-in planets with the semi-major axis $a = 0.05$ AU. Such a system to which this formula can be applied is characterized as an energy-limited system.

From the formula, we can see that the hydrodynamic escape becomes significant for close-in (the EUV flux is larger) and low-mass (the planetary gravity is weak) planets. The

effect of the stellar gravity is sometimes also considered in some studies (Erkaev et al. 2007) because the outflow does not need to escape to infinity, but need to escape the outside of the planetary Roche lobe. The corrected mass-loss rate is given by

$$\dot{M} = \pi \frac{\epsilon F_{EUV} R_p^3}{G M_p K} \tag{2.15}$$

where K is the parameter which accounts for the tidal effect. Erkaev et al. 2007 showed that K can be approximated as:

$$K = 1 - \frac{3}{2\epsilon_k} + \frac{1}{2\epsilon_k^3} \tag{2.16}$$

$$\epsilon_k = \frac{R_{\rm Roche}}{R_p} \tag{2.17}$$

where $R_{\rm Roche} \sim a(M_p/3M_*)^1/3$ is the Roche lobe radius. The formula assumes that the efficiency is independent of the stellar and planetary properties. In reality, this assumption is not correct for high F_{EUV} planets. For such planets, the photoionization and recombination rates are in equilibrium and the system becomes recombination-limited. In this case, the density at the $\tau_{EUV} = 1$ base is $m_{\rm H} n_{\rm HII}$ and the ionization-recombination equilibrium can be written as

$$\Phi_{\rm EUV} \sigma_0 n_{\rm HI} \sim n_{\rm HII}^2 \alpha_{\rm rec} \tag{2.18}$$

where $\alpha_{\rm rec}$ is the Case B recombination coefficient (Storey and Hummer 1995) and σ_0 is the photoionization cross section of neutral hydrogen atoms. As a result, the mass-loss rate for the planet with $M_p = 0.7 M_J, R_p = 1.4 R_J$ can be given as:

$$\dot{M} \sim 4 \times 10^{12} \left(\frac{F_{\rm EUV}}{5 \times 10^5 \,{\rm erg\,cm^{-2}\,s^{-1}}} \right)^{1/2} {\rm g\,s^{-1}} \tag{2.19}$$

There are many theoretical models to investigate the hydrodynamic escape of hot Jupiters (Lammer et al. 2003; Yelle 2004; García Muñoz 2007; Murray-Clay et al. 2009; Tripathi et al. 2015). The physical conditions that separate the two regimes, the energy-limited and the recombination-limited, will be explained in Chapter 5. We will also construct the analytical model of the escape due to the EUV heating including the stellar gravitational effect in the later part of the thesis.

Heavier elements can also escape by being carried with the outflow, in contrast to the Jeans escape. This process dominates the mass-loss rate of close-in planets. The stellar surface activities are related to the EUV emission, and the EUV flux from the photosphere

is small for many stars. The chromospheric and coronal emission dominate the high-energy flux from the solar-type star (Güdel 2004; Jardine et al. 2006). The EUV flux determines the mass-loss rate of close-in planets but it is difficult to determine the flux from observations. In general, young stars are active and the mass loss due to the EUV flux is significant in young systems. The observational study has revealed the relationships between the stellar age and the EUV luminosity $L_{\rm EUV}$ (erg/s) as shown in Sanz-Forcada et al. 2011.

$$\log L_{\rm EUV} = (29.12 \pm 0.11) - (1.24 \pm 0.15) \log \tau \tag{2.20}$$

where τ is the stellar age in Gyr. If we assume the mass-loss rate can be written as in Equation 2.15, $\int \dot{M} dt \propto \tau^{-0.24}$. The intense photoevaporation takes place in young systems and the accumulated mass loss is dominated by the mass loss in young age. The X-ray luminosity is also used to estimate the EUV luminosity, since it is related to the stellar surface activity. The X-ray luminosity of very young stars can be given as Jackson et al. 2012:

$$\frac{L_X}{L_{bol}} = \begin{cases} (L_X/L_{bol})_{sat} & (t < t_{sat}) \\ (L_X/L_{bol})_{sat}(t/t_{sat})^{-\alpha} & (t > t_{sat}) \end{cases} \tag{2.21}$$

where L_X, L_{bol} are the X-ray luminosity and the bolometric luminosity of the stars and $(L_X/L_{bol})_{sat}$ is the X-ray to bolometric luminosity ratio at the stellar age $t = t_{sat}$. They found that $t_{sat} \sim 10^8$year, $\alpha \sim 1.2$ in FGK stars. EUV luminosity is difficult to observe but it may be saturated in very young stars such as pre-main-sequence stars. In the planets of the early solar system, the hydrodynamic escape thus may be important and dominant in mass-loss rates. In the early Venus, the hydrodynamic escape of hydrogen may occur because of the high water mixing ratio and the intense high-energy flux from the young sun (Kulikov et al. 2006). It is also important to note that in such cases, in contrast to the Jeans escape, heavy elements such as oxygen may also be dragged by the escaping outflow of hydrogen atoms and alter the evolution of the atmospheric composition of early rocky planets.

Far-ultraviolet (FUV; < 13.6 eV) photons can also heat the atmosphere but this effect has not yet been investigated. The stellar FUV luminosity depends strongly on the spectral type of the star. The stellar spectrum can be approximated by blackbody radiation, but differs slightly from blackbody radiation due to absorption and emission in the stellar atmosphere. The contribution of the chromosphere to the FUV is dominant for cool stars, and the photosphere dominates in hot stars (Figure 2.1). The FUV luminosity of 10000 K stars is 4-5 orders of magnitude larger than that of solar-like stars. The FUV heating may

be important for close-in planets around a hot star but has not been studied because of the small number of such planets. Such planets around hot stars have been found in recent observations (e.g. KELT 9b; Gaudi et al. 2017, KELT-20b; Lund et al. 2017) and detailed radiation hydrodynamics simulations are needed to reveal the escape process in such an extreme environment. We introduce FUV photoheating processes in the upper atmosphere of hot Jupiters and the hydrodynamics simulations with the FUV heating processes in the Chapter 3.

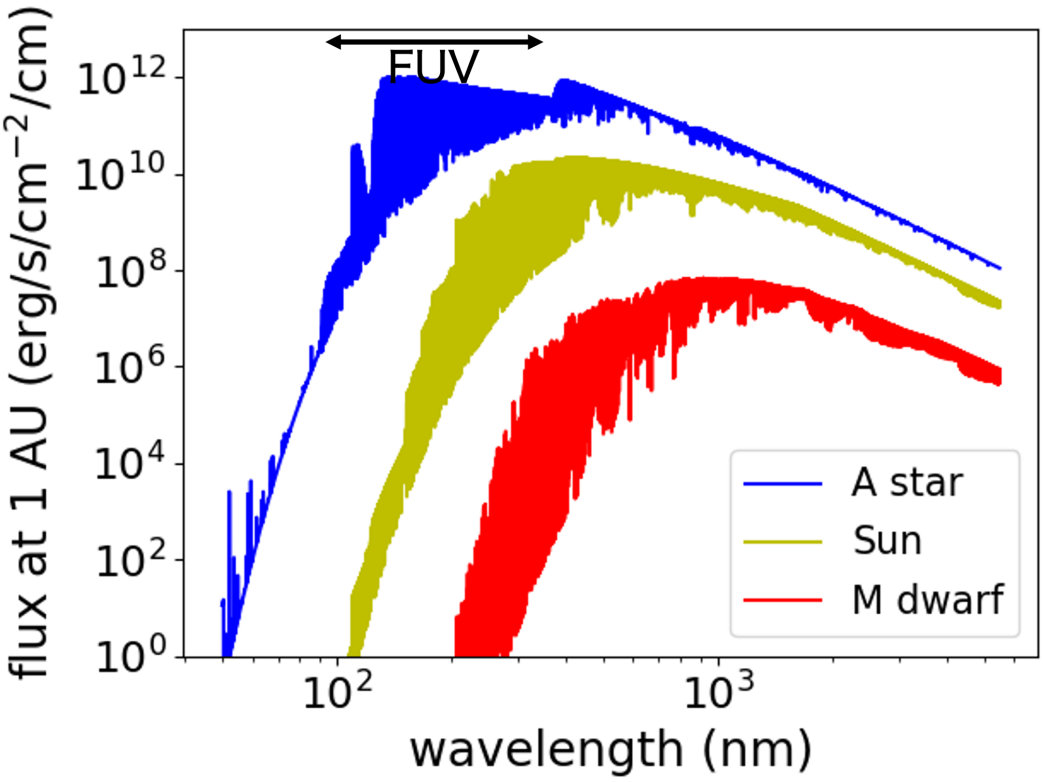

Fig 2.1: Stellar photospheric spectra of a hot star at 1AU (Blue, $T_{\rm eff} = 10000\,{\rm K}$), a solar-type star (Yellow, $T_{\rm eff} = 5800\,{\rm K}$), and a cool star (Red, $T_{\rm eff} = 3000\,{\rm K}$) at 1 AU. The arrow shows the range of FUV wavelength (6eV - 13.6 eV). The spectra is calculated the data from Husser et al. 2013.

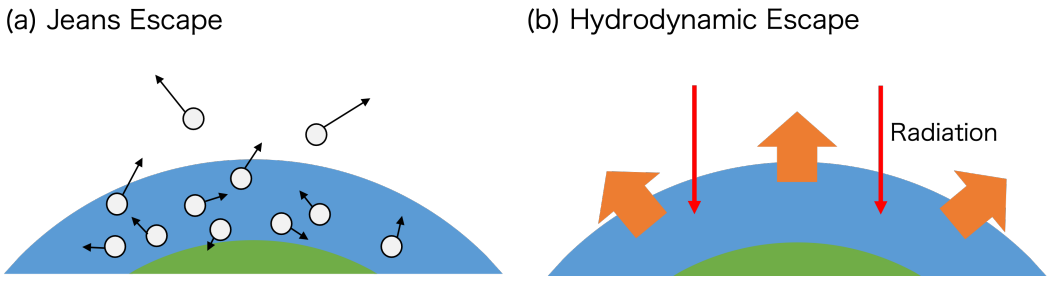

Fig 2.2: Schematic figures of thermal escape processes. In (a) Jeans escape, some particles with enough velocity can escape but particles in lower atmosphere cannot escape due to the collisions. In (b) hydrodynamic escape, the gas expansion due to the radiation heating drives the escaping outflow.

2.1.3 Magnetic field effect

The planetary magnetic field can affect the escaping outflow because the outflow can be highly ionized due to the photoionization of hydrogen atoms by the intense EUV radiation from the host star (Trammell et al. 2014). If the planet has a strong dipole magnetic field and the field is closed at low latitudes, the atmosphere can escape only at high latitudes where the field is open. Owen and Adams 2014 has introduced a dimensionless parameter that represents the ratio between the ram pressure of the outflow and the magnetic field pressure as:

$$\Lambda_p = \frac{2\dot{M}_p v}{B_p^2 r^2} \tag{2.22}$$

$$\sim 2\times10^{-4}\times\left(\frac{\dot{M}_p}{10^{10}\,\mathrm{g/s}}\right)\left(\frac{v_p}{10\,\mathrm{km/s}}\right)\left(\frac{B_p}{1\,\mathrm{G}}\right)^{-2} \times\left(\frac{R_p}{10^{10}\,\mathrm{cm}}\right)^{-2}\left(\frac{r}{R_p}\right)^{4} \tag{2.23}$$

where v_p is the velocity of the outflow and B_p is the planetary magnetic field at the surface. When the planetary magnetic field is strong enough $B_p > 0.1$G, the outflow is controlled not only by stellar UV heating but also by the planetary magnetic field. In such a strong magnetic field environment, the mass-loss rates of planets are reduced by about an order of magnitude (Owen and Adams 2014; Khodachenko et al. 2015). We will focus on the non-magnetized environments due to the uncertainty of the magnetic field of exoplanets. The shape and the strength of the magnetic field of exoplanets are still unknown but should

be investigated by detailed magnetohydrodynamics simulations with radiative transfer in future studies.

2.2 Transit observations of atmospheric escape

Not only the planet itself but also the existence of the atmospheric escape can be observed using the transit method. The effective radius of a planet depends on the observed wavelength and we can use the different wavelengths to follow the vertical structure of the atmosphere. The extended atmosphere beyond the Roche radius represents the existence of the escape. If the escaping atmosphere outside the Roche lobe absorbs the stellar photons, then the transit depth becomes

$$\delta > \left(\frac{R_{\rm Roche}}{R_*}\right)^2 \tag{2.24}$$

The absorption due to the extended atmosphere can be detected in some lines. The Lyman-α line flux from the host star is commonly used to detect such an extended atmosphere because of its large transit depth. Such Lyman-α absorption was first detected by Vidal-Madjar et al. 2003 in HD209458b after its first discovery by the transit method. The absorption is also detected in the Neptune-mass planet GJ436b (Ehrenreich et al. 2015). The Lyman-α transit depth is large because the cross-section $\sigma_{{\rm Ly}\alpha} = 6 \times 10^{-14}\,{\rm cm}^{-2}$ (Hansen and Oh 2006) is large and the density at the point where the optical depth becomes unity can be given as:

$$n_{\rm HI} \sim \frac{1}{\sigma_{{\rm Ly}\alpha} R_p} \sim 2 \times 10^2\,{\rm cm}^{-3} \left(\frac{R_p}{R_J}\right)^{-1} \tag{2.25}$$

In some observations, the absorption due to the tail-like escaping atmosphere after the transit has been observed (Bourrier and Lecavelier des Etangs 2013; Ehrenreich et al. 2015). Figure 2.3 shows a schematic picture of the absorption of the escaping atmosphere and the transit spectrum. The Lyman-α from the host star is absorbed by neutral hydrogen gas in the interstellar medium (ISM) in its line center and we cannot detect the transit in the center but can detect only the absorption in the blue/red wing. Typically, the significant absorption can be seen at $\sim 100\,{\rm km\,s}^{-1}$ in the transit. The typical sound speed of the $10^4\,{\rm K}$ gas is $\sim 10\,{\rm km\,s}^{-1}$ and the acceleration mechanisms are required. There are two possible mechanisms to explain such high-velocity absorption. One is the radiation pressure from the host star. Some simulations have succeeded to reproduce the high-velocity absorption (Bourrier and Lecavelier des Etangs 2013; Beth et al. 2016). Another scenario is the charge

exchange with the stellar wind. The high-energy protons in the wind become rapid neutral hydrogen atoms through the charge exchange process. Some hydrodynamics simulations show that both charge-exchange and the radiation pressure are important to explain the observed absorption signals (Tremblin and Chiang 2013; Bourrier et al. 2016). The details of the line spectrum are not well understood and the origin of the acceleration is still unknown. Detailed radiation hydrodynamics simulations of the planetary outflow can reveal the origin. The Lyman-α observations have revealed the post-transit absorption due to the absorption of the escaping atmosphere and such absorption after transit is the evidence for the tail-like structure of the neutral hydrogen atmosphere.

Recent observations have also revealed the non-detection of the Lyman-α absorption in close-in planets that may receive the intense EUV radiation (Rockcliffe et al. 2021). The existence of such systems suggests that the planet has already lost the primordial hydrogen and helium atmosphere, or that some unknown factors prevent the absorption by the outflow (e.g. high EUV flux also photoionizes the escaping neutral hydrogen or strong stellar wind confines the escaping outflow).

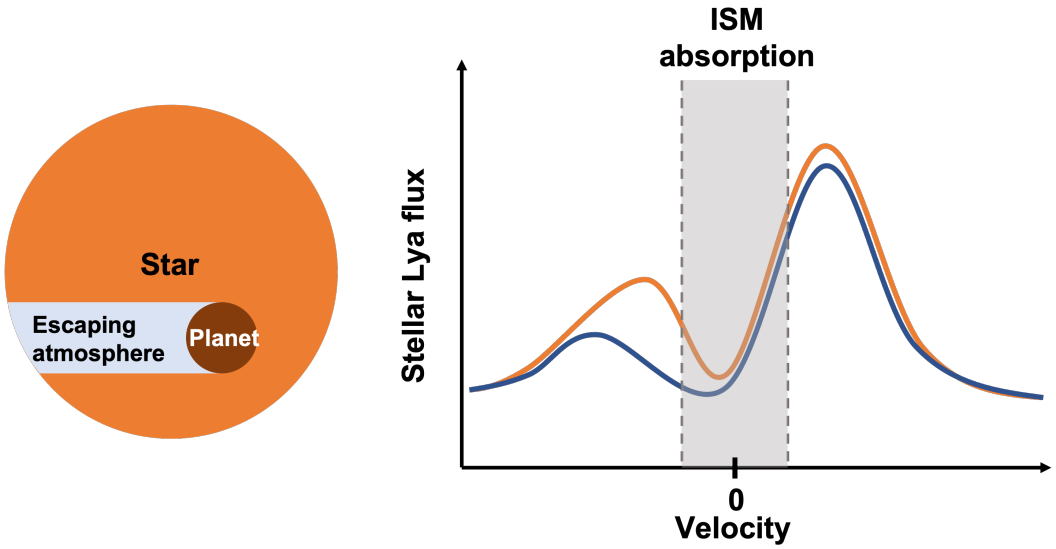

Fig 2.3: Schematic figure of the transiting planet with escaping atmosphere (left) and the Lyman-α transit observations (right). The blue curve shows the Lyman-α flux from the star before the transit and the orange curve shows the flux during transit and after transit. In the line center, the ISM absorbs the stellar flux (shaded region).

The Lyman-α line emission is difficult to observe in many systems although the transit depth itself is large because the space telescope is required. Recently, some other lines have been proposed to study atmospheric escape. Helium transits become major for searching the escaping atmosphere. The 10833 Å absorption due to the excited metastable helium has been proposed (Oklopčić and Hirata 2018) and used for this purpose. The 10833 Å photons excite helium atoms to the 2^3S level of which the transition probability is low because the radiative decay is forbidden. The important point is that we can measure the absorption using ground-based telescopes rather than space telescopes and high-resolution spectroscopy may be possible. Transit observations of these lines sometimes do not directly detect the escaping atmosphere but provide the information about the escaping atmosphere. We also explain more details and discuss the helium line in the later chapter. Other UV metal lines also show large transit depths in close-in planets (e.g. OI and CII in HD209458b Vidal-Madjar et al. 2004) and can be used to study the structure of the upper atmosphere.

2.3 The effects of atmospheric escape on the planetary evolution

The atmospheric escape process is important for understanding the evolution of close-in exoplanets. The mass loss due to the escape changes the planetary mass evolution and affects the democracy in the case of close-in planets.

Recent observations have found that the number of close-in planets with radius $R_p \sim 1.5R_\oplus - 2R_\oplus$ is small. This statistical property is called the photoevaporation valley and the atmospheric escape process can be an origin of the bimodality. Figure 2.4 shows the size distribution of the planets. We can find the scarcity of planets with $R_p \sim 2R_\oplus$. We have removed some planets as discussed in Fulton et al. 2017 to avoid contamination of less well-observed planets. We removed the planets with host large magnitude ($m > 14.2$) of the host star and with a long orbital period ($P < 100$ day). We also removed planets with the large impact parameter $b > 0.7$ because the uncertainty of the planetary radius increases due to the influence of the limb-darkening when b is large. The total number of filtered planets in the figure is 1062.

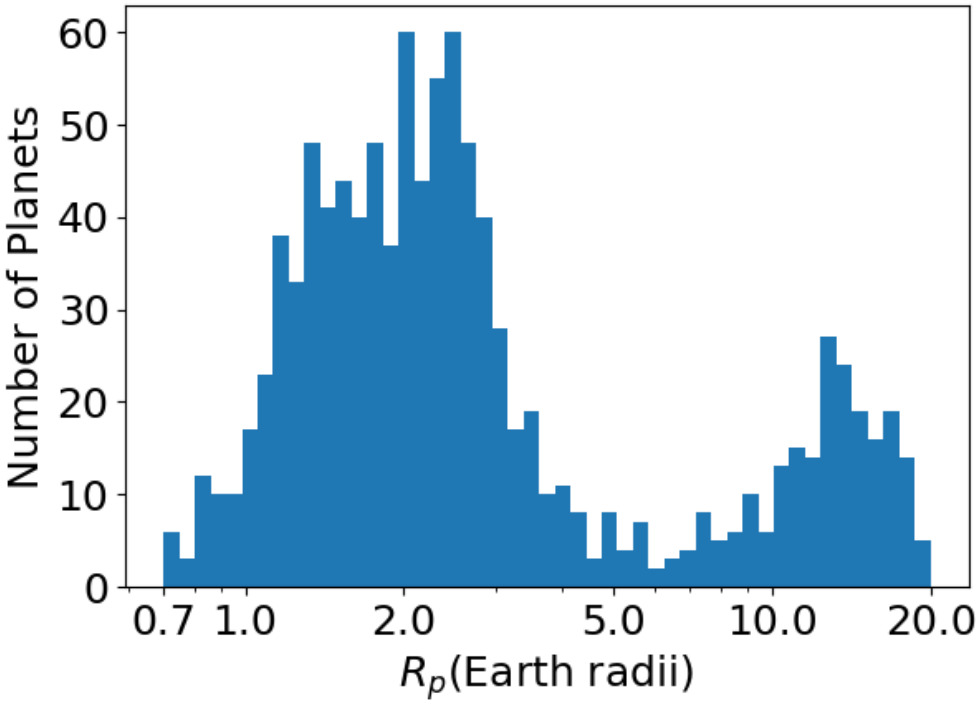

Fig 2.4: Size distribution of planets. The valley exists around $R_p \sim 2R_\oplus$. The number of filtered planets is 1062.

Some studies (Owen and Wu 2013, 2017; Owen 2019) have argued that this valley can be explained by the hydrodynamic escape due to the UV heating. They found that the mass-loss timescale $M_{atm}/\dot{M}_p$ as a function of the atmospheric mass fraction $f = M_{atm}/M_p$ has a local minimum around $f \sim 1$ and a local maximum around $f \sim 0.01$. When the atmospheric mass fraction f is large enough, the atmosphere doubles the planetary radius and increases the absorption of the UV flux. The mass loss timescale then becomes short. This trend continues until the self-gravity of the atmosphere can reduce the radius. The number of planets around $f \sim 1$ is small due to the short timescale. Recently, the core-powered mass loss has also been proposed as the origin (Ginzburg et al. 2018; Gupta and Schlichting 2019; Gupta et al. 2022). In the core-powered scenario, the heat due to the planetary formation drives the escape. This process also drives hydrodynamic escape but

the driving heating source is different from the classical hydrodynamic escape. There are two regimes in the core-powered mass loss. The first regime is the energy-limited regime and the mass-loss rate can be given as:

$$\dot{M}^{E}_{core} \sim \frac{L_{rcb}}{gR_p} \tag{2.26}$$

where L_{rcb} is the planetary luminosity at the radiative-convective boundary R_{rcb}. As the core of planet cools, the mass-loss rate above becomes small. In the Bondi-limited regime, the mass-loss rate is given as:

$$\dot{M}^{B}_{core} = 4\pi R_s^2 c_s \rho_{rcb} \exp\left(-\frac{GM_p}{c_s^2 R_{rcb}}\right) \tag{2.27}$$

The minimum value of the two mass-loss rates is the physical upper limit of the mass-loss rate of the core-powered mass loss. It is difficult to distinguish between the effect of the UV-driven escape and the core-powered mass loss because the mass-loss rate in both scenarios depends on the stellar luminosity. The main difference is that the core-powered mass loss can be significant in the young planets and the classical escape due to UV heating can explain the existence of the outflow around old planets. We will focus on the classical hydrodynamic escape and neglect the core-powered mass loss because the observed transit signals are detected not only in young systems but also in old systems.

The impact of the atmospheric escape is also important in the evolution of the Jupiter-mass giant planets (Kurokawa and Nakamoto 2014). The strong gravity of the giant planets suppresses the intense mass loss, and the planets may not lose entire of the atmosphere during the host star's lifetime. In the case of relatively low-mass planets, the mass loss process has a strong influence on the evolution.

The probability of a transit can be written as

$$\mathrm{P(transit)} \sim \frac{R_*}{a} \propto P^{-2/3} \tag{2.28}$$

and we may find more short period planets due to the observational bias. However, we notice a dearth of planets with mass $M_p < M_J$ and short period $P < 5$ day (Figure 2.5, Szabó and Kiss 2011; Mazeh et al. 2016). This implies the planetary formation/evolution in such systems reduce the probability of the existence.

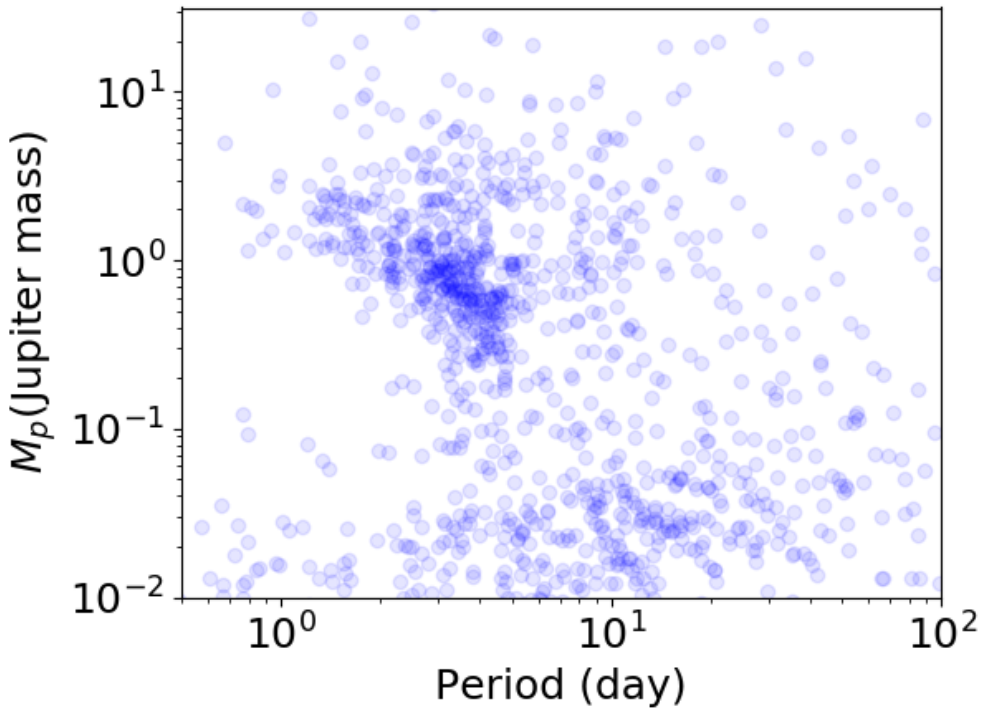

Fig 2.5: The observed close-in exoplanets in the period-mass plane. The desert exists around relatively light($M_p < M_J$) and short period (less than a few days).

Recent studies show that the statistical properties of close-in planets depend on the temperature and metallicity of the host star (Szabó and Kálmán 2019). The boundary of the desert depends on the temperature of the host star. In the case of cool host stars, the boundary of the period is around 9 days, and 21 days in the hot stars. The metallicity also has an impact on the desert. Around the desert, three-quarters of the planets are found around high-metallicity stars and have short orbital periods ($\sim$ 10 days). Low-metallicity planets tend to have longer periods. These stellar temperature and metallicity dependencies are found around the desert and are not found outside of the desert. These features suggest that the stellar temperature and metallicity are important parameters that determine the formation and evolution of planets and that the observational bias may not be the origin.

The EUV luminosity weakly depends on the stellar temperature, and the photoioniza-

tion heating rate is independent of the metallicity of the systems because the photoionization of hydrogen atoms itself is independent of the metal elements. The metal elements can cool the atmosphere by radiative coolings and reduce the effective heating rate. The previous outflow models with EUV photoionization are not sufficient to understand the mass-loss process. The radiation hydrodynamics simulations with FUV heating are necessary to understand the general systems.

2.3.1 The effects of the atmospheric escape on the planetary orbital evolution

The mass loss due to the intense radiation has impact on not only the planetary mass evolution but also on the orbital evolution of close-in planets (Jackson et al. 2016; Fujita et al. 2022). The orbital angular momentum can be given as

$$L \sim M_p \sqrt{G M_* a} \tag{2.29}$$

and the time derivative of L is given as

$$\frac{\dot{L}}{L} = \frac{\dot{M}_p}{M_p} + \frac{1}{2}\frac{\dot{a}}{a} \tag{2.30}$$

We can find that the time derivative is positive and that the planetary orbit expands with time. If we assume the time derivative of the angular momentum of the system as $\dot{L} = (1-\chi)\dot{M}_p a^2 \Omega$, we obtain

$$\frac{\dot{a}}{a} \sim -2\chi\frac{\dot{M}_p}{M_p} - (1-\chi)\frac{\dot{M}_p}{M_*} \tag{2.31}$$

We can see that the time derivative is positive regardless of the parameter $0 < \chi < 1$. The parameter χ represents the fraction of the angular momentum conserved in the system and depends on the geometry of the escaping outflow. We can neglect the mass loss of the host star during the main sequence whose mass loss is not significant. Note that as the star evolves and the mass loss becomes significant, the orbital expansion due to the change in the stellar mass becomes important. If we assume the typical hot Jupiter $M_p = M_J, \dot{M}_p = 10^{11} g/s, a = 0.05\,\mathrm{AU}$ around a solar type star $M_* = M_\odot$ and $\chi = 0.5$, the time scale of the migration is about 6×10^{11} year. Thus, this type of migration is not significant in the typical hot Jupiters. The mass loss due to EUV photoionization heating leads to $\sim 10\%$ orbital expansion in Gyr in the case of the super earth.

The escaping atmosphere may accumulate and form a torus around the host star. The mass of the torus can be given as:

$$M_t = 2\pi \int drr\Sigma \tag{2.32}$$

where Σ is the surface density of the torus. The theoretical calculation has found that the surface density around the planet is about $\sim 0.01\,\mathrm{g\,cm^{-2}}$ (Kurbatov and Bisikalo 2021). The tidal interaction between the torus and the planet also plays an important role in the orbital evolution. This migration is similar to the migration in the protoplanetary disk which might be the origin of the formation of close-in gas giant planets. In addition to the mass-loss effect in the above equation, such a tidal interaction may cause the migration of close-in planets.

The time derivative of angular momentum can be written using the tidal torque τ (Papaloizou and Terquem 2006) as:

$$\dot{L} = -2\pi \int_{r'}^{\infty} drr\Sigma\tau \tag{2.33}$$

$$\tau = \frac{C_0}{\pi} \frac{G^2 M_p^2 a}{(r'-a)^2} \frac{\Omega_p - \Omega}{(a\Omega_p - r'\Omega)^3} \tag{2.34}$$

The 1D simulation has found that the initial orbit 0.3 AU may become 0.047 AU through the tidal interaction. We will discuss such orbital evolution with mass loss due to the photoionization heating in the upper atmosphere in Chapter 5. This type of migration has a significant effect on the orbital evolution of close-in gas giant planets that can supply enough sufficient gas to the torus, but may not be important for rocky planets that cannot retain a primordial atmosphere. To understand the statistical properties of hot Jupiters, detailed models of orbital evolution with the planetary mass loss and the torus due to the accumulation of the atmospheric escape are also required.

2.4 Summary

We summarize the current understanding of the atmospheric escape in exoplanets. There are many possible escape processes, but hydrodynamic escape is a dominant process for close-in planets. In this process, the heating in the upper atmosphere due to the intense radiation from the host star drives the hydrodynamic outflow. The outflow structure and the mass-loss rate depend on the UV radiation. Previous studies have focused on the EUV

photoionization heating of hydrogen atoms. FUV heating has not been investigated, but it can be significant around hot stars which emit intense FUV radiation from the photosphere.

We can observe the escaping outflow from their transit signatures. The Lyman-α absorption is a classical line absorption to observe the existence of the outflow. The large cross-section allows us to detect the thin upper atmosphere. The absorption signal can be detected even after the transit of some close-in planets, indicating the existence of the outflow. Recent observations have found the close-in planets with Lyman-α non-detection. The origin of such non-detection and the quantitative condition that determines the physics and the existence of absorption are still unknown.

The atmospheric escape process is a key process for understanding the observed properties of exoplanets and determines the evolution of the close-in planets. The sub-Jupiter desert and the radius valley are thought to be the result of the mass loss due to the UV radiation from the host star. The radiative hydrodynamics simulation gives us the detailed thermo-chemical structure to investigate the observational signals and the mass-loss rates that determine the planetary evolution.

Chapter 3

Radiation hydrodynamics simulations of the escaping process with FUV heating

In this chapter, we describe our radiation hydrodynamics simulations of the atmospheric escape of hot Jupiters. We discuss the effect of FUV heating on the atmospheric escape in this chapter. FUV heating may be significant in close-in planets around hot stars which have been discovered recently. The multi-dimensional radiation hydrodynamics simulations in Chapter 3 and Chapter 4 were carried out on Cray XC50 at Center for Computational Astrophysics, National Astronomical Observatory of Japan.

3.1 Methods: Radiation hydrodynamics simulations of atmospheric escape of hot Jupiters

We develop the radiation hydrodynamic code with multi-species chemistry (Nakatani et al. 2018a,b; Mitani et al. 2020, 2022) using the public hydrodynamic code PLUTO (Mignone et al. 2007). Our code is also used for other objects (e.g. protoplanetary disks, Nakatani et al. 2018a,b, minihalos, Nakatani et al. 2020). We summarize the implemented physics in our code. We choose a hot Jupiter around a hot A-star as a fiducial setting to investigate intense FUV heating effect on the atmospheric escape and the planetary evolution (Table 3.1). Recent observations have found such exoplanets, such as KELT-9b. In the case of KELT-9b, the temperature of the host star is about 10000 K. We assume 2D axisymmetry in our simulation to follow the structure and to save computational cost. In the radiation hydrodynamics simulations, we have to solve the hydrodynamic equations with

the radiative transfer. The equations are

$$\frac{\partial \rho}{\partial t} + \nabla \cdot \rho \vec{v} = 0 \tag{3.1}$$

$$\frac{\partial \rho v_R}{\partial t} + \nabla \cdot (\rho v_R \vec{v}) = -\frac{\partial P}{\partial R} - \rho \frac{\partial \Psi}{\partial R} \tag{3.2}$$

$$\frac{\partial \rho v_z}{\partial t} + \nabla \cdot (\rho v_z \vec{v}) = -\frac{\partial P}{\partial z} - \rho \frac{\partial \Psi}{\partial z} \tag{3.3}$$

$$\frac{\partial E}{\partial t} + \nabla \cdot (H \vec{v}) = -\rho \vec{v} \cdot \nabla \Psi + \rho(\Gamma - \Lambda) \tag{3.4}$$

where $\rho, \vec{v}, P, \Psi$ are gas density, velocity, pressure, and gravitational potential of the star and planet including the centrifugal force term. We configure plane-parallel stellar radiation coming from the negative z direction (Figure 3.1). Because the mass of the upper atmosphere is considerably lower than that of the planet, we ignore its self-gravity. The relevant heating (Γ) and the cooling (Λ) rates which change the total energy and enthalpy of the gas per unit volume E, H. We also follow non-equilibrium chemistry

$$\frac{\partial n_H y_i}{\partial t} + \nabla \cdot (n_H y_i \vec{v}) = n_H R_i \tag{3.5}$$

where $y_i = n_i / n_H$ and R_i represent the abundance and the reaction rate, respectively. The implemented reactions and their rates are given in Table 3.2. The potential is given as:

$$\Psi = -\frac{GM_p}{r} - \frac{GM_*}{r_*} - \frac{1}{2}\frac{GM_* r_*^2}{a^3} \tag{3.6}$$

We use the equation of state

$$e = \frac{kT}{\mu m_H (\gamma - 1)} \tag{3.7}$$

$$P = \frac{\rho k T}{\mu m_H} \tag{3.8}$$

We calculate the mean molecular weight neglecting heavy elements:

$$\gamma = 1 + \frac{y_{HI} + y_{HII} + y_{H2} + y_e}{\frac{3}{2} y_{HI} + \frac{3}{2} y_{HII} + \frac{5}{2} y_{H2} + \frac{3}{2} y_e} \tag{3.9}$$

The total energy and enthalpy of the gas per unit volume E, H can be given as:

$$E = \frac{1}{2}\rho v^2 \tag{3.10}$$

$$H = E + p \tag{3.11}$$

The computational domain is defined on a region with $R = [0, 4] \times 10^{10}$ cm and $z = [-4, 4] \times 10^{10}$ cm. The domain is configured with the numbers of cells $(N_R, N_z) = (480, 960)$.

To solve the equations, the boundary conditions and the initial conditions are required. We use the isothermal hydrostatic atmosphere as the initial condition. In the isothermal hydrostatic atmosphere, from the balance between the pressure gradient and the planetary gravity, we get the density profile as:

$$\rho(r) = \rho_{\rm p} \exp\left[\frac{GM_{\rm p}}{c_s^2}\left(\frac{1}{r} - \frac{1}{R_{\rm p}}\right)\right], \tag{3.12}$$

where r, $\rho_{\rm p}$ and $c_{\rm s}$ are the radius measured from the center of the planet, the density at the surface of the planet ($r = R_{\rm p}$), and the sound speed at the surface, respectively. The innermost atmosphere should not affect the dynamical structure of the upper escaping outflow. We fix the temperature and the density in the inner boundary at every time step to avoid non-physical inflow/outflow. The pressure gradient is larger in the inner region. We set the inner boundary region to save the computational cost. We check that the structure of the atmospheric escape is almost independent of the location of the inner boundary and the resolution.

We also set the outer boundary conditions to avoid the unphysical accumulation of escaping gas. The density contrast is set to unity at the outer boundary. At the symmetry axis, we use conventional reflective axisymmetric boundary conditions.

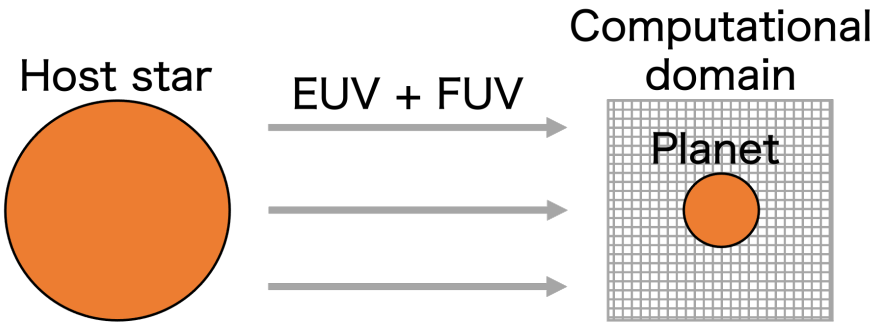

Fig 3.1: Schematic figure of our simulations. The host star is placed outside the computational domain and the planet is placed at the center of the domain.

Table 3.1: Model parameters in the fiducial run

Stellar parameters	
Stellar Mass M_*	$3\mathrm{M}_\odot$
Stellar Radius R_*	$1.6\mathrm{R}_\odot$
Stellar EUV photon emission rate	4.4×10^{38} photons/s
Stellar FUV luminosity	1.5×10^{34} erg/s
Planetary parameters	
Planet Mass M_p	0.3 $\mathrm{M_J}$
Planet Radius R_p	$1\mathrm{R_J}$
Semi-major axis a	0.045 AU
Metallicity Z	$0.1Z_\odot$
Dust-to-gas mass ratio	0.001

Table 3.2: Reactions and rate coefficients in our simulations. $T_{\rm eV}$ is the gas temperature in eV and T is the gas temperature in K.

Reaction	Reaction Rate Coefficient
$\mathrm{H} + \mathrm{e} \longrightarrow \mathrm{H}^+ + 2\,\mathrm{e}$	$\exp(-32.71396786+13.536556\ln T_{\rm eV}-5.73932875(\ln T_{\rm eV})^2+1.56315498(\ln T_{\rm eV})^3 - 0.2877056(\ln T_{\rm eV})^4 + 3.48255977 \times 10^{-2}(\ln T_{\rm eV})^5 - 2.63197617 \times 10^{-3}(\ln T_{\rm eV})^6 + 1.11954395 \times 10^{-6}(\ln T_{\rm eV})^7 - 2.03914985 \times 10^{-6}(\ln T_{\rm eV})^8)$
$\mathrm{H}^+ + \mathrm{e} \longrightarrow \mathrm{H} + \gamma$	$\exp(-28.6130338 - 0.72411256\ln T_{\rm eV} - 2.02604473 \times 10^{-2}(\ln T_{\rm eV})^2 - 2.38086188 \times 10^{-3}(\ln T_{\rm eV})^3 - 3.21260521 \times 10^{-4}\ln T_{\rm eV})^4 - 1.42150291 \times 10^{-5}(\ln T_{\rm eV})^5 + 4.98910892 \times 10^{-6}(\ln T_{\rm eV})^6 + 5.75561414 times 10^{-7}(\ln T_{\rm eV})^7 - 1.85676704 \times 10^{-8}(\ln T_{\rm eV})^8 - 3.07113524 \times 10^{-9}(\ln T_{\rm eV})^9$
$\mathrm{H} + \mathrm{H}^+ \longrightarrow \mathrm{H_2}^+ + \gamma$	$10^{-19.38-1.523\log_{10}T+1.118(\log_{10}T)^2-0.1269(\log_{10}T)^3}$
$\mathrm{H_2}^+ + \mathrm{H} \longrightarrow \mathrm{H_2} + \mathrm{H}^+$	6.4×10^{-10}
$\mathrm{H_2} + \mathrm{H}^+ \longrightarrow \mathrm{H_2}^+ + \mathrm{H}$	$3.0 \times 10^{-10}\exp(-2.1050 \times 10^4/T)$
$\mathrm{H_2} + \mathrm{e} \longrightarrow 2\,\mathrm{H} + \mathrm{e}$	$4.4 \times 10^{-10}T^{0.35}\exp(-1.02 \times 10^5/T)$
$\mathrm{H_2} + \mathrm{H} \longrightarrow 3\,\mathrm{H}$	$k_H^{1-a}k_L^a, k_L = 1.12 \times 10^{-10}\exp(-7.035 \times 10^4/T), k_H = 6.5 \times 10^{-7}T^{-1/2}\exp(-5.2 \times 10^4/T)(1-\exp(-6000/T)), a = 4.0 - 0.416\log_{10}(T/10^4) - 0.327(\log_{10}(T/10^4))^2$
$\mathrm{H_2}^+ + \mathrm{e} \longrightarrow 2\,\mathrm{H}$	$2.0 \times 10^{-7}T^{-1/2}$
$3\,\mathrm{H} \longrightarrow \mathrm{H_2} + \mathrm{H}$	$5.5 \times 10^{-29}T^{-1}$
$2\,\mathrm{H} + \mathrm{H_2} \longrightarrow 2\,\mathrm{H_2}$	$5.5 \times 10^{-29}T^{-1}/8$
$2\,\mathrm{H_2} \longrightarrow 2\,\mathrm{H} + \mathrm{H_2}$	$k_H^{1-a}k_L^a, k_L = 1.18 \times 10^{-10}\exp(-6.95 \times 10^4/T), k_H = 8.125\times10^{-8}T^{-1/2}\exp(-5.2\times10^4/T)(1-\exp(-6000/T)), a = 4.845 - 1.3\log_{10}(T/10^4) + 1.62(\log_{10}(T/10^4))^2$
$2\,\mathrm{H} \longrightarrow \mathrm{H}^+ + \mathrm{e} + \mathrm{H}$	$1.7 \times 10^{-4}k_1$
$\mathrm{H}^- + \mathrm{H} \longrightarrow \mathrm{H_2} + \mathrm{e}$	$4.0\times10^{-9}T^{-0.17}$ for $(T > 300\,\mathrm{K})$, 1.5×10^{-9} for $(T < 300\,\mathrm{K})$

3.2 Heating and cooling processes

The heating rate Γ and the cooling rate Λ determine the thermal structure of the upper atmosphere. We describe the heating/cooling rate implemented in our simulation code in this section. We also explain the atmospheric structure of our simulations with FUV heating in the heating section.

3.2.1 Cooling processes

The cooling processes also determine the thermo-chemical structure and the escaping outflow. We consider several radiative cooling processes in the model. The most important radiative cooling process is the radiative recombination cooling. The electron energy is lost by the recombination of the hydrogen ions and the cooling rate can be written by

$$\Lambda_{rec} = \frac{2}{3} kT\, R_{rec}\, n_e\, n_{H^+} \tag{3.13}$$

where R_{rec} is the rate coefficient of the recombination (Spitzer 1978). The Lyman-α cooling due to the collisional excitation can be given as:

$$\Lambda_{Ly\alpha} = \left(\frac{7.5 \times 10^{-19} e^{-118348\mathrm{K}/T}}{1 + \sqrt{T/100000\mathrm{K}}} \,\mathrm{erg\,cm^{-3}\,s^{-1}} \right) n_e n_H \tag{3.14}$$

Previous models have found that the Lyman-α cooling dominates the recombination cooling (Murray-Clay et al. 2009) and we also check that Lyman-α cooling is the dominant cooling process in our simulations. We also compute the OI line cooling which can contribute to the total cooling rate in the atmosphere. The cooling rate can be given as:

$$\Lambda_{\mathrm{OI}} = \Sigma_j x_j \Sigma A_{ji} \Delta E_{ji} \tag{3.15}$$

where x_j is the population of level j, and $A_{ji}, \Delta E_{ji}$ are the Einstein coefficient and the transition energy of $j \rightarrow i$ transition. We calculate the level population by the statistical equilibrium:

$$x_i \Sigma_{j \neq i} c_{ij} = \Sigma_{i \neq j} x_j c_{ji} \tag{3.16}$$

We can calculate c_{ji} from the collisional excitation/de-excitation rate (Osterbrock and Ferland 2006; Santoro and Shull 2006). We find that the metal line cooling is not significant in the total cooling rate unless the metallicity of the atmosphere is significantly large.

In the planetary outflow, not only the radiative cooling processes but also the adiabatic cooling is significant. The cooling rate can be given as:

$$\Lambda_{\rm adi} = -P\frac{d}{dt}\frac{1}{\rho}, \tag{3.17}$$

The expansion of the gas causes the adiabatic cooling. This cooling is also called PdV cooling in the context of the atmospheric escape. The cooling rate dominates in the upper region of the outflow and the process cools the gas.

3.2.2 EUV heating

The EUV heating can drive the escape and it is a unique radiative heating process in many previous studies. The radiative transfer for EUV photoionization of hydrogen can be written as:

$$F_\nu(a) = \frac{\Phi_\nu}{4\pi a^2}\exp(-\sigma_\nu N_{\rm HI}) \tag{3.18}$$

where a is the distance to the host star, ν is a frequency of photons, F_ν is the EUV flux, and σ_ν is the absorption cross section. The column density of the neutral hydrogen is given as:

$$N_{\rm HI} = \int dr n_{\rm HI} \tag{3.19}$$

where $n_{\rm HI}$ is the number density of the neutral hydrogen. The absorption cross section can be written as Osterbrock and Ferland 2006:

$$\sigma_\nu = 6.3\times10^{-18}\left(\frac{h\nu}{h\nu_1}\right)^{-3}\ {\rm cm}^2 \tag{3.20}$$

where $h\nu_1 = 13.6\,{\rm eV}$ and the photoionization rate and heating rate are given as:

$$R_{\rm ion} = \frac{n_{\rm HI}}{n_{\rm H}}\int_{\nu_1}^{\infty} d\nu\sigma_\nu F_\nu \tag{3.21}$$

$$\Gamma_{\rm EUV} = \frac{1}{\rho}n_{\rm H}\int_{\nu_1}^{\infty} d\nu\sigma_\nu h(\nu-\nu_1)F_\nu \tag{3.22}$$

The flux depends on the spectral shape. We assume the blackbody spectra and the temperature is 10^4 K. We find that the results are almost independent of the temperature of the blackbody. In our code, we use the luminosity of the EUV photons $\Phi_{EUV}({\rm s}^{-1})$ as a parameter. In previous studies, X-ray radiation also contributes to the heating rate in the same process. Such heating due to the high-energy radiation is significant in young systems with high X-ray luminosity. In this study, we focus on the observed typical hot Jupiters and we neglect the heating due to the X-ray. We have checked the atmospheric structure with the EUV heating and found that the structure was consistent with previous studies.

3.2.3 FUV heating

Far-ultraviolet photons can also heat the atmosphere and contribute to the escape. FUV photons cannot photoionize hydrogen atoms. There are several FUV heating processes that may contribute to the heating in the atmosphere. We introduce three heating processes that might be a dominant heating source in the upper atmosphere and the results of the simulations with each heating process. In this section, we show the results of our simulations with FUV heating and discuss the physical conditions which determines the FUV heating effect on the atmospheric escape.

The first FUV heating process is the photoelectric heating of the dust grains. This process affects the structure of ISM and widely known in the context of the ISM. In this process, the dust grains provide photoelectrons and the photoelectrons thermalize into gas. The existence of dust grains is necessary for this process. The size distribution and the amount of dust grains in the upper atmosphere are not known. We assume the ISM-like dust properties as a fiducial case and investigate the dust amount dependence. We implement the photoelectric heating rate of Bakes and Tielens 1994:

$$\Gamma_{\rm pe} = 10^{-24}\,\epsilon_{pe} G_{\rm FUV} n_{\rm H} Z/Z_\odot \text{ ergs s}^{-1}\text{ cm}^{-3} \tag{3.23}$$

$$\epsilon_{pe} = \frac{4.87\times10^{-2}}{1+4\times10^{-3}(G_{\rm FUV}\sqrt{T}/n_e)^{0.73}} + \frac{3.65\times10^{-2}(T/10^4\text{ K})^{0.7}}{1+2\times10^{-4}G_{\rm FUV}\sqrt{T}/n_e} \tag{3.24}$$

where ϵ_{pe} is the heating efficiency that depends on the gas temperature T, electron density n_e and local normalized FUV flux $G_{\rm FUV}$, and $n_{\rm H}$ is the hydrogen nuclei number density. In our code with FUV photoelectric heating, we use the FUV flux defined by $G_{\rm FUV} = F_{FUV}\exp(-1.8A_{\rm V})/(1.6\times10^{-3}\,\text{erg s}^{-1}\,\text{cm}^{-2})$, where F_{FUV} is the FUV flux in $\text{erg s}^{-1}\,\text{cm}^{-2}$, and $A_{\rm V} = 5.34\times10^{-22}N_H(Z/Z_\odot)\,\text{mag cm}^2$ is the visual extinction. The efficiency of the photoelectric heating depends on the size distribution of the dust grains and the UV spectral shape.

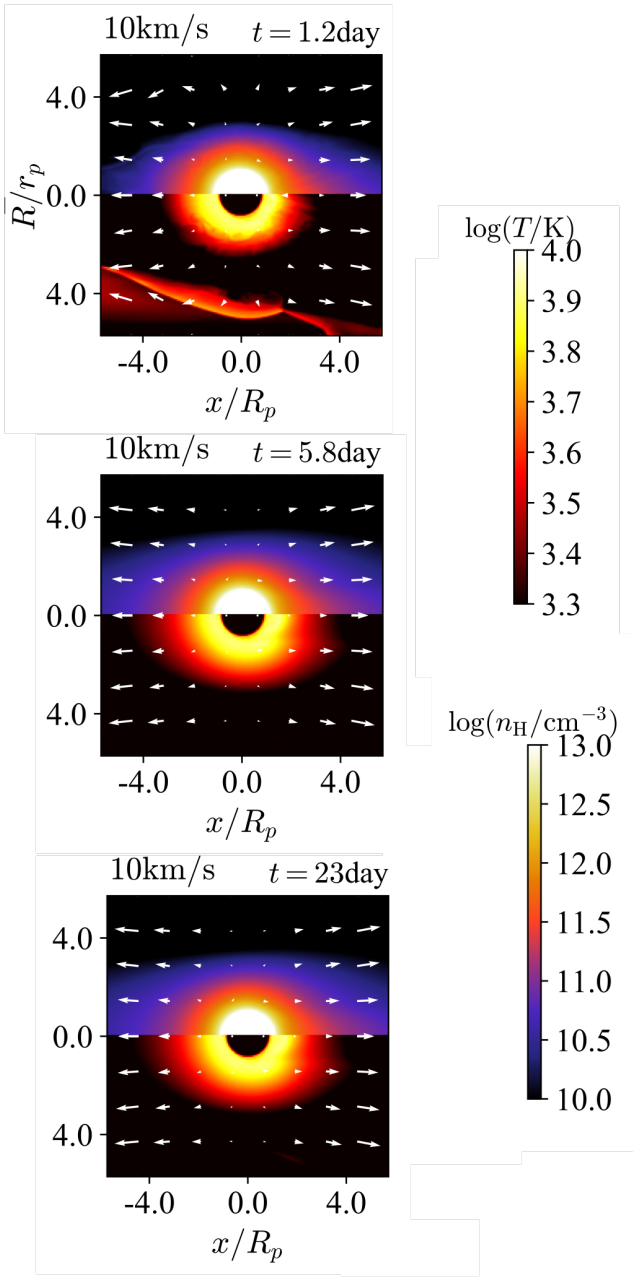

Fig 3.2: The snapshots of the fiducial planet with FUV photoelectric heating at $t = 1.2$ days (top), $t = 5.8$ days (middle), and $t = 23$ days (bottom). The FUV flux is injected from the left side of the panel. In each panel, the upper half shows the density profile and the lower half shows the temperature profile, and the arrows show the gas velocity field.

Figure 3.2 shows the snapshots of the simulations with FUV photoelectric heating. The system reaches a quasi-steady state within a few days after the initial condition. The dynamical timescale is much shorter than our computational time. We find that the FUV photoelectric heating can drive the atmospheric escape. Figure 3.3 shows the time-averaged radial profiles of the fiducial case. We can see that the FUV heating rate dominates the heating and the cooling due to the gas expansion dominates the cooling.

In this process, the existence of the dust grains like PAHs in the upper atmosphere is required. In our simulations, the gas temperature reaches $\sim 10^4\,\mathrm{K}$, above the sublimation temperature of graphite of $\sim 2200\,\mathrm{K}$ at $n_\mathrm{H} \sim 10^{13}\ \mathrm{cm}^{-3}$ (Baskin and Laor 2018). Thus the sublimation of the dust grains can reduce the photoelectric heating and suppress the mass-loss outflow driven by the FUV radiation. In the planetary outflows where the temperatures are $\sim 10^4\mathrm{K}$, the collision with the helium atoms can sputter the carbon of the PAHs (Micelotta et al. 2010). The lifetime of PAHs can be estimated from the results of Micelotta et al. 2010:

$$\tau_\mathrm{PAHs} = \frac{N_C}{R_T} \sim 10^{6-10}\mathrm{s} \tag{3.25}$$

where R_T is the rate coefficient for collisional destruction. We should also consider the dust formation rate. Theoretical chemical calculations (Morley et al. 2012; Lavvas and Koskinen 2017) show that the dust formation rate in the upper atmosphere is low. Thus, the dominant dust supply process is transport from the inner region. The small dust grains which can contribute to the FUV photoelectric heating rate in our simulations can be dragged by the upward outflow. The drag force exerted on a moving grain in a gas with temperature T and number density n is given by

$$F_\mathrm{drag} \approx 2\pi a_g^2 kTn \times \frac{8s}{3\sqrt{\pi}}\left(1+\frac{9\pi}{64}s^2\right), \tag{3.26}$$

where a_g is the grain radius and $s = \sqrt{\mu v^2/2kT}$ with μ is the mean molecular mass (Baines et al. 1965; Draine 2011). Equating the drag force to the gravitational force, we derive

$$\begin{aligned}\frac{GM_pM_d}{r^2} \times \frac{3\sqrt{\pi}}{16\pi a_g^2 kTn} &= s\left(1+\frac{9\pi}{64}s^2\right) \\ &> s = \sqrt{\mu v^2/2kT}\end{aligned} \tag{3.27}$$

Hence, if the atmosphere is escaping at a speed greater than

$$\begin{aligned}v_\mathrm{c} = 10.1\,\mathrm{m\,s^{-1}} &\times \left(\frac{M_p}{M_J}\right)\left(\frac{r}{R_J}\right)^{-2}\left(\frac{a_g}{10\text{Å}}\right) \\ &\times \left(\frac{\rho_d}{3\,\mathrm{g\,cm^{-3}}}\right)\left(\frac{n}{10^{12}\,\mathrm{cm}^3}\right)^{-1}\left(\frac{T}{10^3\mathrm{K}}\right)^{-1/2}\left(\frac{\mu}{m_p}\right)^{-1/2},\end{aligned} \tag{3.28}$$

the dust grains can be transported to upper layers by the drag force. This lifetime should be compared with the hydrodynamical timescale, the sound crossing time of $\tau = R_p/c_s \sim 10^4$ s. Clearly, the destruction of PAHs is unimportant in the escaping atmosphere of the hot Jupiters we study here.

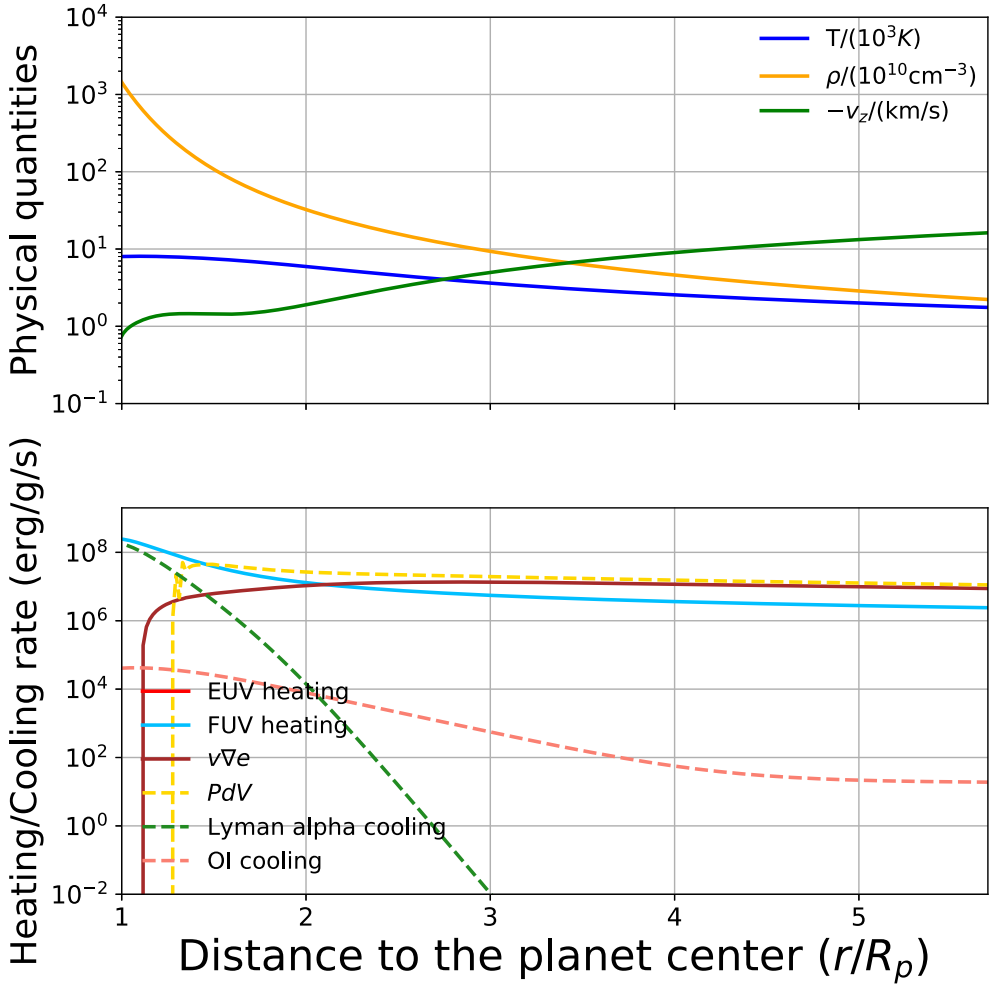

Fig 3.3: The radial profile of the fiducial atmosphere with dust photoelectric heating. In the upper panel, the radial profiles of physical quantities are shown. In the bottom panel, the heating and cooling rates in our simulation are shown. The solid curves show the heating rates and the dashed curves show the cooling rate profiles.

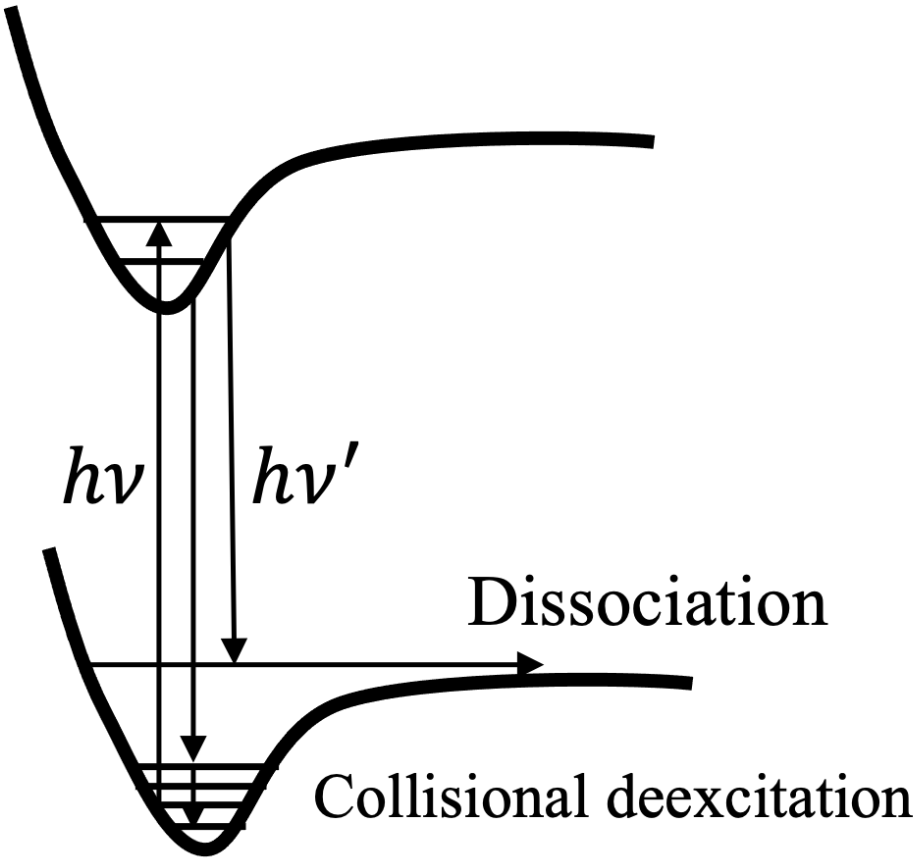

Fig 3.4: The schematic figure of pumping process. Lyman-Werner photons excite molecular hydrogens. Excited hydrogens are either photodissociated or de-excited by collision.

The second one is the heating through H_2 pumping process. The Lyman-Werner photons (11.2 eV-13.6 eV) excite the molecular hydrogens. The excited H_2 are dissociated or de-excitated through collision (Figure 3.4). The photodissociation and collisional de-excitation heat the atmosphere.

About 10 % of the excited hydrogen molecules dissociate. We also calculate the photodissociation of H_2. The heating rate of H_2 photodissociation is given by:

$$\Gamma_{\rm diss} = \Delta E_{\rm diss} R_{\rm diss} n_{\rm H_2}, \tag{3.29}$$

where $R_{\rm diss}$ represents the photodissociation coefficients (Draine and Bertoldi 1996).

$$R_{\rm diss} \sim 4 \times 10^{-11} G_{\rm FUV} \beta n_{\rm H_2}\, {\rm s}^{-1} \tag{3.30}$$

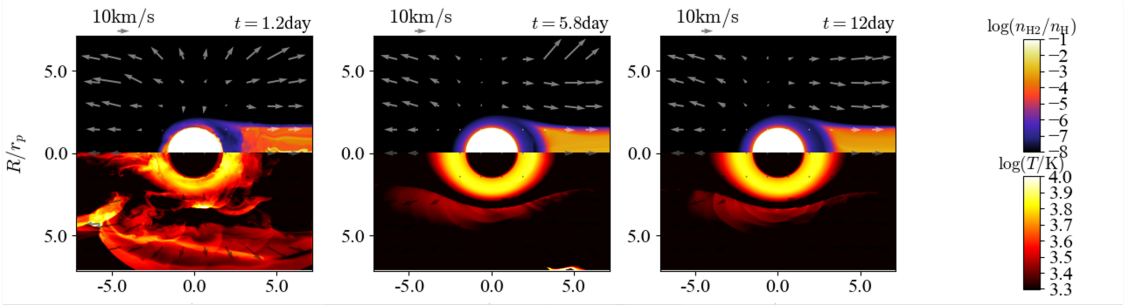

Fig 3.5: Snapshots of the fiducial planetary atmosphere at $t = 1.2$days (left), $t = 5.8$days (middle), and $t = 12$days (right). Radiation from the central star are injected from left side of the figure. In each panel, the upper half shows the H_2 abundance and the lower half shows the temperature profile, and the arrows show the velocity of the gas.

where $G_{\rm FUV}$ is the local FUV flux normalized by $1.6 \times 10^{-3}\,{\rm erg/cm/s}$ and β is the self-shielding factor given by:

$$\beta = \begin{cases} 1 & (N_{\rm H_2} < N_0) \\ \left(\frac{N_{\rm H_2}}{N_0}\right)^{-0.75} & (N_{\rm H_2} > N_0) \end{cases} \tag{3.31}$$

where $N_{\rm H_2}$ represents the column density of the molecular hydrogen and $N_0 = 10^{14}\,{\rm cm^{-2}}$.

The heating rate of the collisional de-excitation is also given by:

$$\Gamma_{\rm pump} = \Delta E_* (9 R_{\rm diss}) \left(1 + \frac{n_{\rm cr}}{n_{\rm H}}\right)^{-1} n_{\rm H_2}, \tag{3.32}$$

where $n_{\rm cr}$ is the critical density. In general, the heating rate of the de-excitation is 1-2 orders of magnitude larger than that of the photodissociation and the heating through the photodissociation has only a small contribution to the total heating rate. Figure 3.5 shows the planetary atmosphere with FUV heating through H_2 pumping process. The heating through H_2 pumping can drive the atmospheric escape as well as the FUV photoelectric heating of dust grains.

The last FUV heating process is Balmer absorption (García Muñoz and Schneider 2019). The photoionization of the excited hydrogen atoms at the $n = 2$ level causes the heating. This process has been investigated in the simulation of KELT-9b which is a known hot Jupiter around the hottest star. In the Balmer absorption process, the excited hydrogen atoms absorb low-energy ultraviolet photons and the photoelectrons thermalize into gas. The photoionization rate coefficient of $n = 2 \to \infty$ is 7 orders of magnitude larger than that

of $n = 1 \rightarrow \infty$ in the planetary atmosphere around hot stars due to the strong radiation (García Muñoz and Schneider 2019). Theoretical simulations show that the heating due to the Balmer absorption is significant for planets around hot stars. The heating rate can be given as:

$$\Gamma_{\rm Balmer} = \frac{1}{\rho} n_2 \int_{\nu_1}^{\infty} {\rm d}\nu \, \sigma_\nu h(\nu - \nu_1) F_\nu \tag{3.33}$$

where σ_ν is the photoionization cross section and $h\nu_1 = 3.4\,{\rm eV}$. We use the stellar spectra of Husser et al. 2013 for F_ν. We can assume the optical depth $\tau_{\rm balmer} = 0$. We can calculate the cross section neglecting the bound-free Gaunt factor and using the analytical formula (Mihalas 1978):

$$\sigma_\nu = \left(\frac{64\pi^4 m_e e^{10}}{3\sqrt{3} c h^6} \right) \frac{1}{n'^5 \nu^3} \tag{3.34}$$

where $n' = 2$. We find that the integration part of Equation 3.33 is $\sim 4.8 \times 10^{-8}\,{\rm erg/s}$, $2.3 \times 10^{-10}\,{\rm erg/s}$ for the planet ($a = 0.045\,{\rm au}$) around the host stars ($T_{\rm eff} = 10200\,{\rm K}$, $\log g = 4.0\,{\rm cm/s^2}, T_{\rm eff} = 6500\,{\rm K}$, $\log g = 4.5\,{\rm cm/s^2}$). To calculate the heating rate, we also need to know the level population of the hydrogen atoms because our simulations do not follow the level population of hydrogen atoms and the heating rate is proportional to the $n = 2$ level population.

The photoelectric heating by dust grains depends on the amount of dust. The last two heating processes are independent of the existence of dust. The heating rate through H_2 pumping process depends on the amount of molecular hydrogen and the formation process is important to maintain the amount of molecular hydrogen. We implement chemical reactions including the formation reactions for molecular hydrogen (Table 3.2).

Figure 3.6 shows the radial profiles of the chemical reaction rates. We find that the photodissociation rate is balanced by the formation rate of molecular hydrogen (H^- reaction and three-body reaction). In the absence of dust in the upper atmosphere, molecular hydrogen is formed through chemical reactions and the H_2 pumping process could be significant. The pumping heating is significant even in the metal-poor planetary atmosphere around the host star.

Figure 3.7 shows the heating rate profile of hot Jupiters around hot A-stars ($T_{eff} = 10000\,{\rm K}$). In the case of the ultra-hot Jupiters around the hot star, such as KELT-9 b, the heating due to the Balmer absorption dominates below $10^{-9}\,{\rm bar}$ and the heating due to the pumping has a minor effect although it is also larger than the heating due to the photoionization of ground state hydrogen atoms in the lower region. The high temperature

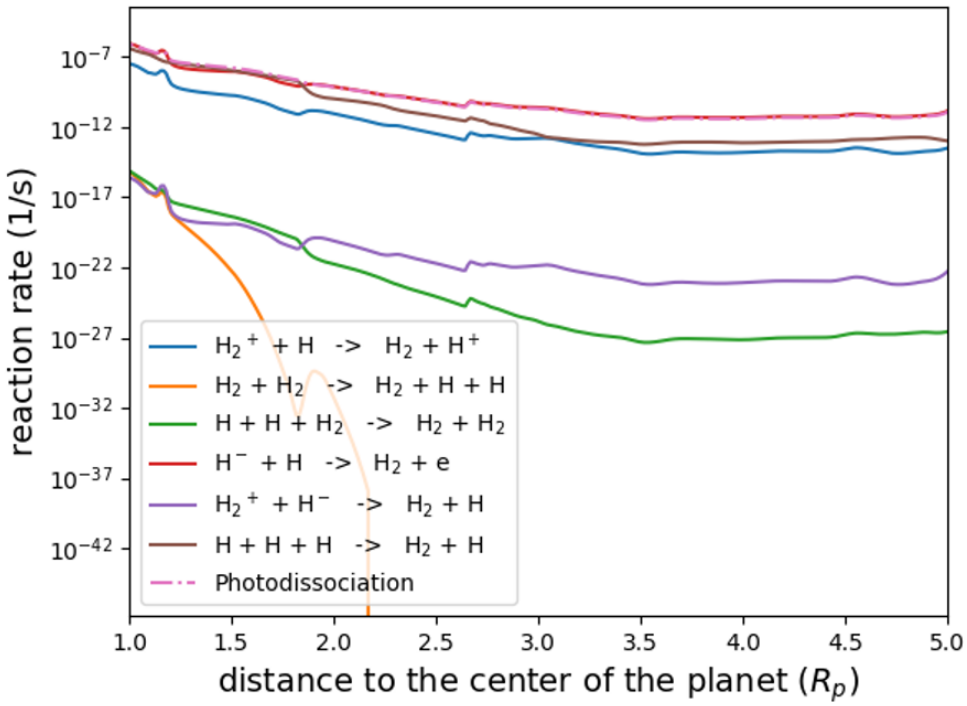

Fig 3.6: Radial profiles of chemical reaction rates of hydrogen. Solid curves and dashed curves represent the formation rate and destruction of hydrogen molecule.

of the atmosphere can increase the population of hydrogen atoms at the $n = 2$ level and reduce the abundance of the molecular hydrogens by dissociation. Planets like KELT-9 b may experience a more extreme mass loss due to the Balmer absorption process than the mass loss due to the EUV photoionization of hydrogen atoms at the ground state.

However, in the case of the planets around relatively cool A-stars like HAT-P-57 b (Hartman et al. 2015, $T_{eff} = 7500\,\mathrm{K}$), the pumping heating becomes comparable to the Balmer absorption in $P > 0.1\,\mu$bar because of the relatively low temperature of the gas of the atmosphere leading to a low population of the excited $n = 2$ hydrogen atoms. Figure 3.8 shows the similar profile of HAT-P-57 b case. This may indicate that the pumping heating is significant in planets around hot stars with semi-major axis $a > 0.1\,\mathrm{AU}$ because the FUV flux also depends on the distance to the host star.

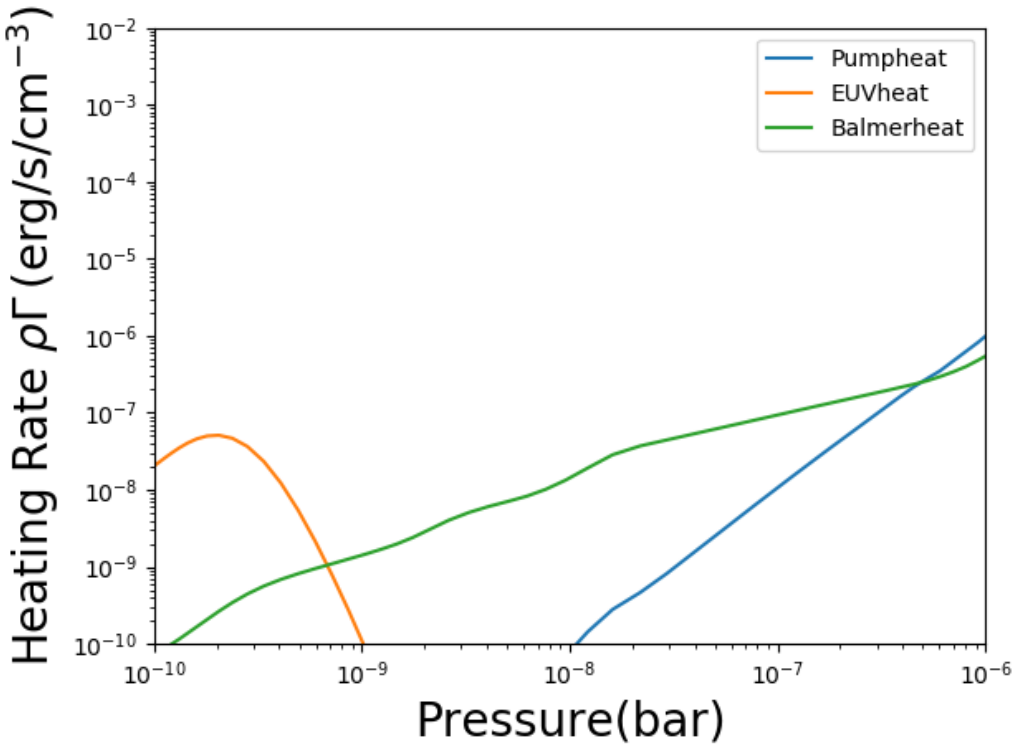

Fig 3.7: Radial profiles of heating rate in hot Jupiters around hot A-stars ($T_{\rm eff} = 10000\,\mathrm{K}$).

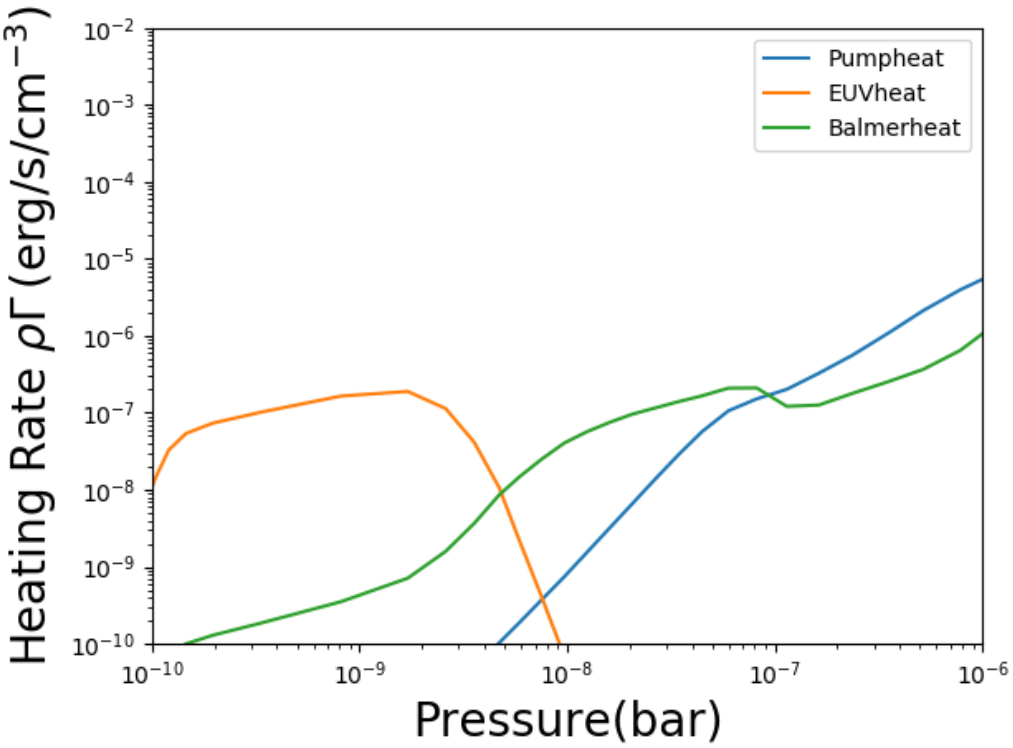

Fig 3.8: Radial profiles of heating rate in HAT-P-57 b. The planetary mass is $M_p = 1.85\,M_{\rm J}$ and the radius is $R_p = 1.4\,R_{\rm J}$. We set the effective temperature of the host star is 7600 K.

3.3 The impact of the FUV driven escaping outflow on the observed planetary distributions

We find that the mass-loss rate is dominated by FUV heating in close-in planets around hot stars because the FUV luminosity is significantly large. We investigate the stellar temperature dependence of the mass-loss rates due to FUV photoelectric heating (Figure 3.9). We find that the FUV photoelectric heating can drive the mass loss around hot stars, while classical EUV photoionization heating drives the outflow around cooler stars ($T_{eff} < 6500$ K). The strong FUV radiation can drive the strong atmospheric escape and the mass-loss rate becomes higher. Our simulation is consistent with the previous studies of hot Jupiters around solar-type stars.

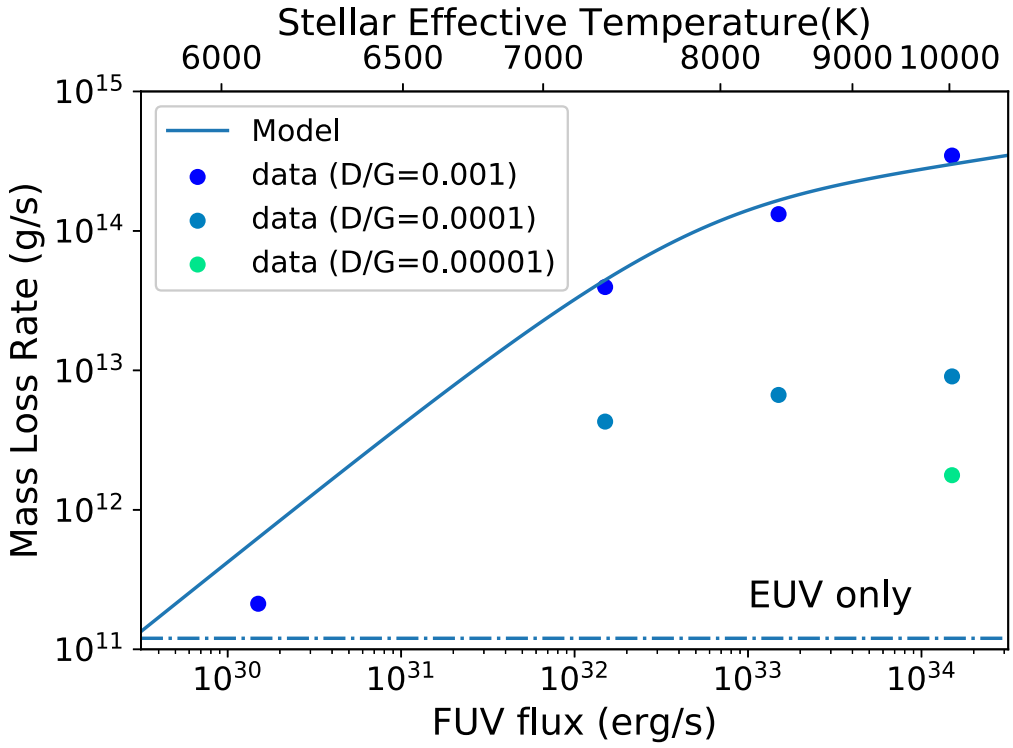

Fig 3.9: The stellar temperature dependence of the mass-loss rates by FUV photoelectric heating. The dots show the results of our simulations. The solid curve shows the mass-loss rate estimated by the FUV photoelectric heating efficiency.

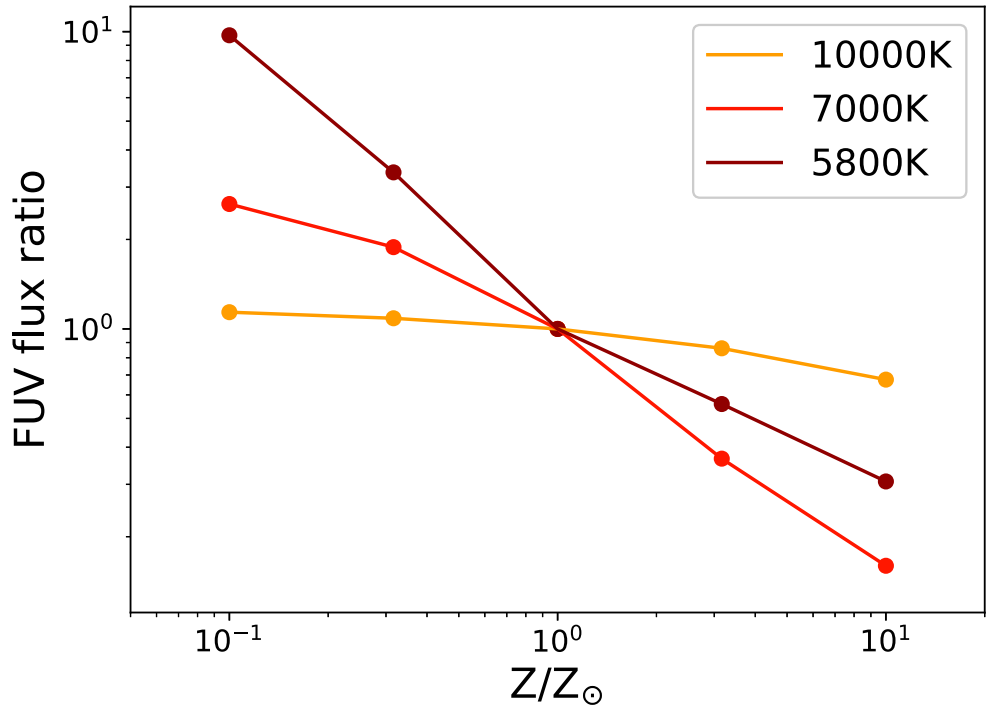

Fig 3.10: The metallicity dependence of the FUV luminosity. The dots show the FUV flux ratio to the solar metallicity and same temperature stars. FUV luminosity is obtained from the theoretical spectra (Husser et al. 2013).

This stellar temperature dependence is consistent with the dependence of the observed sub-Jupiter desert. We also investigate the dependence of the dust abundance on the mass-loss rates because the dust abundance in the upper atmosphere of hot Jupiters is not clear. The small amount of dust grains results in a low photoelectric heating rate and the low mass-loss rate. We find that the FUV photoelectric heating can drive the mass loss when the dust-to-gas mass ratio is large enough $D/G > 10^{-5}$. If we assume that the amount of dust in the atmosphere is proportional to the stellar metallicity, the mass-loss rates become smaller in metal-poor systems. We also find that the mass loss due to the photoelectric

heating can be given as:

$$\dot{M} = \epsilon_{pe} \frac{\pi R_p^3 F_{\rm UV}(1{\rm AU})}{GM_p} \left(\frac{a_p}{1{\rm AU}}\right)^{-2} \tag{3.35}$$

$$= 1.5 \times 10^{12}\, \epsilon \left(\frac{F_{\rm FUV}}{10^{30}{\rm erg/s}}\right) \times \left(\frac{R_p}{R_j}\right)^3 \left(\frac{M_p}{M_j}\right)^{-1} \left(\frac{a_p}{0.045{\rm AU}}\right)^{-2} {\rm g/s} \tag{3.36}$$

The heating efficiency determines the mass-loss rate similar to the typical energy-limited mass-loss rates due to EUV photoionization heating.

We also note that the FUV luminosity depends on the stellar metallicity. The opacity of the stellar atmosphere depends on the free electrons from metals. The metal-rich stars tend to have low FUV luminosities. Figure 3.10 shows the metallicity dependence of the FUV luminosity. We compute the FUV luminosity from the theoretical spectra of Husser et al. 2013 by integrating the flux in FUV wavelength. We note that the metallicity dependence is important around cool stars, such as solar-type stars, and that the FUV luminosity is almost independent of the stellar metallicity in hot stars. As we discussed in the previous section, the FUV heating is significant in hot stars. The metallicity dependence of the FUV flux may be important around intermediate stars ($T_{eff} \sim 7000$ K). In the case of the observed planets, many of the host stars are late type stars. Our FUV heating due to the H_2 pumping and the Balmer absorption is consistent with the stellar temperature dependence of the sub-Jupiter desert.

3.4 Summary

In this chapter, we investigate the effect of the FUV on the atmospheric escape. In many of the previous theoretical simulations neglect the FUV effect and focus on the EUV heating as the heating source. Ultra-hot Jupiters like KELT-9b have very hot host stars and such stars emit strong FUV from their photospheres. We focus on such close-in gas giant planets around hot stars which might experience the different evolution. There are three possible heating processes by FUV; (i) photoelectric heating by dust grains, (ii) H_2 pumping heating, and (iii) Balmer absorption. We study all of the three processes. We find that the (i) dust photoelectric heating dominates the heating rate and drives the atmospheric escape when the upper atmosphere has a sufficient amount of dust grains. In a cooler host star case, the FUV photoelectric heating rate becomes small and the classical EUV heating dominates

due to the low FUV luminosity relative to the EUV. We also find that the (ii) H_2 pumping process and the Balmer absorption process dominate the heating rate even if there is no dust grain in the upper atmosphere. In the case of very hot host star $T_{eff} \sim 10000$ K, the (iii) Balmer absorption exceeds the heating rate of the H_2 pumping process because the high temperature results in the small amount of the molecular hydrogen. In the case of intermediate temperature stars $T_{eff} \sim 7000$ K, the H_2 pumping also becomes significant. We conclude that the FUV heating is important for the atmospheric escape of hot Jupiters around hot stars and enhances the mass-loss of planets. The lifetime of the planet can be less than a Gyr and this may be consistent with the small number of hot Jupiters around hot stars.

Chapter 4

Wind confinement of the escaping atmosphere

The stellar UV radiation heating launches the planetary outflow and the flow can be observed in the transit absorptions. We have not calculated the observational signal from the upper atmosphere in the previous chapter. The upper atmosphere contributes Lyman-α absorption and thus the structure of the outflow above the sonic point, which cannot affect the mass-loss rate, is also important for understanding the observational signal. Not only the EUV flux but also the wind effect can change the structure and the observational signals. In this chapter, we discuss the stellar wind confinement effect which determines the structure of the planetary outflow and the observational absorption signals. The wind confinement may be an origin of non-detection of Lyman-α absorption in close-in planets which has been found by recent observations. We perform the first radiation hydrodynamics simulations of the escaping outflow with the stellar wind from the launching point to the point where the stellar wind interaction occurs in a self-consistent manner. We discuss the possible transit signature other than the classical Lyman-α absorption and investigate the possibility of understanding the stellar wind effect from the observations. We finally explain the impact of the stellar activity on the outflow and observational signatures. In this chapter, "wind" refers to the stellar wind from the host star, and "outflow" refers to the escaping outflow from the planet.

4.1 Methods: Radiation hydrodynamics simulations of the atmospheric escape with the stellar winds from the host star

The escaping outflow interacts with the stellar wind. This interaction can modify the escaping outflow and affect the observed transit absorption during the transit. Hydrodynamics simulations show that the wind can confine the planetary outflow and reduce the transit depth (e.g. Matsakos et al. 2015; Christie et al. 2016; Shaikhislamov et al. 2016; Khodachenko et al. 2017; Villarreal D'Angelo et al. 2018; McCann et al. 2019; Odert et al. 2020; Vidotto and Cleary 2020; Carolan et al. 2020, 2021b; Villarreal D'Angelo et al. 2021). For young planetary systems, where the host star is active and generates a powerful stellar wind, the wind effects on the transit signals can be significant. The stellar wind can also suppress the atmospheric escape in close-in planets (Adams 2011; Lecavelier des Etangs et al. 2012a; García Muñoz et al. 2020).

To understand the observed transit signature, the multi-dimensional hydrodynamics simulations of the geometry of the outflow are required. Most of the previous studies have performed simulations without self-consistent calculation of the upper atmosphere from the launching point, and have investigated only the Lyman-α transit signal. Recent ground-based observations of the atmospheric escape and the upper atmosphere have used other lines (e.g. Helium triplet line), but most of the theoretical simulations have focused on the classical Lyman-α transit. To investigate the wind effect on the new transit observations is one of the aims of this study.

We implement the quiescent stellar wind in our radiation hydrodynamics code in the previous chapter. Our code includes the EUV photoionization effect and solves the non-equilibrium chemistry as in Chapter 3. The gas density, temperature, and velocity are set to be a solar wind value for the boundary condition. The fiducial model parameters are listed in Table 4.1. In this chapter, we only consider heating by EUV photoionization of hydrogen atoms because the EUV heating rate dominates the heating source and drives the escape in typical hot Jupiters around solar-type stars as discussed in the previous chapter. The young active stars tend to have high EUV luminosities and the effect of FUV heating may be smaller than that of EUV photoionization heating. Our fiducial model sets the stellar wind strength in terms of the mass-loss rate, which is equal to the solar value $\dot{M}_\odot = 2 \times 10^{-14}\, M_\odot\, \mathrm{yr}^{-1}$. We set the wind velocity and the wind temperature to be the solar value. The wind density can be calculated from the mass-loss rate of the star, the semi-major axis, and the velocity of the wind. We also investigate the planets around

active stars with strong stellar wind. In the case of strong stellar wind, we assume that the speed of the wind is the same as in the fiducial case and change the wind density. We run simulations with $\dot{M}_* = 1\,\dot{M}_\odot, 10\,\dot{M}_\odot, 100\,\dot{M}_\odot$ case to investigate the shape of the outflow around active stars (e.g. young M dwarfs). Our fiducial EUV flux is similar to that of the solar-type star. Young active stars typically have high EUV emissivity. We will discuss the EUV flux effect on the absorption signals. In these simulations, we neglect the metal line cooling and consider hydrogen recombination cooling (Spitzer 1978) and Lyman-α cooling of HI (Anninos et al. 1997) as the major radiative cooling processes because the metal cooling is negligible for typical atmosphere of hot Jupiters as discussed in Chapter 3. Our models correspond to zero metal $Z = 0$ atmosphere in this sense.

Table 4.1: Model parameters in the fiducial run

Stellar parameters	
Stellar Mass M_*	$1\,M_\odot$
Stellar Radius R_*	$1\,R_\odot$
Stellar EUV photon emission rate Φ_{EUV}	$1.4 \times 10^{38}\,\mathrm{s}^{-1}$
Stellar wind strength	$2 \times 10^{-14}\,M_\odot\,\mathrm{yr}^{-1}$
Stellar wind velocity	$540\,\mathrm{km/s}$
Stellar wind temperature	$2 \times 10^6\,\mathrm{K}$
Stellar wind density	$2.5 \times 10^3\,\mathrm{g/cm}^3$
Planetary parameters	
Planet Mass M_p	$0.3\,M_\mathrm{J}$
Planet Radius R_p	$1\,R_\mathrm{J}$
Semi-major axis a	$0.045\,\mathrm{AU}$

4.2 Structure of the escaping atmosphere and the observational transit signals

Figure 4.1 shows the snapshots of our simulations with $\dot{M}_* = 1\,\dot{M}_\odot, 10\,\dot{M}_\odot, 100\,\dot{M}_\odot$. The EUV photoionization of hydrogen atoms heats the atmosphere and the temperature of the outflow reaches ~ 5000K. We can see that the planetary outflow interacts with the stellar wind in the upper atmosphere and the wind confines the outflow in the direction of the host star.

The pressure balance determines the confinement (Figure 4.2) and can be expressed

approximately as

$$k_{\rm B}\rho_{\rm p}(r)\,T_{\rm p}(r)/\mu m_H = \rho_*(r)\,v_*^2(r) \tag{4.1}$$

where $\rho_{\rm p}(r), T_{\rm p}(r)$ represent the density and temperature of the planetary atmosphere at the contact point r, μ is the mean molecular weight, m_H is the hydrogen atomic mass, and $\rho_*(r), v_*(r)$ are the density and velocity of the wind. To examine this, we run additional simulations with different wind velocities fixing $\dot{M}_*$. We have found that a higher wind velocity results in stronger confinement of the atmosphere. We can assume spherical symmetry because the properties of the outflow on the day-side are close to the properties of the spherical case, the mass-loss rate of the planet is

$$\dot{M}_{\rm p} = 4\pi r^2 \rho_{\rm p} v_{\rm p}, \tag{4.2}$$

and that of the host star is

$$\dot{M}_* = 4\pi a^2 \rho_* v_*. \tag{4.3}$$

Then the effective confinement radius is estimated to be

$$\begin{aligned} r_{eff} &= \sqrt{\frac{\dot{M}_{\rm p}}{\dot{M}_*}\frac{k_{\rm B}T_{\rm p}}{\mu m_H v_{\rm p} v_*}}\,a \\ &\approx 4\times10^{10}\,{\rm cm}\left(\frac{\dot{M}_{\rm p}}{3\times10^{10}\,{\rm g/s}}\right)^{1/2}\left(\frac{\dot{M}_*}{\dot{M}_\odot}\right)^{-1/2}\left(\frac{T_p}{5000\,{\rm K}}\right)^{-1/2} \\ &\times\left(\frac{v_p}{1\times10^5\,{\rm cm/s}}\right)^{-1/2}\left(\frac{v_*}{540\,{\rm km/s}}\right)^{-1/2}\left(\frac{a}{0.045\,{\rm au}}\right) \end{aligned} \tag{4.4}$$

We confirm that the approximated radius is close to the radius obtained by our results as seen in Figure 4.2.

In our simulations, the system reaches the quasi-steady state within a few days after the initial condition. The hydrodynamic timescale of the system is a few hours. In the fiducial run, the heating rate of EUV photoionization is about $10^6\,{\rm erg\,g\,s^{-1}}$ and the photoionization timescale is a few 10 hours. The photoionization timescale determines the time for the system to reach equilibrium. We assume the static EUV flux in our models. The EUV flux in actual planets can be variable for some reasons. If the host star has flare activities like the sun, the EUV flux may change with relatively short timescale (Nishimoto et al. 2020). The system cannot reach the quasi-steady state during such short time activities. The eccentricity of planets may reflect the history of orbital evolution. For orbits with non-zero eccentricity, the incident EUV flux varies with time about the orbital period and

the system can reach the quasi-steady state because the orbital period is comparable or longer than a few days. In the case of active host stars, the timescale becomes shorter due to the high EUV flux and the system reaches the equilibrium quickly. We also note that the timescale of the transit is a few hours and we cannot estimate the effect of the EUV variation due to the eccentric orbit from the observations.

We also examine the wind effect on the mass loss and find that the mass-loss rate of the planet is independent of the strength of the stellar wind unless the stellar wind is strong enough to confine the upper atmosphere at the launching point. The mass-loss rates in our simulations are around $\sim 2 \times 10^{10}$g/s as shown in Table 4.2. We run an additional simulation with $\dot{M}_* = 1000\dot{M}_\odot$ to investigate the extreme environment although the observations of the stellar wind suggest such wind may be unlikely. An extremely intense stellar wind $\dot{M}_* > 1000\dot{M}_\odot$ can completely confine the outflow, and the mass-loss rate becomes significantly small in such a case. The base of the outflow is determined by the ionization balance between the EUV photoionization and the radiative recombination:

$$\frac{F_{EUV}}{h\nu_0}\sigma_{\nu_0} n_{\rm HI,base} \sim n^2_{\rm HII,base}\alpha_{\rm rec} \tag{4.5}$$

The base density of the wind is proportional to the square root of the EUV flux. The intense EUV radiation can launch a strong outflow that absorbs the stellar lines and the confinement effect becomes relatively small. The extremely strong stellar wind $\dot{M}_* > 1000\dot{M}_\odot$ can confine the planetary outflow to the launching point, but unrealistically strong winds are required to confine the outflow completely in the case of young stars which emit intense EUV flux.

Transit signals can be used to observe the existence of the escaping outflow and the thermo-chemical structure of the upper atmosphere. Recent Lyman-α observations have revealed the existence of close-in planets without Lyman-α absorption although the EUV flux is strong. The quantitative understanding of such Lyman-α non-detection condition is necessary to know the structure of the upper atmosphere from the recent observations. To interpret the recent transit observations, we calculate the transit depth using the atmospheric structure of our simulations with the stellar wind effect.

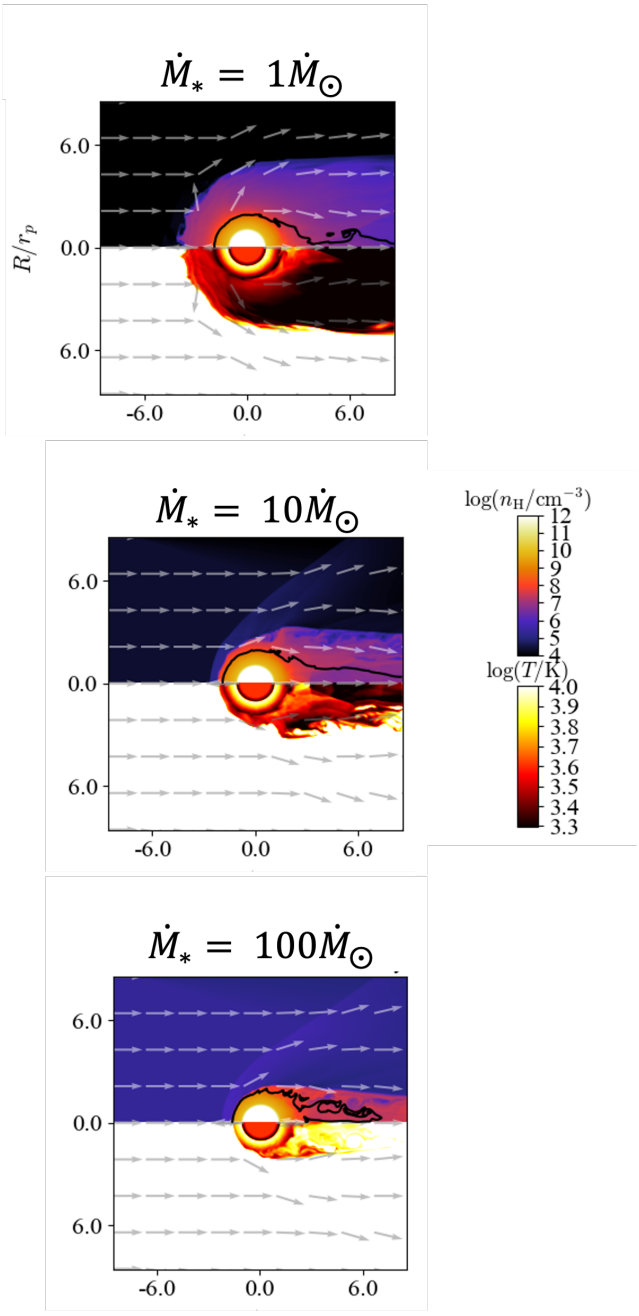

Fig 4.1: Our results of simulations with $\dot{M}_* = 1\,\dot{M}_\odot, 10\,\dot{M}_\odot, 100\,\dot{M}_\odot$ stellar wind from the host star at $t = 5.8$ day after the initial conditions. EUV radiation and the wind from the host star are injected from the left side of each panel. The density is given in the upper half, the temperature is shown in the lower half, and the arrows denote the gas velocity. The solid lines in upper panels show neutral hydrogen abundance becomes 0.9.

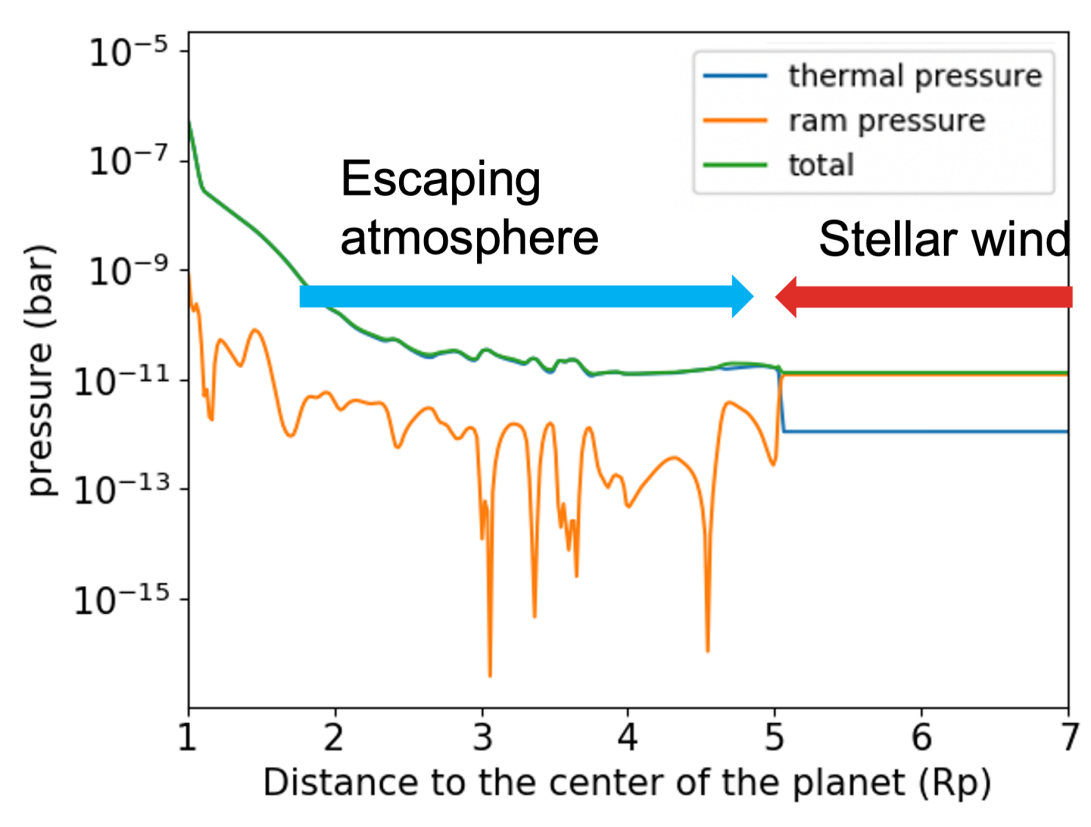

Fig 4.2: Pressure radial profile of our fiducial model ($\dot{M}_* = 1\dot{M}_\odot$). The thermal pressure (blue) of the outflow dominates in inner region and the ram pressure (orange) of the stellar wind dominates the total pressure (green) in the outer region.

Table 4.2: Planetary Mass-loss rates with different stellar winds

Stellar Wind strength	Mass-loss rate (g/s)
$1\,\dot{M}_\odot$	2.9×10^{10}
$10\,\dot{M}_\odot$	2.2×10^{10}
$100\,\dot{M}_\odot$	2.3×10^{10}

4.2.1 Lyman-α transit signal

Lyman-α absorption has been used to observe the planetary outflows since shortly after the beginning of observations of exoplanets (Vidal-Madjar et al. 2003; Ben-Jaffel and Sona

Hosseini 2010; Koskinen et al. 2010; Bourrier and Lecavelier des Etangs 2013). The hydrodynamics simulations have been used to interpret the observed Lyman-α absorption (e.g. Murray-Clay et al. 2009; Tripathi et al. 2015; Christie et al. 2016; Allan and Vidotto 2019; Carolan et al. 2020).The wavelength of Lyman-α is 121.6 nm and in ultraviolet. The absorption by neutral hydrogen atoms in the the ground state contributes to the transit signal. We explain the calculation of the transit depth in general. The procedure have been used for different studies (e.g. Allan and Vidotto 2019). The transit depth δ_ν is given as:

$$\delta_\nu = \frac{\int 2\pi R(1 - e^{-\tau_\nu})\mathrm{d}R}{\pi R_*^2} \tag{4.6}$$

where τ_ν is the optical depth at frequency ν. The optical depth is given as:

$$\tau_\nu = \int n_i \sigma \phi_\nu dz \tag{4.7}$$

where σ is the absorption cross-section at the line center, ϕ_ν is the line profile, and n_i is the number density of absorber. In the case of planetary atmosphere, at a certain altitude, the optical depth exceeds one and becomes optically thick. The cross-section is given as:

$$\sigma = \frac{\pi e^2 f}{m_e c} \tag{4.8}$$

where f is the oscillator strength of the transition (Lyman-α;$f = 0.41641$, Hα;$f = 0.64108$ from NIST Catalog) and c is the speed of light. The Voigt line profile is given by a convolution of a Gaussian and a Lorentz distribution.

$$\phi_\nu \propto \int_{-\infty}^{\infty} \frac{e^{-x^2}}{\chi^2 + (\Delta u / u_{\rm th} - x)^2} dx \tag{4.9}$$

where $u_{\rm th} = \sqrt{2k_B T / m_H}$ is the thermal velocity and χ is the damping parameter.

We explain the wind effect of the Lyman-α absorption in this section. The transit depth is proportional to the square of the effective radius of the planet, and we detect $n_{\rm HI} \sim 10^2\,{\rm cm}^{-3}$ by Lyman-α. If we assume that the ionization degree is about $\sim 10^{-2}$, we observe $n_{\rm H} \sim 10^4\,{\rm cm}^3$ by Lyman-α absorption and we can see that such an upper atmosphere of escaping outflow is confined by the wind in Figure 4.1. Figure 4.3 shows the Lyman-α transit depth of our simulations. The confinement by the strong wind reduces the Lyman-α transit depth and the depth strongly depends on the stellar wind strength. The peak is blue-shifted by ~ 10 km/s due to the wind pressure. $10\dot{M}_\odot$ wind can reduce the Lyman-α by half. Our results suggest that the outflow may be affected by the strong

wind in the case of Lyman-α non-detected close-in planets. We note that the transit depths are time-dependent and vary a few 10%. Such absorption by the tail may affect the transit signal of close-in planets with relatively weak EUV radiation from the host star.

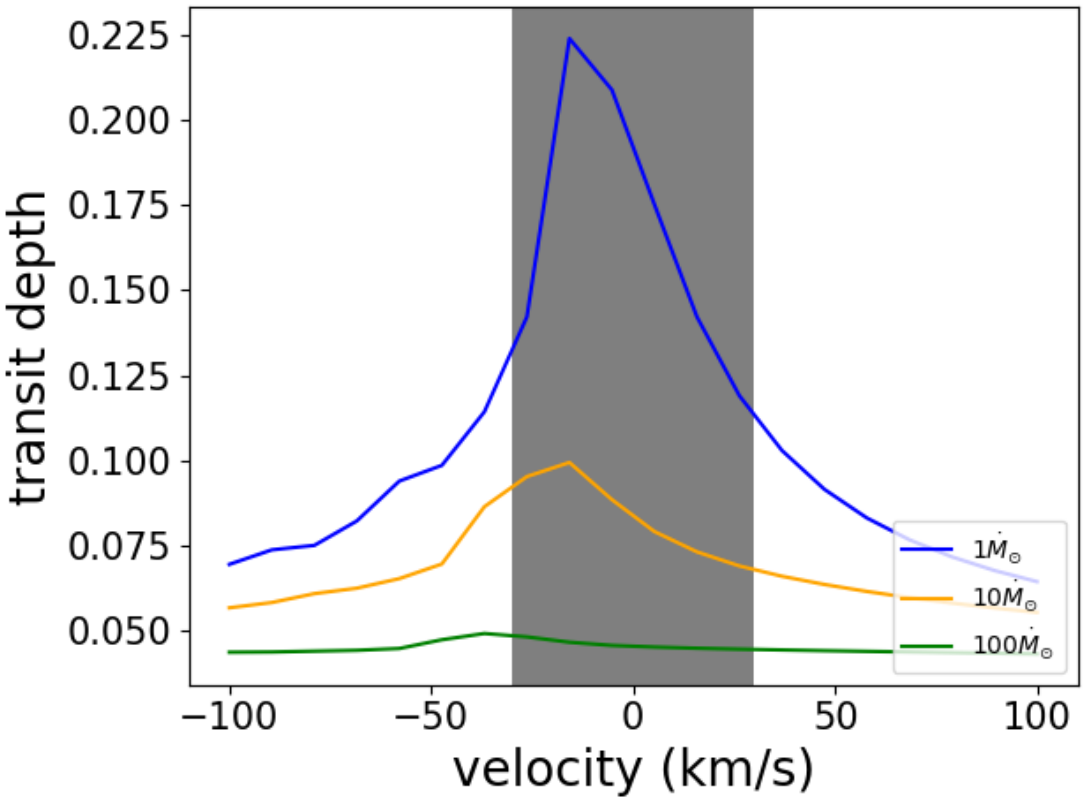

Fig 4.3: The Lyman-α transit depths for different stellar wind strengths ($\dot{M}_* = 1\,\dot{M}_\odot, 10\,\dot{M}_\odot, 100\,\dot{M}_\odot$). The shaded region indicates the line center ($-30\,\mathrm{km/s} < v < 30\mathrm{km/s}$). The peaks are blue-shifted due to the stellar wind.

We assume 2D axissmmetry in our simulations as in the previous chapter. The contribution from the tail structure can be significant. The tail scale length can be given as:

$$R_t = \frac{u}{\Omega} \tag{4.10}$$

where u is the velocity of the outflow and Ω is the angular velocity of the planet. The ratio R_t is typically a few planetary radii, which can be large enough to absorb the Lyman-α

emission from the star. We assume that the tail size is R_t and the impact parameter $b = 0$. We can assume that the density of the tail to be similar to the density behind the planet in our simulations, and the ionization fraction can be estimated from the ionization equilibrium. The Lyman-α cross section is $\sim 8 \times 10^{-18}\,\mathrm{cm}^2$ and the density of the tail is $\sim 10^6\,\mathrm{cm}^{-3}$. The tail is nearly fully ionized with $X_{\mathrm{HI}} \sim 10^{-2}$ because of the intense EUV radiation.

4.2.2 Hα transit signal

The Lyman-α transit absorption depth can be observed by the space telescope and cannot be observed in some cases. This makes it difficult to observe the Lyman-α absorption although the transit depth itself is very large. Future observations have been performed by the lines which can be observed by ground-based telescopes. The Hα absorption is one of the example of such signals which observed by ground-based telescopes. For future observations, it is necessary to study the effect of the stellar wind on the Hα absorption. The line center of the Hα emission is not absorbed by ISM, in contrast to the Lyman-α transit observation. The upper atmosphere, which absorbs the Hα, does not provide direct evidence of atmospheric escape because it exists within the Roche lobe, but on the other hand, understanding the structure of the upper atmosphere from the Hα observations can provide insight into the escaping atmosphere.

The population of excited hydrogen at $n = 2$ depends on collisional and radiative processes. There is a detailed non-LTE scheme for stellar atmospheres (Munafò et al. 2017). In the collisional processes, collisional excitation and de-excitation due to the collisions with electrons, protons, and neutral hydrogen atoms contribute to the population. In the radiative processes, the contribution of the bound-bound, bound-free, and free-free radiative transitions should be considered. It is difficult to implement these processes in our hydrodynamics simulations because the large number of the related transitions of multi-levels significantly increases the computational cost. Such detailed calculations can be performed in 1D. In the observational transit signals of the planetary wind, the multi-dimensional geometry should be taken into account. Therefore, we adopt the post-processing to calculate the level population.

We calculate the $n = 2$ level population in order to obtain Hα transit depth. In our hydrodynamic code, we have not considered the level population as we mentioned. We

calculate the population using the $2p, 2s$ population of Christie et al. 2013:

$$\begin{aligned}\frac{n_2}{n_1} = \frac{n_{2p}+n_{2s}}{n_1 s} &\simeq 10^{-9}\left(\frac{5R_*}{a}\right)^2 e^{16.9-(10.2\,\mathrm{eV}/k_B T_{\mathrm{Ly}\alpha,*})} \\ &+ 1.627\times10^{-8}\left(\frac{T}{10^4\,\mathrm{K}}\right)^{0.045} e^{11.84-118400\,\mathrm{K}/T} \\ &\times \frac{8.633}{\log(T/T_0)-\gamma}\end{aligned} \tag{4.11}$$

where $T_{Ly\alpha,*} \sim 7000\,\mathrm{K}$ is the excitation temperature for the solar Lyman-α, $T_0 = 1.02\,\mathrm{K}$ and $\gamma = 0.57721\ldots$ is the Euler-Mascheroni constant. The 2s level population is larger than $n = 2$p level in the high temperature ($> 5000\,\mathrm{K}$) region and $n = 2$ abundance is about 10^{-9} in the planetary atmosphere of our simulations. In the Lyman-α transit depth, we neglect the $n = 2$ level population considering the much greater population of the $n = 1$ ground state. After we get the density of hydrogen atoms at level $n = 2$, we can calculate the optical depth for Hα as we calculate in Lyman-α transit depth. We detect the atmosphere $n_{\mathrm{H}} \sim 10^{12}\,\mathrm{cm}^{-3}$ by Hα transit.

Figure 4.4 shows the Hα transit depth of our simulations. Due to the small amount of hydrogen at the $n = 2$ level, the transit depth at the line center is quite smaller than that of Lyman-α. The transit depth at the line center is about 1% in our simulations. These values are in agreement with the observations of close-in planets (HD 189733 b;Jensen et al. 2012; Cauley et al. 2017, KELT-9b; Yan and Henning 2018, KELT-20b; Casasayas-Barris et al. 2018, HAT-P-32 b; Czesla et al. 2022, WASP-121b; Cabot et al. 2020, WASP-33b; Yan et al. 2021, WASP-52b; Chen et al. 2020). The absorption depth of Hα is almost independent of the strength of the wind. The relatively lower part of the atmosphere contributes to the absorption because the amount of hydrogen atoms at the $n = 2$ level is quite small in the upper part where the ground state hydrogen can absorb Lyman-α. The difference in the dependence of Hα and Lyman-α on the stellar wind strength helps to determine the stellar wind parameters and EUV flux. We cannot determine the EUV flux and the stellar wind strength without Hα.

We can estimate the EUV luminosity from the transit depth of Hα because the transit depth depends only on the EUV flux from the host star. The non-detection of Lyman-α transit is not the evidence of the absence of the atmospheric escape and future observations of Hα transit can reveal the presence of escape and the wind environment for close-in planets without Lyman-α absorption. The typical transit depth of Hα is ~ 0.01 and the observational error in Hα absorption is about a few 10% (Jensen et al. 2012; Czesla et al. 2022). The EUV flux from the Hα observations and hydrodynamic model has an error of a

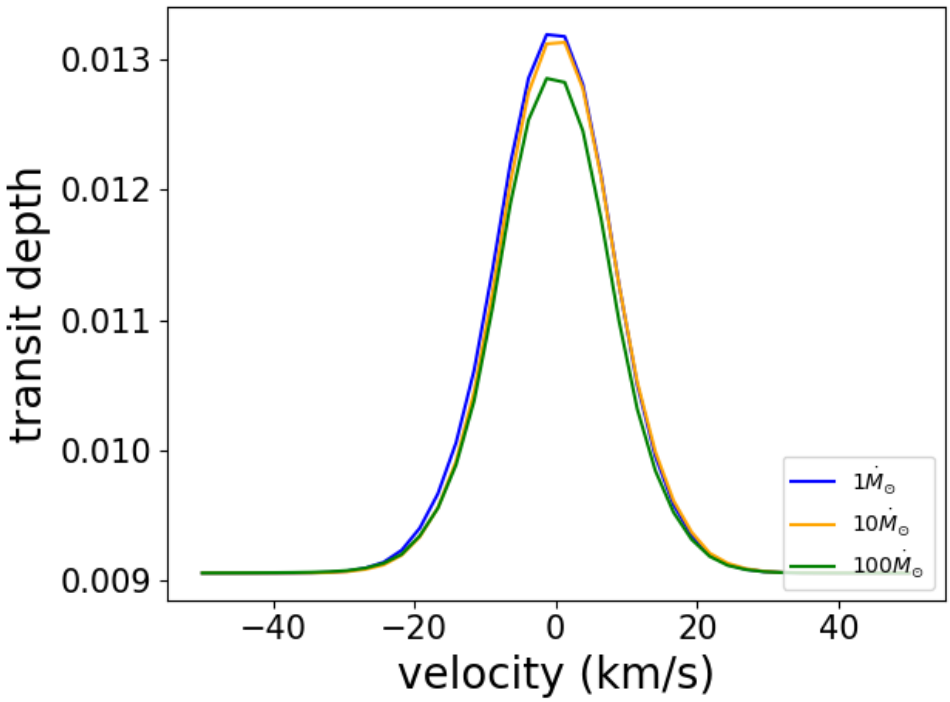

Fig 4.4: The Hα transit depths calculated using our simulation outputs similar to the Lyman-α transit depth.

few 10%. The Lyman-α transit depth depends on the stellar wind strength and the EUV flux. The observational error of the Lyman-α absorption is typically $10-50$ %. The stellar wind strength obtained from our model may have an error of up to one order of magnitude. We can obtain the information about the stellar wind from the Lyman-α transit depth and the EUV flux from the Hα. Figure 4.5 shows the relationships between the observed transit depth and the stellar properties. If Hα absorption is strong, the EUV flux is strong, and if Hα is weak, the EUV flux is also weak. Furthermore, in the former case, a strong Lyman-α indicates a weak stellar wind, and a weak Lyman-α absorption indicates the existence of the strong stellar wind. Our model suggests that the combination of Lyman-α and Hα transits is important for understanding the upper atmosphere of close-in exoplanets.

We also note that, in the case of Hα, the $n = 2$ level population is extremely small in the thin tail and the tail contribution can also be negligible. Our calculated Hα depths

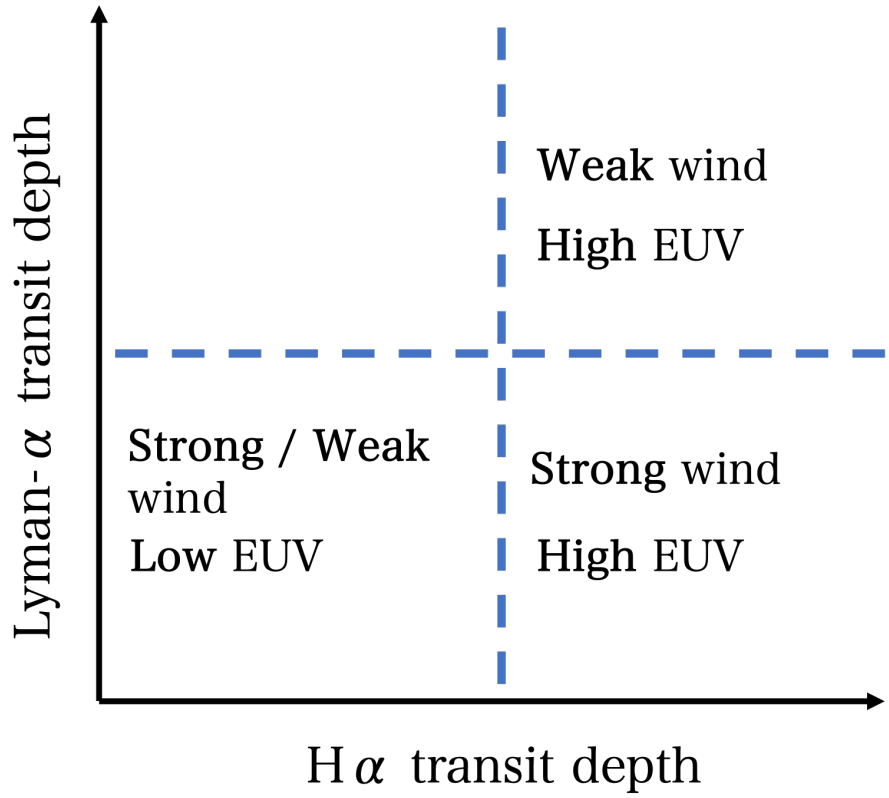

Fig 4.5: The schematic plot of the observational transit depth and the stellar properties (EUV flux and stellar wind strength).

are thus realistic even though we neglect the tail-like structure bent by the Coriolis force in the calculations.

4.2.3 Other lines

As we introduce in Chapter 2 , recent observations by ground-based telescopes have used the helium triplet lines to track the planetary outflow. To obtain the transit signals from the atmospheric structure, we should obtain the population of helium similar to the Hα case. There are several planets with helium absorption in transit (GJ 3470b; Palle et al. 2020; Ninan et al. 2020, WASP-69b; Nortmann et al. 2018, HD 189733 b; Guilluy et al. 2020, HD 209458 b; Alonso-Floriano et al. 2019, HAT-P-32 b; Czesla et al. 2022). There are

many radiative transitions and collisional transitions in the helium energy levels Figure 4.6.

Our radiative hydrodynamics simulations have not included the level population of helium atoms. We estimate the level population by the post-process. We follow the transition rates in detailed calculation (Oklopčić and Hirata 2018). The transition coefficients of collisions with electrons can be given as

$$q_{ij} = 2.1 \times 10^{-8} \sqrt{\frac{13.6\,\mathrm{eV}}{kT}} \exp\left(-\frac{E_{ij}}{kT}\right) \frac{\Upsilon_{ij}}{\omega_i} \tag{4.12}$$

and the values in the helium transitions are $q_{13a} = 4.5 \times 10^{-20}\,\mathrm{cm^3\,s^{-1}}, q_{31a} = 2.6 \times 10^{-8}\,\mathrm{cm^3\,s^{-1}}, q_{31b} = 4.0 \times 10^{-9}\,\mathrm{cm^3\,s^{-1}}$. The transition coefficient of collision with neutral hydrogen atoms is given as $Q_{31} \sim 5 \times 10^{-10}$. And the radiative transition from the metastable to the ground state is slow $A_{31} = 1.272 \times 10^{-4}\,\mathrm{s^{-1}}$. The photoionization of the metastable and the ground state of helium plays an important role in the population of 2^3S triplet in which the helium atoms absorb 10830 Åphotons. The photon with $h\nu > 24.6$eV can photoionize the ground state helium and $h\nu > 4.8$eV photon can ionize the helium in the triplet state. The EUV photons with $h\nu > 24.6$eV increase the metastable helium and the FUV photons with $h\nu > 4.8$eV decrease the metastable helium. The helium 10830Åabsorption is not observable in close-in planets around hot stars with strong FUV luminosity.

The photoionization cross section of the helium at the ground state is given as Brown 1971:

$$\frac{\sigma_{\mathrm{He}}}{\sigma_{\mathrm{H}}} = \begin{cases} 6.53(h\nu/24.6\,\mathrm{eV}) - 0.22 & (24.6\,\mathrm{eV} < h\nu < 65.4\,\mathrm{eV}) \\ 37.0 - 19.1(h\nu/65.4\,\mathrm{eV})^{-0.76} & (65.4\,\mathrm{eV} < h\nu < 1\,\mathrm{keV}) \end{cases} \tag{4.13}$$

where σ_{H} is the photoionization cross section of hydrogen atoms. We assume that the number of the photoionization photons of helium (40 eV) is 3×10^{13}. The photoionization rate is about $\Phi_1 \sim 8 \times 10^{-5}\,\mathrm{s^{-1}}$.

We use the photoionization cross section for metastable helium from Norcross 1971. We assume the photospheric spectrum $T_{eff} = 5800\,\mathrm{K}, \log g = -4.5$ of the data from Husser et al. 2013 and find the photoionization rate for $a = 0.05$ AU is $\phi_2 \sim 3\,\mathrm{s^{-1}}$. The recombination coefficients are $\alpha_1 = 1.54 \times 10^{-13}\,\mathrm{cm^3\,s^{-1}}, \alpha_2 = 1.49 \times 10^{-14}\,\mathrm{cm^3\,s^{-1}}$ from Osterbrock and Ferland 2006. If we assume the steady state, the transition rate should be balanced. We assume that the attenuation of the UV is negligible in the above photoionization rates. We can also neglect the contribution of electrons from the photoionization of helium atoms due to the small abundance.

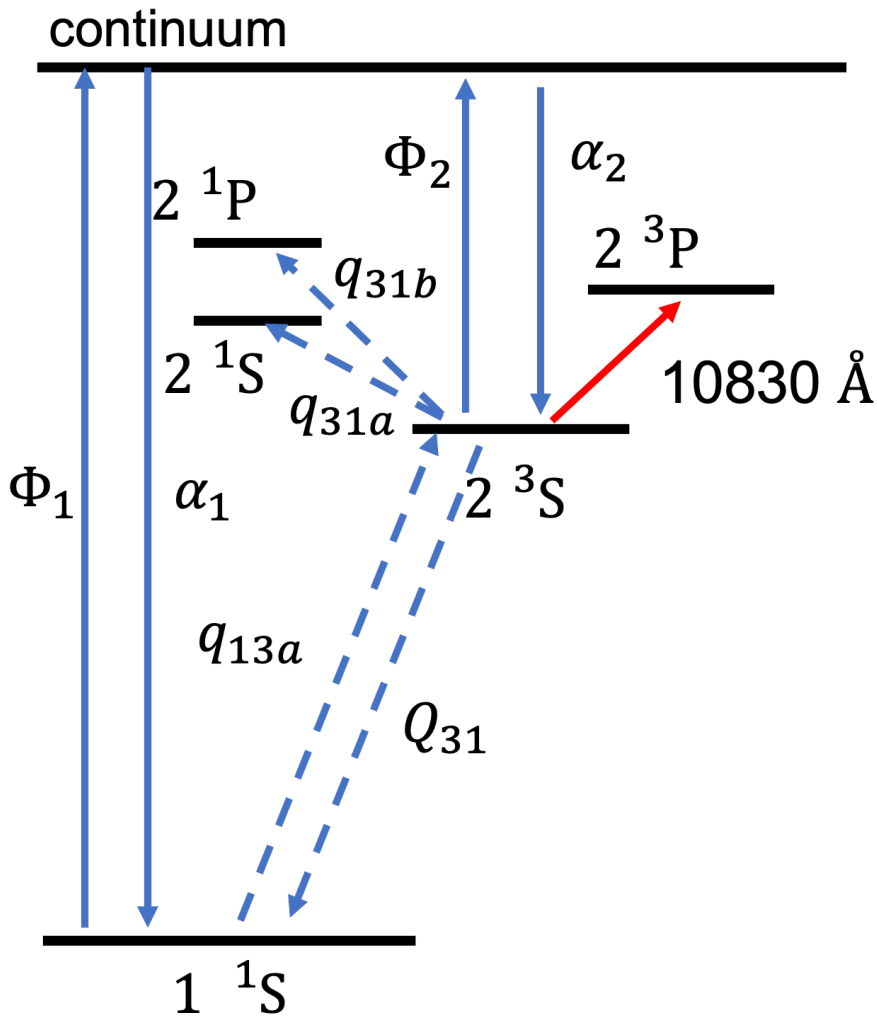

Fig 4.6: The energy structure of Helium atoms. The solid arrows show the radiative transitions and the dashed arrows show the transition due to collisions.

Figure 4.7 shows the transit depth for helium 10830Åabsorption. The depth depends on the stellar wind strength. The transit depth in the solar wind case is larger than Hα and similar to the previous study without stellar wind (Oklopčić and Hirata 2018). The stellar wind strength dependence of helium absorption is between Hα and Lyman-α because the intermediate layer contributes to the absorption.

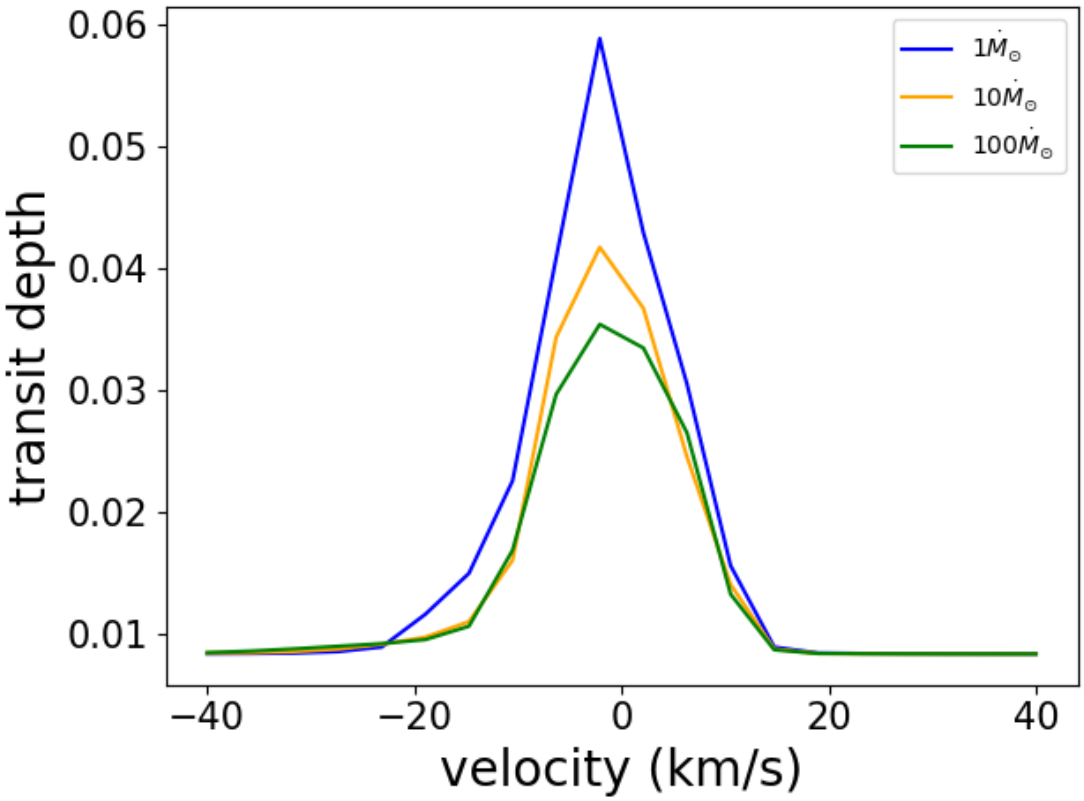

Fig 4.7: The Helium triplet transit depths calculated using our simulation outputs similar to the Lyman-α transit depth.

Recent observations have revealed the existence of other heavy elements in the upper atmosphere of hot Jupiters (Ba, Azevedo Silva et al. 2022). The existence of such heavy elements may suggest the strong outflow in the ultra-hot gas giants. In the previous chapter, we investigate such a strong outflow driven by intense FUV radiation. The strong wind may also suppress the metal line absorptions. In the future study, detailed hydrodynamics simulations with heavy elements and stellar wind confinement can be used to reveal the structure of the upper atmosphere.

4.3 The effect of the time dependence of the stellar activity and the magnetic fields

The stellar activities are time-dependent. Such activities change the shape of the planetary outflow. The frequency of strong flares can be estimated from observations. The strong flare activities are associated with coronal mass ejections (CMEs). The mass ejection changes the shape of the outflow by its ram pressure like stellar winds.

If we focus on the flare frequency $f(E_{\rm flare})$, which corresponds to the flares that can confine the upper atmosphere and reduce the absorption during the transit ($E_{\rm flare} > 10^{32}\,{\rm erg}$), the occurrence rate is estimated by using the power-law relationship $f(E_{\rm flare}) \propto E_{\rm flare}^{-2}$ (Maehara et al. 2017),

$$\int_{10^{32}\,{\rm erg}}^{\infty} f(E_{\rm flare})\,{\rm d}E_{\rm flare} \sim 1 - 100\,{\rm year}^{-1} \tag{4.14}$$

The probability of observing a transit during a flare is less than 1% even if we consider all the flare activities, which can cause an order of magnitude larger mass loss than the solar steady wind. Even though the CME activity in the other stars may be less intense (Leitzinger et al. 2014), it can still be substantial in extremely young active systems. Young stars are more likely to have powerful flares than older stars because they are more active (Feinstein et al. 2020). This may only be significant if the age is less than 50 Myr. The spectral type of the star also affects the frequency of powerful flares. The rate is several orders of magnitude higher for M dwarfs than for G-type stars. This shows that severe flares are common around M dwarfs and that CMEs affect the Lyman-α transit almost every time it passes across. Strong stellar activity can reduce the Lyman-α transit around K- and M-type stars, but the Hα transit can still be seen.

Because of ionization, the magnetic field may also have a significant impact on planetary outflows and stellar winds. The planetary magnetic field's pressure is less intense than the outflow's thermal pressure in the case of rocky planets (Zhang et al. 2021). The effect of the planetary magnetic field has been investigated in previous studies using magneto-hydrodynamics models of hot Jupiters (Matsakos et al. 2015; Carolan et al. 2021a; Odert et al. 2020; Villarreal D'Angelo et al. 2018). We can use the ratio of the pressure of outflow to the magnetic pressure to investigate the effect of the planetary magnetic fields. For a magnetic field of $\sim 10\,{\rm G}$, the magnetic pressure is $P_B \sim 1\,\mu{\rm bar}$. A strong magnetic field like Jupiter can suppress the wind confinement effect on the planetary outflow. Detailed simulations with a radiative transfer are needed to evaluate the wind effect with the strong planetary magnetic field, as suggested by Cauley et al. 2019.

The stellar magnetic field also enhances the pressure of the wind. The interaction between the magnetized wind and the planetary outflow is highly complex and variable (Harbach et al. 2021). When the planet crosses the current sheet, the magnetic and dynamical pressure changes by up to an order of magnitude. The detailed 3D magnetohydrodynamic model (Garraffo et al. 2017) has revealed that the magnetic pressure dominates in the case of inner planets such as TRAPPIST-1b ($a = 0.01$ AU) and the dynamic pressure dominates in the case of the outer planets such as TRAPPIST-1h ($a = 0.06$ AU). The effect of the stellar magnetic field can be estimated as we introduced in Chapter 2. The strength of the field can be given as:

$$B \sim B_0 \left(\frac{R_0}{r}\right)^3 \tag{4.15}$$

where B_0 is the surface field strength. The magnetic pressure of stellar magnetic field around planets can be given as:

$$P_{B_*} \sim 2.5 \times 10^{-14}\,\mathrm{bar} \left(\frac{B_*}{1\,\mathrm{G}}\right)^2 \left(\frac{a}{0.05\,\mathrm{AU}}\right)^{-6} \left(\frac{R_*}{R_\odot}\right)^6 \tag{4.16}$$

The pressure strongly depends on the semi-major axis, and the pressure for typical hot Jupiters around the solar-like star is less than the ram pressure of the wind. If the semi-major axis is quite small $a \sim 0.015\,\mathrm{AU}$, the magnetic pressure exceeds the ram pressure. For such planets, the magnetic field also confines the escaping outflow and the Lyman-α transit signal may decrease. It seems difficult to confine the escaping outflow to the planetary surface for the magnetic field because the pressure of the outflow is around $> 10^{-9}$ bar and the very small orbital separation $a < 0.01\,\mathrm{AU}$ is required if we assume the solar magnetic field. We can neglect the planetary magnetic field as an origin of the pressure confinement unless the host star is magnetically active and/or the planets are very close-in. However, the magnetic field may change the geometry of the wind and the outflow. In this sense, further detailed simulations may reveal the detailed geometry of the outflow.

4.4 Summary

In this chapter, we investigate the geometry of the outflow that determines the transit absorption signals using radiation hydrodynamics simulations that include the stellar wind in a self-consistent manner. The stellar wind confines the escaping outflow by the ram pressure. The balance between the thermal pressure of the outflow and the ram pressure

of the wind determines the shape of the outflow. We find that the Lyman-α transit signal depends on the strength of the wind because the confinement reduces the effective radius. Extremely strong wind $\dot{M}_* > 100\dot{M}_\odot$ significantly suppresses the Lyman-α absorption. We also investigate the Hα transit depth because the Lyman-α transit cannot be observed by ground-based telescopes. We find that the Hα absorption is almost independent of the strength of the wind. The contribution from the upper region is small in the case of Hα, in contrast to Lyman-α due to the small amount of the excited hydrogen atoms in the upper atmosphere. The absorption depth of both lines depends on the strength of the EUV flux from the host star because the escaping outflow becomes strong if the EUV flux is strong. If we use only the Lyman-α transit signal, the strength of the wind and the EUV flux degenerate. We can use the Hα absorption signal in addition to Lyman-α to solve the degeneracy. We also investigate the effect of stellar activity on the observational signal. The CMEs may have impacts on the observations by the confinement. The activity is time-dependent and the frequency depends on the stellar type. We find that in the case of M-dwarfs, which can be very active, the CMEs can confine the atmosphere very frequently and the observational signals can be affected by almost every transit.

Chapter 5

Physical conditions of the planetary wind

In this chapter, we discuss the physics of the escaping atmosphere which determines the thermo-chemical structure and the transit signals. One of the goals of this chapter is to determine which of the many exoplanets are most affected by stellar winds, based on a physical understanding. We only consider EUV photoionization heating because FUV heating processes become dominant around hot stars, and EUV heating dominates planets around solar-type stars as discussed in Chapter 3. Finally, we discuss the planetary evolution with the mass loss driven by intense UV radiation from the host star.

5.1 Relevant physics of the atmospheric escape

The physics of the escaping outflow is determined by photoheating, gravity, and gas expansion. Despite many radiation hydrodynamics simulations, the physics of mass loss due to the UV heating under various conditions is not well understood. We introduce the typical timescales for these physical effects in order to understand the physics in the upper atmosphere heated by EUV photons.

We can define the gravitational temperature from the planetary mass as:

$$kT_g = \frac{GM_p \mu m_{\rm H}}{R_p} \tag{5.1}$$

The temperature indicates the strength of the planetary gravity. The sound speed at the gravitational temperature is equal to the escape velocity around the planet. The equilibrium temperature T_{eq} can be determined from the balance of the photoheating and

the cooling

$$\frac{F_{\rm EUV}}{h\nu}\sigma_\nu n_{\rm HI} \sim n_{\rm HII}^2 \tag{5.2}$$

$$\Lambda_{{\rm Ly}\alpha} \sim F_{\rm EUV}\sigma_\nu n_{\rm HI} \tag{5.3}$$

From these equations, the equilibrium temperature becomes $\sim 10^4$ K for EUV photoionization heating of hydrogen atoms. This equilibrium temperature is same as the temperature of photoionized gas in other astrophysical situations such as ISM. The real gas temperature of the system cannot exceed the equilibrium temperature. We can also define the gravitational radius using the sound speed at the equilibrium temperature $c_{\rm eq}$ as:

$$R_g = \frac{GM_p}{(c_{\rm eq} = 10\,{\rm km/s})^2} \tag{5.4}$$

The gravitational radius represents the place where the planetary gravity can retain the gas with the temperature $T_{gas} = T_{eq}$. If the gas at the equilibrium temperature is in the upper layers above this radius, it can easily escape against the planet's gravity.

Finally, we can define the " characteristic temperature" $T_{\rm ch}$ (Begelman et al. 1983) as:

$$kT_{\rm ch} = \frac{\Gamma}{c_p/\mu m_{\rm H}}\frac{R_p}{c_{\rm ch}} \tag{5.5}$$

where Γ is the photoheating rate, and c_p is the specific heat at constant pressure. The right-hand side represents the deposited EUV energy in the characteristic sound crossing time. In the original work, the characteristic temperature has been used for the coronae of accretion disks driven by Compton heating. The characteristic temperature represents the temperature that the gas reaches before it expands to about the planetary radius in the absence of cooling. The temperature can exceed the equilibrium temperature but this does not mean that the real gas temperature becomes larger than $T_{eq} = 10^4$ K. The characteristic sound speed $c_{\rm ch}$ is given as:

$$c_{\rm ch} = \left(\frac{\Gamma R_p}{c_p}\right)^{1/3} \tag{5.6}$$

The typical value of the sound speed in the upper atmosphere is ~ 10 km/s. The characteristic temperature represents how rapid the photoheating is compared to the gas expansion and does not mean the typical temperature of the system. In the case of EUV photoiniza-

tion heating of hydrogen atoms, the photoheating rate can be given as:

$$\Gamma = \frac{1-x}{m} F_0 \delta \langle\sigma\rangle \langle\Delta E\rangle \tag{5.7}$$

$$= 1.2 \times 10^7 \,\mathrm{erg\,g^{-1}\,s^{-1}} \left(\frac{1-x}{0.5}\right) \left(\frac{m}{1.4 m_\mathrm{H}}\right) \left(\frac{\Phi}{10^{41}\,\mathrm{s^{-1}}}\right) \tag{5.8}$$

$$\times \left(\frac{r}{1\mathrm{au}}\right)^{-2} \left(\frac{\delta\langle\sigma\rangle\langle\Delta E\rangle}{10^{-18}\,\mathrm{cm^2} \times 1\,\mathrm{eV}}\right) \tag{5.9}$$

where x is the ionization degree, m is the gas mass per hydrogen nucleus, Φ is the EUV photon flux, δ is the attenunation factor, $\langle\sigma\rangle$ is the average cross section of the photoionization and $\langle\Delta E\rangle$ is the average deposited energy per photoionization. The rate depends on the spectral shape. At higher energies, the cross section is smaller but the deposited energy increases, so these effects cancel each other out overall.

The ratio between T_ch and T_eq is

$$\frac{T_\mathrm{ch}}{T_\mathrm{eq}} = \left(\frac{R_p \Gamma}{c_\mathrm{eq}^3 c_p}\right)^{2/3} = \left(\frac{R_p}{R_g}\right)^{2/3} \left(\frac{\Gamma G M_p}{c_p c_\mathrm{eq}}\right)^{2/3} \tag{5.10}$$

From the second factor, we can define the critical flux as:

$$F_\mathrm{cr} = \frac{m c_p c_\mathrm{eq}^5}{G M_p \sigma \Delta E} \tag{5.11}$$

$$= 5.8 \times 10^{12}\,\mathrm{cm^{-2}\,s^{-1}} \left(\frac{m}{1.4 m_\mathrm{H}}\right) \left(\frac{c_\mathrm{eq}}{10\,\mathrm{km\,s^{-1}}}\right)^5 \tag{5.12}$$

$$\times \left(\frac{M_p}{M_J}\right)^{-1} \left(\frac{\sigma_0}{5 \times 10^{-18}\,\mathrm{cm^2}}\right)^{-1} \left(\frac{\Delta E}{1\,\mathrm{eV}}\right)^{-1} \left(\frac{c_p}{5/2}\right) \tag{5.13}$$

and the ratio can be given as:

$$\xi = \frac{R_p}{R_g} \tag{5.14}$$

$$\frac{T_\mathrm{ch}}{T_\mathrm{eq}} \sim \xi^{2/3} \left(\frac{F_0}{F_\mathrm{cr}}\right)^{2/3} \tag{5.15}$$

$$\tag{5.16}$$

The parameters $\xi, F_0/F_\mathrm{cr}$ are fundamental to determine the physical conditions of the planetary outflow driven by EUV photoionization heating.

We can also define the photoheating timescale and the gravitational timescale:

$$t_g = \sqrt{\frac{R_p^3}{GM_p}} \tag{5.17}$$

$$t_h = \frac{R_p}{c_{\rm ch}} \tag{5.18}$$

From these timescales, we can also determine the dominant physics. The ratio between the gravitational and photoheating timescales is

$$\frac{t_g}{t_h} = \xi^{5/6} \left(\frac{F_0}{F_{\rm cr}} \epsilon (1-x) \right)^{1/3} \tag{5.19}$$

which represents the relative strength of the gravity to that of the photoheating. ϵ is an attenuation factor which depends on the column density of the hydrogen. If the ratio is larger than unity $t_g/t_h > 1$, the photoheating is faster and the system loses the atmosphere rapidly.

We perform 1D radiation hydrodynamics simulations with the EUV photoionization of hydrogen atoms and the recombination of hydrogen atoms to understand the thermo-chemical structure of the atmosphere. The equations of the 1D spherical symmetry case are given in appendix. In the simulations, we assume that the Lyman-α cooling is the dominant radiative cooling process as in the previous studies (e.g. Murray-Clay et al. 2009). We check that the thermo-chemical structure is similar to that in the previous 1D simulations. We run simulations for the high EUV case ($T_{\rm ch} > T_{\rm eq}$) and the low EUV case ($T_{\rm ch} < T_{\rm eq}$) for typical hot Jupiter ($M_p = 0.7 M_J, R_p = 1.4 R_J$). Figure 5.1 shows the radial profile of the heating and cooling in our simulations. We find that the adiabatic cooling dominates for the case of low EUV cases and the Lyman-α cooling dominates for the case of high EUV planets. $T_{\rm ch}/T_{\rm eq}$ can be used to distinguish the dominant cooling process. The radiative cooling dominant regime is correspond to the recombination-limited flows and the adiabatic cooling dominant regime is correspond to the energy-limited flows. Our criterion can be calculated using only stellar and planetary properties. In the case of typical hot Jupiters, $T_{\rm eq} = T_{\rm ch}$ when the UV flux is $\sim 10^3\,{\rm erg/cm^2/s}$ and this value is in agreement with the previous simulations.

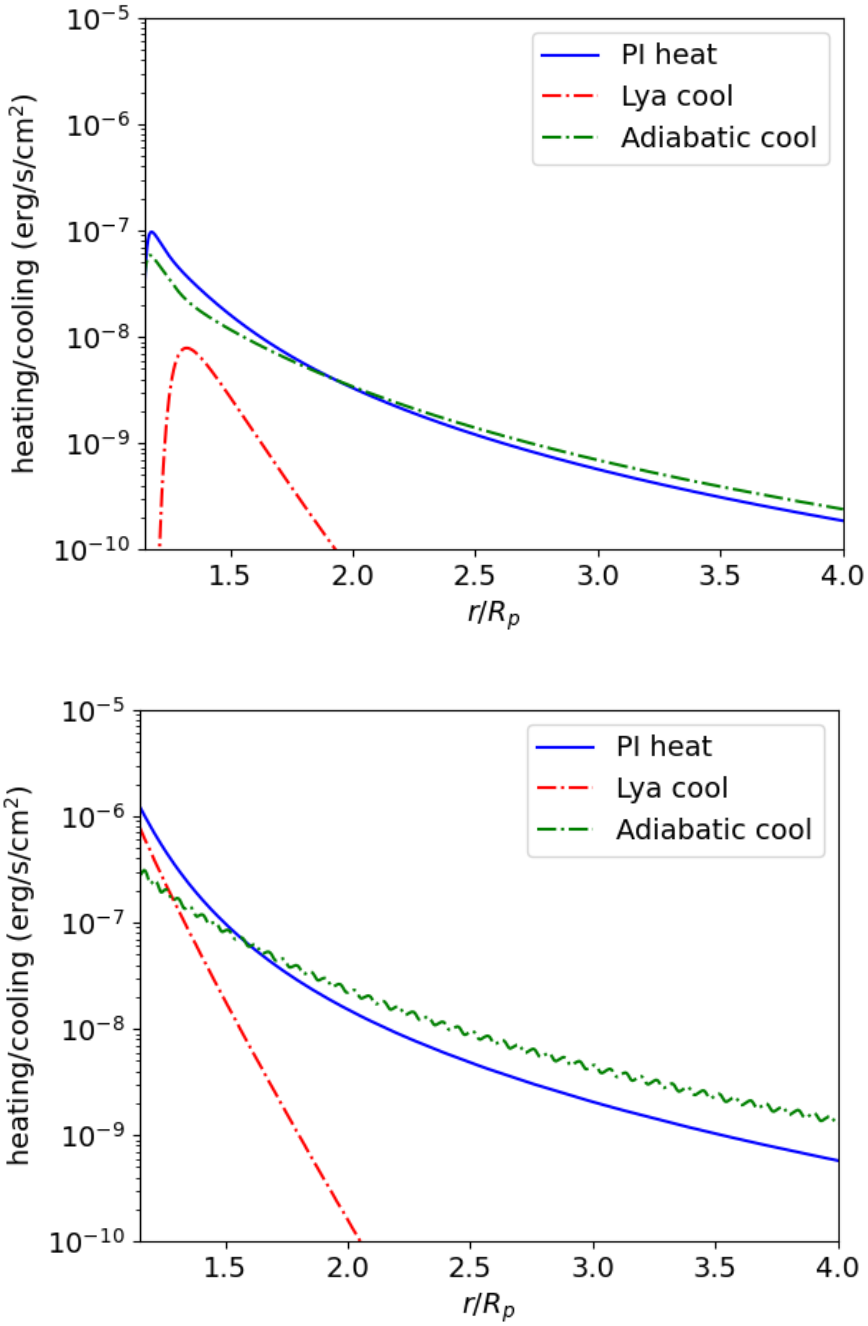

Fig 5.1: Heating and cooling rate profile in low UV planet (top) and high UV planet (bottom). Solid curve shows the photoionization heating. Dashed curves show the cooling rate (red; Lyman-α cooling, greed; PdV work).

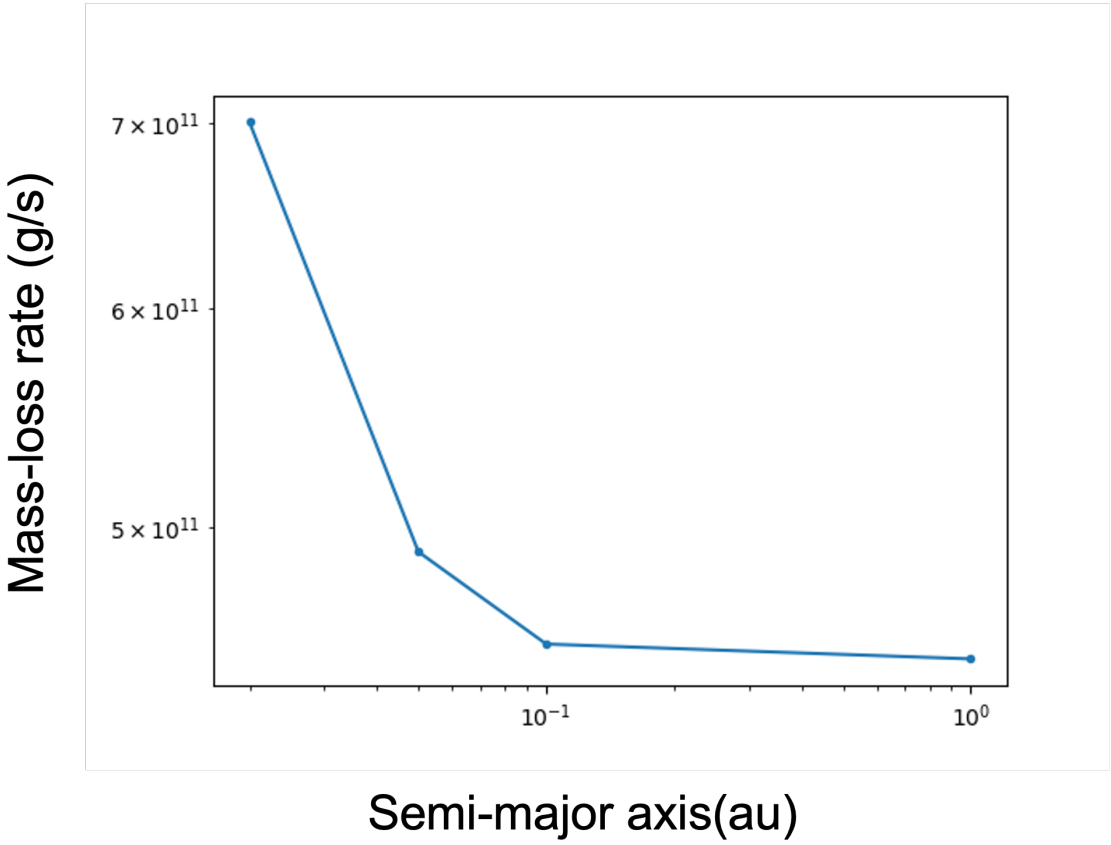

Fig 5.2: Stellar gravity dependence of the planetary mass-loss rate. When the semi-major axis is large, the gravity from the host star is smaller.

As we introduce in Chapter 2, the mass-loss rate also depends on the stellar gravity. We run simulations with the different semi-major axes and fixed other parameters (planetary mass, radius, UV flux, and stellar mass). Figure 5.2 shows the stellar gravity dependence of the planetary mass-loss rates. We should take care of the timescale associated with the stellar gravity. The timescales of the photoheating and the dynamics around the hill radius can be given as:

$$t_{h\_hill} = \frac{R_{hill}}{(\Gamma R_{hill}/c_p)^{1/3}} \tag{5.20}$$

$$t_{dynamics} = \sqrt{\frac{a^3}{GM_*}} \tag{5.21}$$

where R_{hill} is the hill radius. We find that we can use the ratio between the photoheating and dynamical timescales $t_{h\_hill}/t_{dynamics}$ to determine whether the stellar gravity alters the planetary outflow or not. If the ratio is much smaller than the unity (the photoheating timescale is shorter than the dynamical timescale), the photoheating is fast enough, and the stellar gravity cannot enhance the mass-loss rate. We can see that the mass-loss rates become larger within $a < 0.1\,\mathrm{AU}$ and the rates are independent of the semi-major axis if the semi-major axis is larger than $a > 0.1\,\mathrm{AU}$. This is consistent with the condition of the ratio.

We assume the EUV photoionization and neglect the FUV heating and metal line coolings which may affect the temperatures and timescales we have introduced in this chapter. Our model can also be used for planets with non-zero metallicity. As we discussed in Chapter 3, FUV heating is inefficient for close-in planets around cool stars, such as solar-type stars. The characteristic temperature is the same for close-in planets around cool stars, even if we take FUV heating into account. In the case of planets around hot stars, we can neglect EUV photoionization heating and the characteristic temperature is given as:

$$kT'_{\mathrm{ch}} = \frac{\Gamma_{FUV}}{c_p/\mu m_{\mathrm{H}}} \frac{R_p}{c_{\mathrm{ch}}} \tag{5.22}$$

The metal coolings affect the equilibrium temperature. OI cooling can contribute to the cooling rate for metal-rich planets ($Z > 10Z_\odot$). If the metal coolings increase the total cooling rate by factor of 2, the equilibrium temperature decreases and becomes $T'_{\mathrm{eq}} \sim 9500\,\mathrm{K}$. The metal-rich planets tend to satisfy the condition $T'_{\mathrm{ch}}/T'_{\mathrm{eq}} > 1$, and planets around hot stars also tend to have $T'_{\mathrm{ch}}/T'_{\mathrm{eq}} > 1$. The situation becomes complex if we consider the FUV heating and the metal cooling in planets around hot stars. The characteristic temperature in such planets is higher than that in planets without FUV heating. There are several factors that change the equilibrium temperature. The metal line cooling reduces the temperature and FUV heating increases the temperature. In the case of hot stars, the FUV cooling effect is larger than the metal line cooling effect. As we discussed in Chapter 3, the FUV flux is low in the high metallicity stars. This effect also reduces the FUV heating rate by a factor of 2. The photoelectric heating of dust grains is larger for metal-rich systems. If the dust grains are sufficiently abundant in the upper atmosphere, the characteristic temperature becomes higher in metal-rich planets. If the heating due to H_2 pumping and Balmer absorption dominates the heating rate, the presence of metal reduces the characteristic temperature.

5.2 Classification of close-in exoplanets

Two physical conditions can be represented by straight lines in the $\xi - F_0/F_{cr}$ plane. We plot observed exoplanets in $\xi - F_0/F_{cr}$ plane to understand the physical conditions in real systems.

We can use the open-access dataset of observed exoplanets. The dataset includes the planetary parameters (radius, mass, semi-major axis) and the stellar parameters (radius, mass, age, metallicity). It also includes the detected atoms and molecules in the planetary atmosphere. We choose close-in planets (orbital period $P < 10$ day) with the above planetary/stellar parameters except for stellar age because the uncertainty in age is large in general and difficult to determine. The EUV flux is intense in the case of a young host star. We estimate the EUV luminosity using the empirical relationships in Sanz-Forcada et al. 2011:

$$\log L_{\rm EUV} = 29.12 - 1.24 \log \tau \tag{5.23}$$

where τ is the stellar age in Gyr. For stars whose ages were not given in the catalog, we assumed the solar EUV luminosity. We note that the it is difficult to determine the stellar age and the uncertainty is large in many planetary systems in contrast to the mass and radius of the planets. The plot of the $\xi - F_0/F_{cr}$ plane may have a larger error in the F_0/F_{cr} direction than in the ξ direction. Figure 5.3 shows the distribution of the observed exoplanets in the $\log(F_0/F_{\rm cr}) - \log \xi$ plane. The two conditions above can be drawn by two straight lines in the plane. The atmospheric escape in observed planets can be classified into three regions by two lines. Our conditions can be used to distinguish whether the hydrogen-rich atmosphere experience intense mass loss or not. We find that the EUV flux is lower than the critical flux in the case of the two of the Lyman-α non-detected planets and the mass loss is weak. K2-25 b receives intense EUV radiation from the host star and the EUV flux is larger than the critical flux. We plot a few close-in planets do not show the Lyman-α absorption (Lecavelier des Etangs et al. 2012b; Rockcliffe et al. 2021).

If we consider the metal coolings, the straight line of $T_{eq} = T_{ch}$ moves to the bottom side in the $\xi - F_0/F_{cr}$ plane because the equilibrium temperature slightly decreases with the metallicity. In general, the observational error of EUV flux is larger than the effect of FUV heating and metal line coolings on the equilibrium temperature and the characteristic temperature.

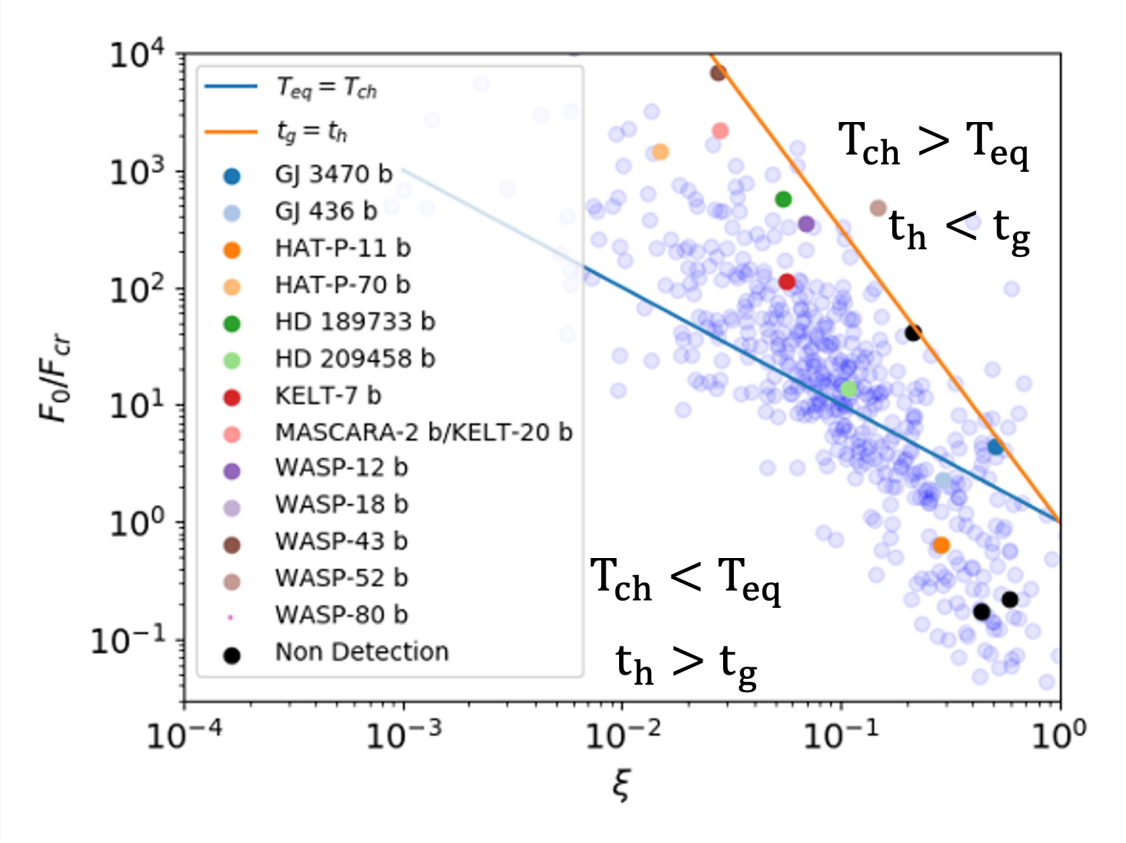

Fig 5.3: The observed planets in $\xi - F_0/F_{cr}$ plane. The colored points show the atomic hydrogen detected close-in planets. Three black points show the Lyman-α non-detected close-in planets. Blue points represent planets without the detection of hydrogen atoms in the dataset. We note that the planets of blue points does not show the Lyman-α absorption detection. Two lines show the physical conditions we introduced (Blue $T_{eq} = T_{ch}$, Orange $t_g = t_h$).

We also try the physical condition with the timescale around the hill radius in observed close-in planets. Figure 5.4 shows the observed planets with the ratio between the timescale of photoheating t_{h_hill} and dynamics $t_{dynamics}$ around the hill radius. The timescale around the hill radius can be used to distinguish whether the stellar gravity affects the atmospheric escape or not. In the case of short period planets, the timescale of photoheating t_{h_hill} is shorter than the dynamics timescale $t_{dynamics}$.

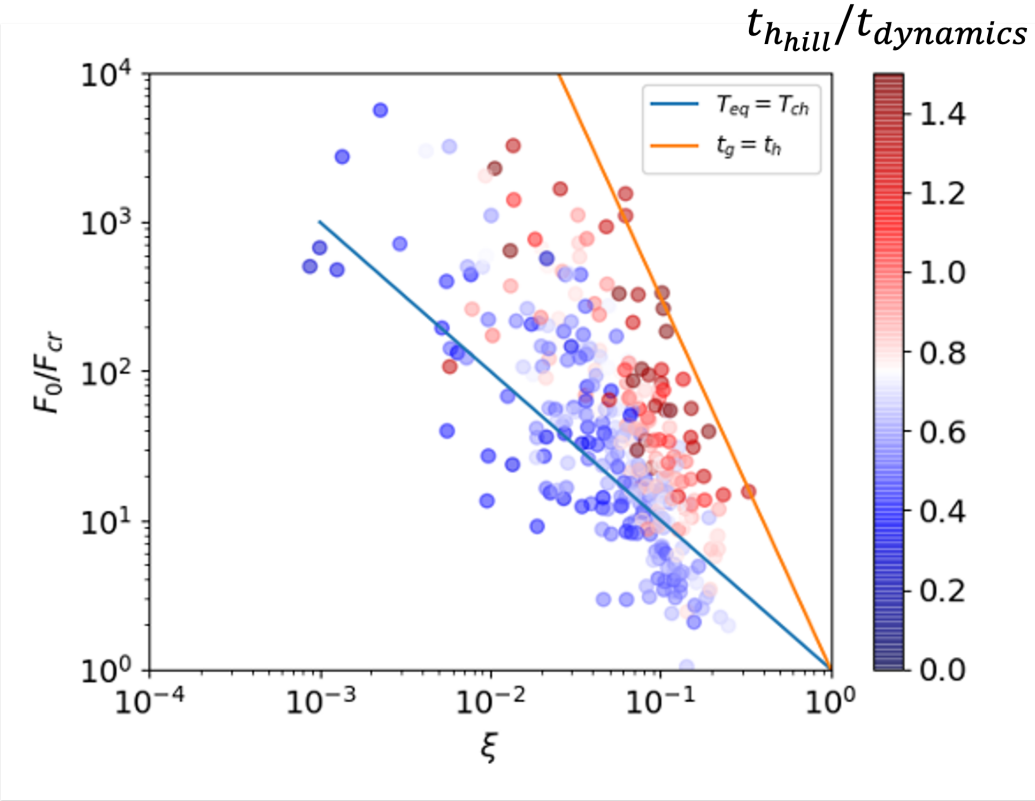

Fig 5.4: The observed planets in $\xi - F_0/F_{cr}$ plane with timescale around hill radius. The color of each points represents the ratio between the timescale of the photoheating and dynamics. In planets represented by red points, the photoheating timescale is shorter than the dynamic timescale.

5.3 Planetary evolution and physical conditions

In this section, we discuss the evolution of hot Jupiters with our mass-loss model based on the physical understandings.

First, we consider the simple planetary evolution without orbital migration. The planetary mass evolution in the early stage can be given as:

$$M(t) = M_{ini} - \int dt\dot{M} \tag{5.24}$$

From this equation, we can find when the system reaches $T_{ch} = T_{eq}$. Figure 5.5 shows

the evolution of the ratio T_{ch}/T_{eq}. We can find that the system reaches the energy-limited ($T_{ch} = T_{eq}$) in about 10Gyr. And the planetary mass evolution is not significant as in the previous study (e.g.Allan and Vidotto 2019). The evolution track in the $\xi - F_0/F_{cr}$ plane should be the vertical straight line because of the small evolution of the mass and radius. In this estimation, we assume the constant average density of the planet and semi-major axis.

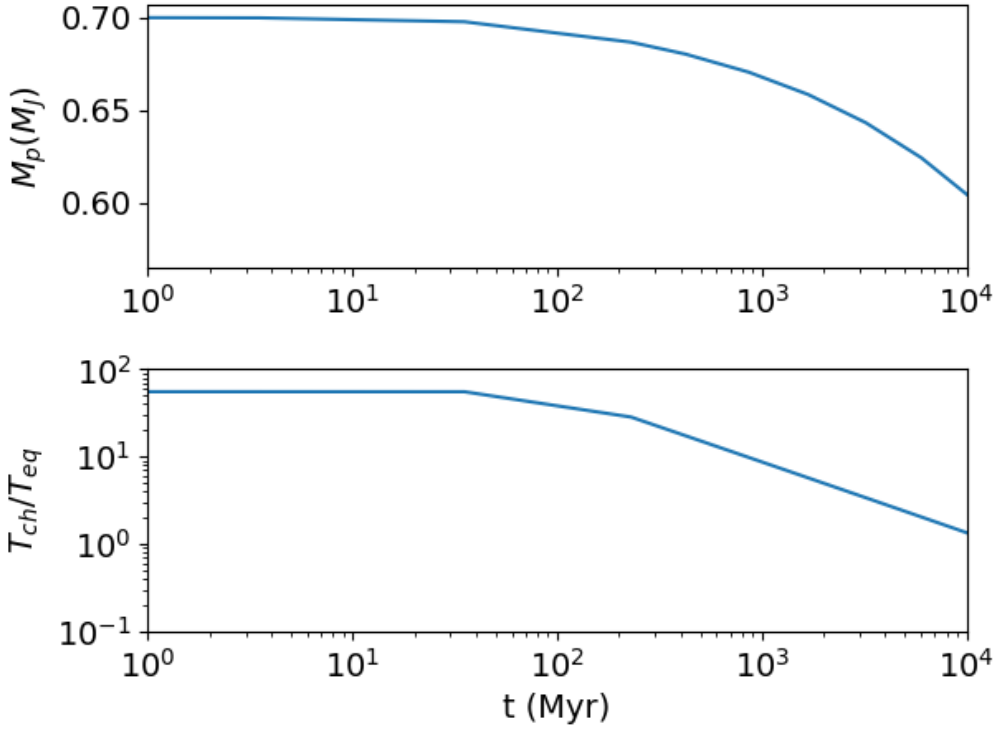

Fig 5.5: Planetary mass evolution (top) and the $T_{\rm ch}/T_{\rm eq}$ evolution (bottom).

We also examine the evolution of planets of different mass. Figure 5.6 shows the evolution track in the $\xi - F_0/F_{cr}$ plane. We find that the evolution track of the light planet also depends on the mass evolution because the mass loss due to the escape is significant for low-mass close-in planets.

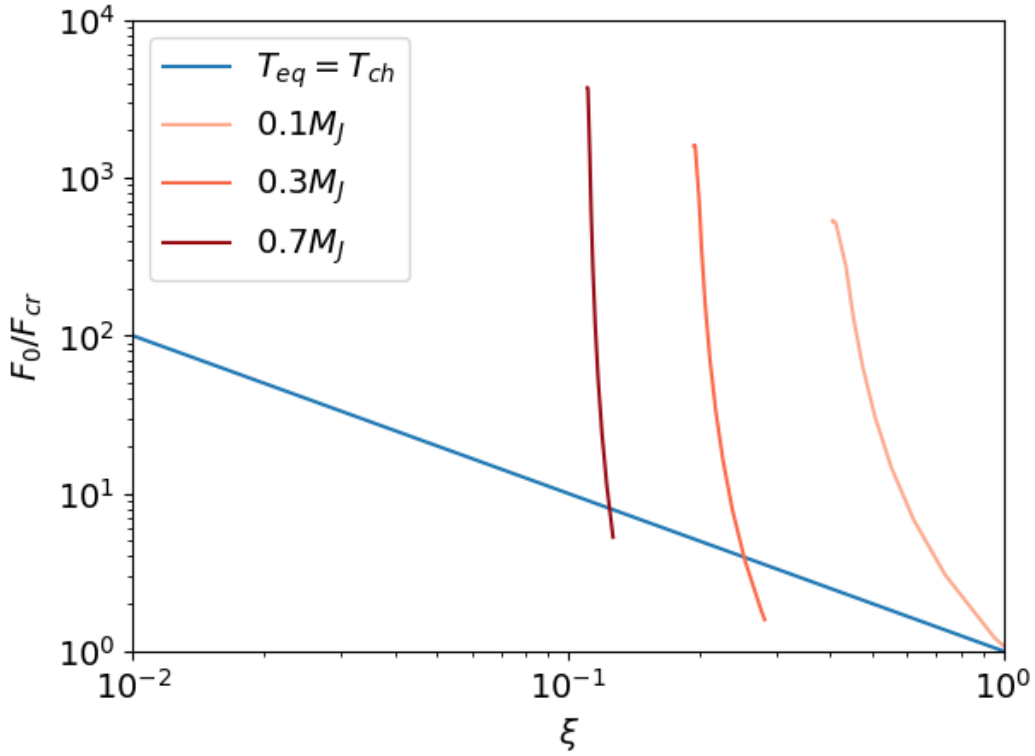

Fig 5.6: Planetary evolution of different mass $M_p = 0.7\,M_J, 0.3\,M_J, 0.1\,M_J$ without the orbital evolution due to the torus in $\xi - F_0/F_{cr}$ plane. The solid blue line shows $T_{\rm ch} = T_{\rm eq}$ condition.

As we briefly explained in Chapter 2, the escaping outflow may accumulate and form a torus around the host star. Tidal interaction between the torus and the planet can cause the migration of the planet as the planet in the protoplanetary disk. The close-in planet may move inward. We calculate the planetary orbital evolution with planetary migration due to the tidal interaction using the open source code (Kurbatov and Bisikalo 2021). We briefly explain the equations which we solve with the code.

The 1D continuity equation and the angular momentum equation can be written as

Pringle 1981; Kurbatov and Bisikalo 2021:

$$\frac{\partial \Sigma}{\partial t} + \frac{1}{r}\frac{\partial (rF)}{\partial r} = -\dot{\Sigma}_{\rm pe} \tag{5.25}$$

$$\frac{\partial}{\partial t}(\Sigma r^2 \Omega) + \frac{1}{r}\frac{\partial (rFr^2\Omega)}{\partial r} = \frac{1}{r}\frac{\partial (r^2 W)}{\partial r} - \dot{\Sigma}_{\rm pe} r^2 \Omega + \Sigma\tau \tag{5.26}$$

where F is the radial mass flux and W is viscosity stress tensor.

The planetary migration can be given as:

$$\frac{da}{dt} = -\frac{4\pi}{M_p}\left(\frac{a}{GM_s}\right)^{1/2}\int_{r_0}^{\infty} dr r\Sigma\tau \tag{5.27}$$

To solve the above equations numerically, we normalize the equations by the characteristic quantities:

$$t_0 = \frac{1}{\Omega_0}, \Sigma_0 = \frac{\dot{M}_p}{2\pi r_0^2 \Omega_0} \tag{5.28}$$

$$\nu_0 = r_0^2\Omega_0, \Omega_0 = \Omega(r) \tag{5.29}$$

where r_0 is the inner boundary of the disk. After the normalization, the disk equation and the migration rate are given as:

$$\frac{\partial \sigma}{\partial s} + \frac{1}{x}\frac{(xf)}{\partial x} = -\frac{t_0}{\Sigma_0}\left(\dot{\Sigma}_{\rm pe} + \frac{d\Sigma_0}{dt}\sigma\right) \tag{5.30}$$

$$f = -\frac{3}{x^{1/2}}\frac{\partial}{\partial x}\left(x^{1/2} n\sigma\right) + \xi^{1/2} x^{1/2}\omega\sigma \tag{5.31}$$

$$n = \alpha h^2 x^{\beta} \tag{5.32}$$

$$\omega = \frac{2C_0}{\pi}\left(\frac{M_p}{M_s}\right)^2 \frac{\xi^{1/2}}{(x-\xi)^2}\frac{x^{3/2}-\xi^{3/2}}{(x^{1/2}-\xi^{1/2})^3} \tag{5.33}$$

$$\frac{da}{ds} = -a\frac{t_0\dot{M}_p}{M_p}\int_1^{\infty} dx\, x\omega\sigma \tag{5.34}$$

These equations are written in dimensionless quantities: $s = t/t_0, x = r/r_0, \sigma = \Sigma/\Sigma_0, f = F/F_0, n = \nu/\nu_0, \xi = a/r_0, h = H_0/r_0$. The parameters α, β are related to the viscosity. From the observations of the protoplanetary disk $\alpha < 3 \times 10^{-3}$ (Flaherty et al. 2017), but the values for the torus due to the accumulation of the gas from the close-in planets are unknown. We run simulations with various parameters. In general, the large value of parameters increase the viscosity and the migration timescale becomes shorter.

As in the case of the atmospheric escape of hot Jupiters, the gas of protoplanetary disks is heated by UV from the host star and escapes. Some theoretical simulations calculated

the photoevaporation rate of the protoplanetary disk with an inner hole (Owen and Jackson 2012). The geometry is close to the case of the torus around the star. The mass-loss rate of torus is given as:

$$\dot{M}_t = 4.8 \times 10^{-9} \left(\frac{M_*}{M_\odot}\right)^{-0.148} \left(\frac{L_X}{10^{30}\,\mathrm{erg/s}}\right)^{1.14} M_\odot\,/\mathrm{yr} \tag{5.35}$$

where L_X is the X-ray luminosity. The X-ray luminosity also changes with the stellar age like the EUV luminosity. We also use the mass-loss profile in Owen and Jackson 2012 to get the photoevaporation rate $\Sigma_{\rm pe}$. The rate profile is given as:

$$\dot{\Sigma} \propto \frac{1}{r}(ab\exp(by) + cd\exp(dy) + ef\exp(fy)) \tag{5.36}$$

$$y = 0.95\left(\frac{M_*}{M_\odot}\right)^{-1} \frac{r - r_0}{1\,\mathrm{AU}},\quad r > r_0 \tag{5.37}$$

where $a = -0.438226, b = -0.10658387, c = 0.5699464, d = 0.010732277, e = -0.131809597$, $f = -1.32285709$ are the fitting parameter in Owen and Jackson 2012.

Previous simulations have shown that the photoevaporation of the torus reduces the surface density and the migration rate can also reduce. The migration timescale without the photoevaporation is about 10^{7-8} year and 10^9 year with photoevaporation. As we introduced in Chapter 2, many previous studies of planetary evolution have assumed the energy-limited mass loss. In reality, this is not true for some close-in planets around young stars and the many of observed hot Jupiters have young host stars. Thus, we should consider the recombination-limited mass loss for the evolution of hot Jupiters. In this calculation, we can neglect the stellar gravity effect on the mass loss because the effect changes the mass-loss rate by a factor of 2.

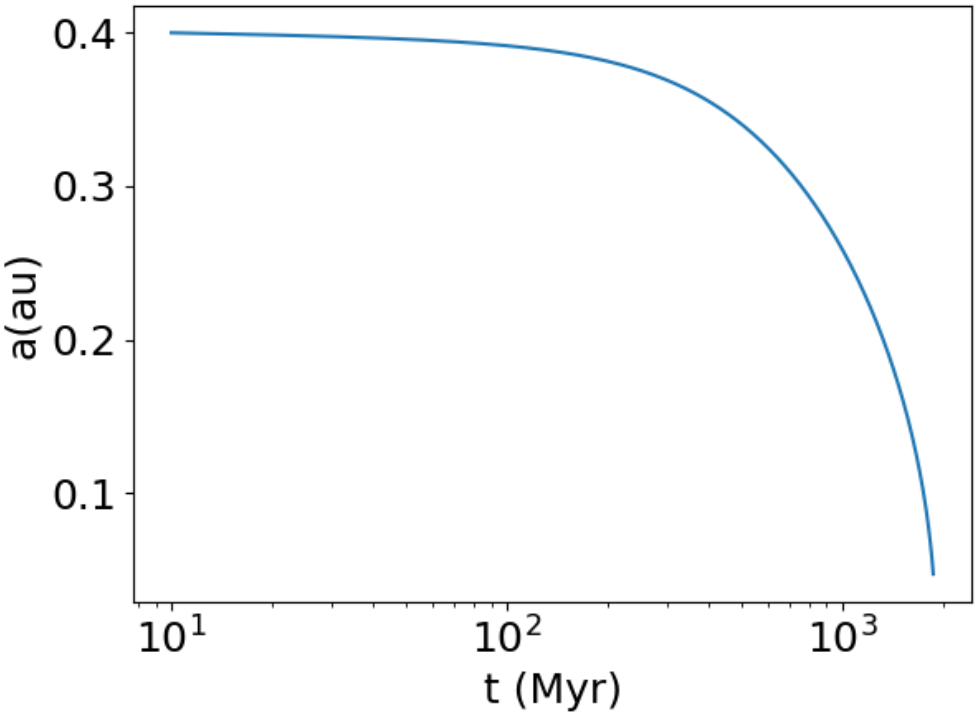

Fig 5.7: Orbital evolution of the fiducial planet ($a_{ini} = 0.4$au, $\alpha = 0.01, \beta = 1.5$).

Figure 5.7 shows the orbital evolution of the fiducial planet. The planet moves inward and the semi-major axis becomes ~ 0.05 AU within a few Gyr.

T_{ch}/T_{eq} is almost constant unless the age reaches $t_{sat} = 10^8$ yr. Then the ratio becomes smaller to some extent. When the orbital migration becomes significant, the ratio becomes larger. This transition may occur when the orbital migration speed is larger than the EUV luminosity evolution speed:

$$\left(\frac{\dot{a}}{a}\right)^2 > \frac{\dot{L}_{EUV}}{L_{EUV}} \tag{5.38}$$

We calculate the evolution of the T_{ch}/T_{eq} for various viscous parameters. We find that the low viscous parameters lead to the low T_{ch}/T_{eq} value (Figure 5.8). We also investigate the dependence of the initial semi-major axis (Figure 5.9). In the case of the small initial semi-major axis, the transition occurs rapidly because of the rapid orbital migration.

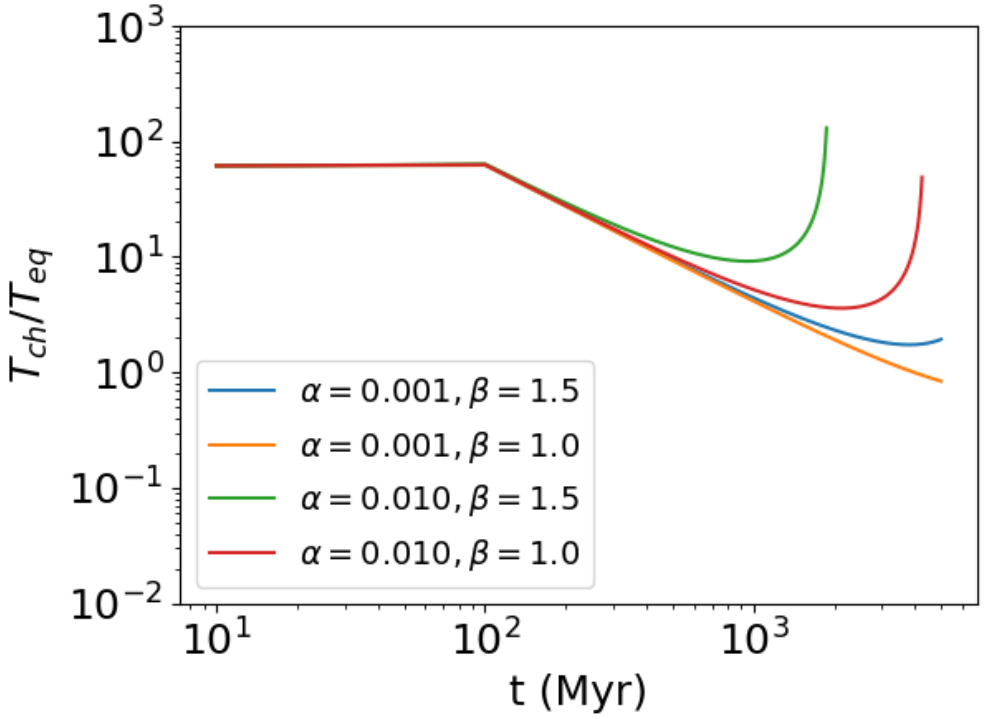

Fig 5.8: T_{ch}/T_{eq} evolution for various viscous parameters $\alpha = 0.01, 0.001, \beta = 1.5, 1.0$.

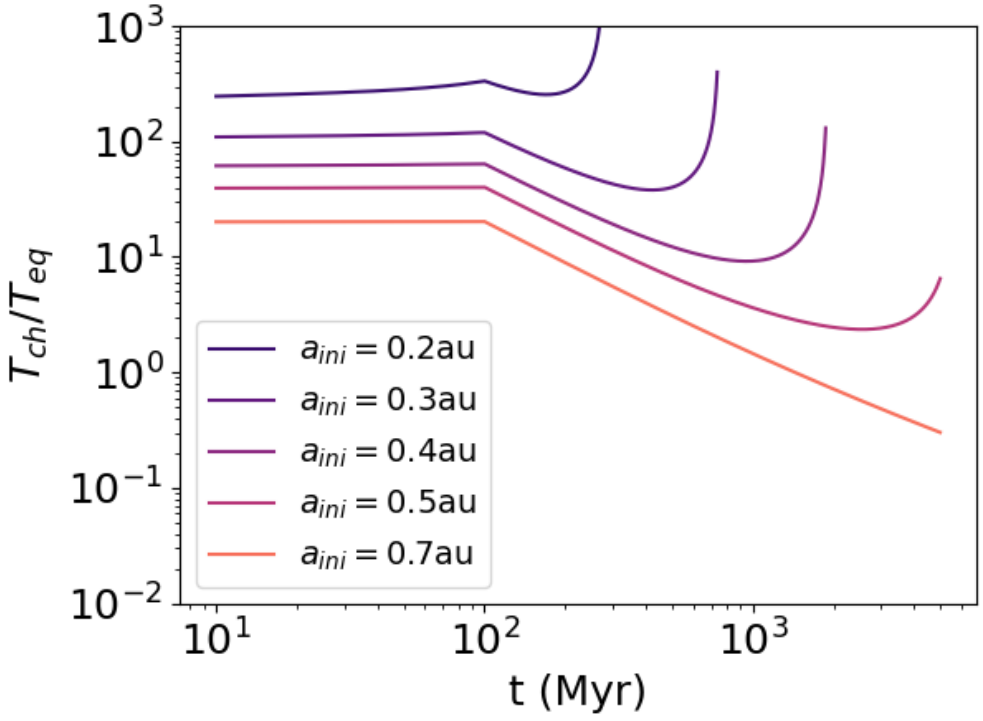

Fig 5.9: T_{ch}/T_{eq} evolution for various initial semi-major axis.

5.4 Summary

Although there are many theoretical studies of atmospheric escape, the physics governing the mass loss of the atmosphere even in the case of the simple hydrogen-dominant atmosphere is unknown. The physics of the atmospheric escape is determined by gravity, photoheating, and gas expansion. We introduce the relevant temperatures and timescales in the upper atmosphere of close-in planets. We find that the equilibrium temperature and the characteristic temperature determine whether the radiative cooling exceeds the cooling due to the expansion of the atmosphere. Thus the temperatures can be used to determine whether the mass-loss rates of the planets are in the energy-limited regime or the recombination-limited regime. The gravitational and photoheating timescales can also be used to determine whether planetary gravity can retain the atmosphere against the

overflow of the upper atmosphere.

We classify the observed exoplanets using the relevant temperatures and timescales. We find that the planets with hydrogen atom detection receive more intense radiation than the critical flux determined by the planetary mass. The EUV flux of two of the Lyman-α non-detection planets is less than the critical flux. For these planets, moderate radiation cannot drive strong outflow. K2-25 b may receive intense EUV although the recent observation has not detected Lyman-α absorption. In this planetary system, unknown factors (e.g. wind confinement) may reduce the transit depth.

We also investigate the planetary evolution with our physical understanding. The EUV luminosity evolution dominates the planetary evolution in typical hot Jupiters. The transition between the recombination-limited and the energy-limited regime may occur in a few Gyr. The orbital evolution can also have a significant effect on the evolution. We find that orbital evolution makes planets more likely to become recombination-limited.

Our physically-motivated conditions provide a general understanding of the atmospheric escape driven by EUV radiation and can be calculated without radiation hydrodynamics simulations. We can use these conditions to select planetary systems suitable for observing atmospheric escape and the wind effect.

Chapter 6

Summary and conclusion

Approximately 5000 exoplanets have been found since the first exoplanet around a solar-like star was found. Hot Jupiters are gas giant planets with short orbital periods. It is crucial to comprehend their formation and evolution processes to understand the diversity of the discovered exoplanets. Intense radiation from the host star heats the upper atmosphere of hot Jupiters and drives the hydrodynamic escape. The mechanism of atmospheric escape is crucial for understanding the evolution of close-in exoplanets.

Most of the previous studies have considered EUV photoionization heating as a dominant heating process in the upper atmosphere and have not considered FUV heating processes. FUV photons from host stars can influence the heating rate in the upper atmosphere, especially around hot stars. The FUV luminosity of hot stars is more than ten thousand times larger than the solar value. We first performed the radiation hydrodynamics simulations with FUV heating processes in Chapter 3. There are three possible FUV heating processes. The first one is photoelectric heating through dust grains. This process is a popular process in the context of ISM. We find that the FUV photoelectric heating can drive the atmospheric escape in hot Jupiters around hot stars. The existence of dust grains in the upper atmosphere is required for the FUV photoelectric heating process. We show that the photoelectric heating process can drive the escaping outflow if the dust-to-gas mass ratio is sufficiently large ($D/G > 10^{-5}$). The second process is the photon pumping of molecular hydrogen. In this process, FUV photons excite the hydrogen molecules in the atmosphere and the collisional de-excitation and photodissociation contribute to the heating rate. The last process is Balmer absorption. The FUV photons photoionize hydrogen atoms at the excited level with principal quantum number $n = 2$. The last two processes are independent of the existence of dust grains. We find that these processes can

also drive the atmospheric escape around hot stars. The heating rate of Balmer absorption is larger than that of the pumping process in the case of very hot host stars. In the case of intermediate mass stars, the heating due to the pumping process becomes comparable to the heating due to Balmer absorption. We find that these FUV heating processes are dominant in the case of hot stars, and that the classical EUV photoionization determines the atmospheric escape around relatively cool stars like solar-type stars. The results of our simulations are consistent with the pervious theoretical simulations and observations of hot Jupiters around solar-type stars at this point. Our results suggest that close-in planets around hot stars experience different evolution due to the intense mass-loss driven by FUV heating.

The geometry of the escaping outflow determines the spectroscopic feature of Lyman-α absorption which has been used in the classical observations of the atmospheric escape of hot Jupiters. The stellar wind interacts with the escaping outflow and changes the outflow structure. Multi-dimensional radiation hydrodynamics simulations can reveal the atmospheric structure and can be used to interpret the observational absorption signals. The structure of the outflow has not been investigated by the detailed radiation hydrodynamics simulations in a self-consistent manner. In Chapter 4, we focus on our radiation hydrodynamics simulations with stellar winds from host stars. We implement the effect of the stellar wind in our simulations. We perform the simulations by resolving the atmospheric structure from the place where the outflow is launched by the EUV photoionization to the point where the wind interacts with the launched outflow. We find that the strong stellar wind can confine the outflow and the Lyman-α absorption is reduced because the effective absorption radius becomes smaller. The strong wind ($\dot{M}_* > 100\dot{M}_\odot$) can significantly reduce the Lyman-α absorption. We also investigate other possible absorption signals that can be observed by the ground-base telescopes. We find that Hα absorption depth is almost independent of the stellar wind strength because the lower dense layer of the atmosphere contributes to the transit depth. The difference in the stellar wind strength dependence between Lyman-α and Hα absorption can be used to investigate the EUV flux and the stellar wind parameters. We find that the mass-loss rate of the planet is almost independent of the stellar wind strength because the wind cannot confine the outflow to the launching point unless the wind is extremely strong ($\dot{M}_* > 1000\dot{M}_\odot$).

The physical understanding of the atmospheric structure can be helpful to understand the mass-loss rate of the hot Jupiters and the planetary evolution. Photoheating, gravity, and gas expansion determine the physics of the atmospheric escape. We introduce the gravitational, equilibrium, and characteristic temperatures in Chapter 5. The gravi-

tational temperature $T_{\rm g}$ represents the strength of the planetary gravity. The equilibrium temperature $T_{\rm eq}$ is determined by the balance between the photoheating and the radiative cooling and becomes $\sim 10^4\,{\rm K}$ in the case of the EUV photoionization heating of hydrogen atom. The gas temperature cannot exceed the equilibrium temperature. The characteristic temperature $T_{\rm ch}$ represents the temperature which the gas can reach within the dynamical timescale if we consider only the photoheating. The characteristic temperature can exceed the equilibrium temperature although the real temperature cannot reach. The ratio $T_{\rm ch}/T_{\rm eq}$ can be written by the ratio of the planetary radius to the gravitational radius and the ratio of the EUV flux to the critical flux which can be determined by the planetary mass ($\xi, F_0/F_{cr}$). We find that the ratio $T_{\rm ch}/T_{\rm eq}$ determines whether the system becomes recombination-limited or energy-limited from the results of radiation hydrodynamics simulations. If the ratio is larger than the unity $T_{\rm ch}/T_{\rm eq} > 1$, the recombination cooling exceeds the cooling due to the gas expansion and the mass-loss rate is recombination limited. We also find that many close-in planets with hydrogen atom detection is exposed to stronger radiation EUV radiation than the critical flux. The EUV flux of the two of the close-in planets without Lyman-α absorption is less than the critical value and the mass loss may be weak. K2-25 b may be an exception. The planet does not show the Lyman-α absorption but is exposed to stronger EUV radiation than the critical value. This means that the unknown factor like the stellar wind confinement reduces the transit signature. Typical hot Jupiters reach the energy-limited regime in a few Gyr.

From our results of the predicted transit signals and future observations, we can estimate the EUV flux and the stellar wind parameters which are difficult to determine by other methods. The estimated parameters are essential for understanding environments of close-in exoplanets. Our radiation hydrodynamics codes can be used for not only for hot Jupiters but also for close-in super earths which are planned to observe by future advanced telescopes. We can easily determine suitable exoplanets to observe the atmospheric escape from our physical understandings and classification of the atmospheric escape of close-in planets. Our classification based on the physical understanding of photoheating can be extended to other planets with other photoheating and radiative cooling processes, such as observed water-rich exoplanets (e.g. TRAPPIST-1 system). The loss of water is directly related to the habitable worlds outside of our solar system because the existence of water is necessary for life. Our study also provides important insights into the atmospheric structure of terrestrial planets in the habitable zone and the possibility of life on their surfaces, which are planned to be observed by telescopes such as JWST in the near future. Research on exoplanets is steadily approaching answers to important questions such as the origin

of life and whether human-like life exists on other planets. From this perspective, our research has clarified a variety of atmospheric environments and developed a new theory for the general atmosphere.

Appendix A

Appendix: Hydrodynamic Equations in Various Geometry

Hydrodynamic equations are solved in hydrodynamic simulations. 3D cartesian, 1D spherical, and 2D cylindrical equations are usually used in astrophysics. We introduce these hydrodynamic equations in this appendix. The general forms of the hydrodynamic equations are derived from the mass conservation, the momentum conservation, and the energy conservation. From the mass conservation, we have:

$$\frac{\partial \rho}{\partial t} + \nabla \cdot (\rho \boldsymbol{v}) = 0 \tag{A.1}$$

This equation is also called as a continuity equation. From the momentum conservation, we have:

$$\frac{\partial (\rho \boldsymbol{v})}{\partial t} + \nabla \cdot (\rho \boldsymbol{v}\boldsymbol{v}) + \nabla p = 0 \tag{A.2}$$

where p is the gas pressure. From the energy conservation, we have:

$$\frac{\partial (\rho (e + \frac{1}{2} v^2))}{\partial t} + \nabla \cdot \left[(\rho e + \frac{1}{2} \rho v^2 + p) \boldsymbol{v} \right] = 0 \tag{A.3}$$

where e is the internal specific energy.

A.1 3D Cartesian case

The hydrodynamic equations in 3D Cartesian coordinates (x, y, z) can be gine as:

$$\frac{\partial \rho}{\partial t} + \frac{\partial(\rho v_x)}{\partial x} + \frac{\partial(\rho v_y)}{\partial y} + \frac{\partial(\rho v_z)}{\partial z} = 0 \tag{A.4}$$

$$\frac{\partial(\rho v_x)}{\partial t} + \frac{\partial(\rho v_x v_x)}{\partial x} + \frac{\partial(\rho v_x v_y)}{\partial y} + \frac{\partial(\rho v_x v_z)}{\partial z} + \frac{\partial p}{\partial x} = -\rho \frac{\partial \Phi}{\partial x} \tag{A.5}$$

$$\frac{\partial(\rho v_y)}{\partial t} + \frac{\partial(\rho v_y v_x)}{\partial x} + \frac{\partial(\rho v_y v_y)}{\partial y} + \frac{\partial(\rho v_y v_z)}{\partial z} + \frac{\partial p}{\partial y} = -\rho \frac{\partial \Phi}{\partial y} \tag{A.6}$$

$$\frac{\partial(\rho v_z)}{\partial t} + \frac{\partial(\rho v_z v_x)}{\partial x} + \frac{\partial(\rho v_z v_y)}{\partial y} + \frac{\partial(\rho v_z v_z)}{\partial z} + \frac{\partial p}{\partial z} = -\rho \frac{\partial \Phi}{\partial z} \tag{A.7}$$

$$\frac{\partial E}{\partial t} + \frac{\partial(H v_x)}{\partial x} + \frac{\partial(H v_y)}{\partial y} + \frac{\partial(H v_z)}{\partial z} = \rho(\Gamma - \Lambda) \tag{A.8}$$

where E, H are the total energy and enthalpy per unit volume:

$$E = \frac{1}{2}\rho v^2 + \frac{\rho k T}{\mu m_{\rm H}(\gamma - 1)} \tag{A.9}$$

$$H = E + p \tag{A.10}$$

A.2 1D Spherical case

In the case of spherical coordinates (r, θ, ϕ), the equations have different forms. If we assume spherical symmetry, the divergence can be written as:

$$\nabla \cdot \boldsymbol{F} = \frac{1}{r^2}\frac{\partial(r^2 F_r)}{\partial r} \tag{A.11}$$

We can write the hydrodynamic equations as:

$$\frac{\partial \rho}{\partial t} + \frac{1}{r^2}\frac{\partial(\rho r^2 v_r)}{\partial r} = 0 \tag{A.12}$$

$$\frac{\partial(\rho v_r)}{\partial t} + \frac{1}{r^2}\frac{\partial(\rho r^2 v_r v_r)}{\partial r} + \frac{\partial p}{\partial r} = -\rho \frac{\partial \Phi}{\partial r} \tag{A.13}$$

$$\frac{\partial E}{\partial t} + \frac{1}{r^2}\frac{\partial(H r^2 v_r)}{\partial r} = \rho(\Gamma - \Lambda) \tag{A.14}$$

A.3 2D Cylindrical case

In the case of cylindrical coordinates (R, ϕ, z), the divergence can be given as:

$$\nabla \cdot \boldsymbol{F} = \frac{1}{R}\frac{\partial(R F_R)}{\partial R} + \frac{1}{R}\frac{\partial F_\phi}{\partial \phi} + \frac{\partial F_z}{\partial z} \tag{A.15}$$

If we assume cylindrical symmetry, the hydrodynamic equations are given as:

$$\frac{\partial \rho}{\partial t} + \frac{1}{R}\frac{\partial(\rho R v_R)}{\partial R} + \frac{\partial(\rho v_z)}{\partial z} = 0 \tag{A.16}$$

$$\frac{\partial(\rho v_R)}{\partial t} + \frac{1}{R}\frac{\partial(\rho R v_R v_R)}{\partial R} + \frac{\partial(\rho v_R v_z)}{\partial z} + \frac{\partial p}{\partial R} = -\rho\frac{\partial \Phi}{\partial R} \tag{A.17}$$

$$\frac{\partial(\rho v_z)}{\partial t} + \frac{1}{R}\frac{\partial(\rho R v_z v_R)}{\partial R} + \frac{\partial(\rho v_z v_z)}{\partial z} + \frac{\partial p}{\partial z} = -\rho\frac{\partial \Phi}{\partial z} \tag{A.18}$$

$$\frac{\partial E}{\partial t} + \frac{1}{R}\frac{\partial(H R v_R)}{\partial R} + \frac{\partial(H v_z)}{\partial z} = \rho(\Gamma - \Lambda) \tag{A.19}$$

We solve the above equations in our 2D simulations.

Acknowledgement

First of all, I would like to thank my advisor, Professor Naoki Yoshida. He supervised me for about seven years from my undergraduate classes to the completion of my Ph.D. course. His undergraduate lectures about the stellar evolution inspired me to study astrophysics and the knowledge from the lecture is also used in this study. He taught me everything I needed to know to pursue my research, from basic knowledge of astrophysics to how to write a paper. I have no doubt that what he has taught me will be useful in many aspects of my life in the future.

I thank Riouhei Nakatani for providing the basic code of the radiation hydrodynamic simulation. He also taught me about basics of the simulation knowledge and how to construct the code. Discussions with him have helped me to advance many parts of my research.

I thank the committee members of this dissertation, Fujihiro Hamba, Takao Nakagawa, Masami Ouchi, Noriko Yamasaki, and Hideyuki Tagoshi, for their fruitful comments and discussions. I also thank all the members of the University of Tokyo Theoretical Astrophysical Group and Research Center for the Early Universe for many fruitful discussions. Discussions in this group led to many discoveries. I could proceed my research in the comfortable environment in this group although the situation around academia was difficult due to the pandemic. I was happy to work with this group.

I would also like to thank my family, Hiroshi, Hiroko, and Kento. Without their support in my daily life and mental support, I would not have been able to continue my research in the Ph. D. course. Their support will be important also in my future academic life.

I have been supported by International Graduate Program for Excellence in Earth-Space Science (IGPEES) of the University of Tokyo and JSPS KAKENHI Grant number 21J11207. Through IGPEES program, I was able to discuss with many researchers of my generation and it encouraged me to proceed my research. The sub-supervisor of IGPEES, Professor Yuri Aikawa, gave many insightful comments on my research and provided me

with another perspective. The numerical computations in the multi-dimensional radiation hydrodynamic simulations of Chapter 3 and Chapter 4 were carried out on Cray XC50 at Center for Computational Astrophysics, National Astronomical Observatory of Japan.

Reference

Fred C. Adams. Magnetically Controlled Outflows from Hot Jupiters. ApJ, 730(1):27, March 2011. doi: 10.1088/0004-637X/730/1/27.

Vardan Adibekyan. Heavy Metal Rules. I. Exoplanet Incidence and Metallicity. *Geosciences*, 9(3):105, February 2019. doi: 10.3390/geosciences9030105.

A. Allan and A. A. Vidotto. Evolution of atmospheric escape in close-in giant planets and their associated Ly α and H α transit predictions. MNRAS, 490(3):3760–3771, December 2019. doi: 10.1093/mnras/stz2842.

F. J. Alonso-Floriano, I. A. G. Snellen, S. Czesla, F. F. Bauer, M. Salz, M. Lampón, L. M. Lara, E. Nagel, M. López-Puertas, L. Nortmann, A. Sánchez-López, J. Sanz-Forcada, J. A. Caballero, A. Reiners, I. Ribas, A. Quirrenbach, P. J. Amado, J. Aceituno, G. Anglada-Escudé, V. J. S. Béjar, M. Brinkmöller, A. P. Hatzes, Th. Henning, A. Kaminski, M. Kürster, F. Labarga, D. Montes, E. Pallé, J. H. M. M. Schmitt, and M. R. Zapatero Osorio. He I λ 10 830 Å in the transmission spectrum of HD209458 b. A&A, 629:A110, September 2019. doi: 10.1051/0004-6361/20193597910.48550/arXiv.1907.13425.

Peter Anninos, Yu Zhang, Tom Abel, and Michael L. Norman. Cosmological hydrodynamics with multi-species chemistry and nonequilibrium ionization and cooling. New A, 2 (3):209–224, Aug 1997. doi: 10.1016/S1384-1076(97)00009-2.

Martin Asplund, Nicolas Grevesse, A. Jacques Sauval, and Pat Scott. The Chemical Composition of the Sun. ARA&A, 47(1):481–522, September 2009. doi: 10.1146/annurev.astro.46.060407.145222.

T. Azevedo Silva, O. D. S. Demangeon, N. C. Santos, R. Allart, F. Borsa, E. Cristo, E. Esparza-Borges, J. V. Seidel, E. Palle, S. G. Sousa, H. M. Tabernero, M. R. Zapatero

Osorio, S. Cristiani, F. Pepe, R. Rebolo, V. Adibekyan, Y. Alibert, S. C. C. Barros, F. Bouchy, V. Bourrier, G. Lo Curto, P. Di Marcantonio, V. D'Odorico, D. Ehrenreich, P. Figueira, J. I. González Hernández, C. Lovis, C. J. A. P. Martins, A. Mehner, G. Micela, P. Molaro, D. Mounzer, N. J. Nunes, A. Sozzetti, A. Suárez Mascareño, and S. Udry. Detection of barium in the atmospheres of the ultra-hot gas giants WASP-76b and WASP-121b. Together with new detections of Co and Sr+ on WASP-121b. A&A, 666:L10, October 2022. doi: 10.1051/0004-6361/202244489.

M. J. Baines, I. P. Williams, and A. S. Asebiomo. Resistance to the motion of a small sphere moving through a gas. MNRAS, 130:63, January 1965. doi: 10.1093/mnras/130.1.63.

E. L. O. Bakes and A. G. G. M. Tielens. The Photoelectric Heating Mechanism for Very Small Graphitic Grains and Polycyclic Aromatic Hydrocarbons. ApJ, 427:822, Jun 1994. doi: 10.1086/174188.

Alexei Baskin and Ari Laor. Dust inflated accretion disc as the origin of the broad line region in active galactic nuclei. MNRAS, 474(2):1970–1994, February 2018. doi: 10.1093/mnras/stx2850.

M. C. Begelman, C. F. McKee, and G. A. Shields. Compton heated winds and coronae above accretion disks. I. Dynamics. ApJ, 271:70–88, August 1983. doi: 10.1086/161178.

Lotfi Ben-Jaffel and S. Sona Hosseini. On the Existence of Energetic Atoms in the Upper Atmosphere of Exoplanet HD209458b. ApJ, 709(2):1284–1296, February 2010. doi: 10.1088/0004-637X/709/2/1284.

A. Beth, P. Garnier, D. Toublanc, I. Dandouras, and C. Mazelle. Theory for planetary exospheres: I. Radiation pressure effect on dynamical trajectories. Icarus, 266:410–422, March 2016. doi: 10.1016/j.icarus.2015.10.018.

William J. Borucki, David G. Koch, Gibor Basri, Natalie Batalha, Timothy M. Brown, Stephen T. Bryson, Douglas Caldwell, Jørgen Christensen-Dalsgaard, William D. Cochran, Edna DeVore, Edward W. Dunham, III Gautier, Thomas N., John C. Geary, Ronald Gilliland, Alan Gould, Steve B. Howell, Jon M. Jenkins, David W. Latham, Jack J. Lissauer, Geoffrey W. Marcy, Jason Rowe, Dimitar Sasselov, Alan Boss, David Charbonneau, David Ciardi, Laurance Doyle, Andrea K. Dupree, Eric B. Ford, Jonathan Fortney, Matthew J. Holman, Sara Seager, Jason H. Steffen, Jill Tarter, William F. Welsh, Christopher Allen, Lars A. Buchhave, Jessie L. Christiansen, Bruce D. Clarke,

Santanu Das, Jean-Michel Désert, Michael Endl, Daniel Fabrycky, Francois Fressin, Michael Haas, Elliott Horch, Andrew Howard, Howard Isaacson, Hans Kjeldsen, Jeffery Kolodziejczak, Craig Kulesa, Jie Li, Philip W. Lucas, Pavel Machalek, Donald McCarthy, Phillip MacQueen, Søren Meibom, Thibaut Miquel, Andrej Prsa, Samuel N. Quinn, Elisa V. Quintana, Darin Ragozzine, William Sherry, Avi Shporer, Peter Tenenbaum, Guillermo Torres, Joseph D. Twicken, Jeffrey Van Cleve, Lucianne Walkowicz, Fred C. Witteborn, and Martin Still. Characteristics of Planetary Candidates Observed by Kepler. II. Analysis of the First Four Months of Data. ApJ, 736(1):19, July 2011. doi: 10.1088/0004-637X/736/1/19.

V. Bourrier and A. Lecavelier des Etangs. 3D model of hydrogen atmospheric escape from HD 209458b and HD 189733b: radiative blow-out and stellar wind interactions. A&A, 557:A124, Sep 2013. doi: 10.1051/0004-6361/201321551.

V. Bourrier, A. Lecavelier des Etangs, D. Ehrenreich, Y. A. Tanaka, and A. A. Vidotto. An evaporating planet in the wind: stellar wind interactions with the radiatively braked exosphere of GJ 436 b. A&A, 591:A121, June 2016. doi: 10.1051/0004-6361/201628362.

Robert L. Brown. On the Photoionization of Hydrogen and Helium. ApJ, 164:387, March 1971. doi: 10.1086/150851.

Samuel H. C. Cabot, Nikku Madhusudhan, Luis Welbanks, Anjali Piette, and Siddharth Gandhi. Detection of neutral atomic species in the ultra-hot Jupiter WASP-121b. MNRAS, 494(1):363–377, May 2020. doi: 10.1093/mnras/staa74810.48550/arXiv.2001.07196.

S. Carolan, A. A. Vidotto, P. Plavchan, C. Villarreal D'Angelo, and G. Hazra. The dichotomy of atmospheric escape in AU Mic b. MNRAS, 498(1):L53–L57, November 2020. doi: 10.1093/mnrasl/slaa127.

S. Carolan, A. A. Vidotto, G. Hazra, C. Villarreal D'Angelo, and D. Kubyshkina. The effects of magnetic fields on observational signatures of atmospheric escape in exoplanets: Double tail structures. MNRAS, 508(4):6001–6012, December 2021a. doi: 10.1093/mnras/stab2947.

S. Carolan, A. A. Vidotto, C. Villarreal D'Angelo, and G. Hazra. Effects of the stellar wind on the Ly α transit of close-in planets. MNRAS, 500(3):3382–3393, January 2021b. doi: 10.1093/mnras/staa3431.

N. Casasayas-Barris, E. Pallé, F. Yan, G. Chen, S. Albrecht, L. Nortmann, V. Van Eylen, I. Snellen, G. J. J. Talens, J. I. González Hernández, R. Rebolo, and G. P. P. L. Otten. Na I and Hα absorption features in the atmosphere of MASCARA-2b/KELT-20b. A&A, 616:A151, Sep 2018. doi: 10.1051/0004-6361/201832963.

T. Castellano, J. Jenkins, D. E. Trilling, L. Doyle, and D. Koch. Detection of Planetary Transits of the Star HD 209458 in the Hipparcos Data Set. ApJ, 532(1):L51–L53, March 2000. doi: 10.1086/312565.

David C. Catling and Kevin J. Zahnle. The Planetary Air Leak. *Scientific American*, 300 (5):36–43, May 2009. doi: 10.1038/scientificamerican0509-36.

P. Wilson Cauley, Seth Redfield, and Adam G. Jensen. A Decade of Hα Transits for HD 189733 b: Stellar Activity versus Absorption in the Extended Atmosphere. AJ, 153(5): 217, May 2017. doi: 10.3847/1538-3881/aa6a15.

P. Wilson Cauley, Evgenya L. Shkolnik, Joe Llama, and Antonino F. Lanza. Magnetic field strengths of hot Jupiters from signals of star-planet interactions. *Nature Astronomy*, 3: 1128–1134, July 2019. doi: 10.1038/s41550-019-0840-x.

David Charbonneau, Timothy M. Brown, David W. Latham, and Michel Mayor. Detection of Planetary Transits Across a Sun-like Star. ApJ, 529(1):L45–L48, January 2000. doi: 10.1086/312457.

David Charbonneau, Timothy M. Brown, Robert W. Noyes, and Ronald L. Gilliland. Detection of an Extrasolar Planet Atmosphere. ApJ, 568(1):377–384, March 2002. doi: 10.1086/338770.

G. Chen, N. Casasayas-Barris, E. Pallé, F. Yan, M. Stangret, H. M. Cegla, R. Allart, and C. Lovis. Detection of Na, K, and Hα absorption in the atmosphere of WASP-52b using ESPRESSO. A&A, 635:A171, March 2020. doi: 10.1051/0004-6361/20193698610.48550/arXiv.2002.08379.

Duncan Christie, Phil Arras, and Zhi-Yun Li. Hα Absorption in Transiting Exoplanet Atmospheres. ApJ, 772(2):144, August 2013. doi: 10.1088/0004-637X/772/2/144.

Duncan Christie, Phil Arras, and Zhi-Yun Li. Axisymmetric Simulations of Hot Jupiter-Stellar Wind Hydrodynamic Interaction. ApJ, 820(1):3, March 2016. doi: 10.3847/0004-637X/820/1/3.

S. Czesla, M. Lampón, J. Sanz-Forcada, A. García Muñoz, M. López-Puertas, L. Nortmann, D. Yan, E. Nagel, F. Yan, J. H. M. M. Schmitt, J. Aceituno, P. J. Amado, J. A. Caballero, N. Casasayas-Barris, Th. Henning, S. Khalafinejad, K. Molaverdikhani, D. Montes, E. Pallé, A. Reiners, P. C. Schneider, I. Ribas, A. Quirrenbach, M. R. Zapatero Osorio, and M. Zechmeister. Hα and He I absorption in HAT-P-32 b observed with CARMENES. Detection of Roche lobe overflow and mass loss. A&A, 657:A6, January 2022. doi: 10.1051/0004-6361/202039919.

B. T. Draine and Frank Bertoldi. Structure of Stationary Photodissociation Fronts. ApJ, 468:269, Sep 1996. doi: 10.1086/177689.

Bruce T. Draine. *Physics of the Interstellar and Intergalactic Medium*. 2011.

Courtney D. Dressing and David Charbonneau. The Occurrence of Potentially Habitable Planets Orbiting M Dwarfs Estimated from the Full Kepler Dataset and an Empirical Measurement of the Detection Sensitivity. ApJ, 807(1):45, July 2015. doi: 10.1088/0004-637X/807/1/45.

David Ehrenreich, Vincent Bourrier, Peter J. Wheatley, Alain Lecavelier des Etangs, Guillaume Hébrard, Stéphane Udry, Xavier Bonfils, Xavier Delfosse, Jean-Michel Désert, David K. Sing, and Alfred Vidal-Madjar. A giant comet-like cloud of hydrogen escaping the warm Neptune-mass exoplanet GJ 436b. Nature, 522(7557):459–461, Jun 2015. doi: 10.1038/nature14501.

N. V. Erkaev, Yu. N. Kulikov, H. Lammer, F. Selsis, D. Langmayr, G. F. Jaritz, and H. K. Biernat. Roche lobe effects on the atmospheric loss from "Hot Jupiters". A&A, 472(1): 329–334, September 2007. doi: 10.1051/0004-6361:20066929.

A. Esquivel, M. Schneiter, C. Villarreal D'Angelo, M. A. Sgró, and L. Krapp. Hydrodynamical interaction of stellar and planetary winds: effects of charge exchange and radiation pressure on the observed Ly α absorption. MNRAS, 487(4):5788–5798, August 2019. doi: 10.1093/mnras/stz1725.

Adina D. Feinstein, Benjamin T. Montet, Megan Ansdell, Brian Nord, Jacob L. Bean, Maximilian N. Günther, Michael A. Gully-Santiago, and Joshua E. Schlieder. Flare Statistics for Young Stars from a Convolutional Neural Network Analysis of TESS Data. AJ, 160(5):219, November 2020. doi: 10.3847/1538-3881/abac0a.

Kevin M. Flaherty, A. Meredith Hughes, Sanaea C. Rose, Jacob B. Simon, Chunhua Qi, Sean M. Andrews, Ágnes Kóspál, David J. Wilner, Eugene Chiang, Philip J. Armitage, and Xue-ning Bai. A Three-dimensional View of Turbulence: Constraints on Turbulent Motions in the HD 163296 Protoplanetary Disk Using DCO^+. ApJ, 843(2):150, July 2017. doi: 10.3847/1538-4357/aa79f9.

Naho Fujita, Yasunori Hori, and Takanori Sasaki. Orbital Evolution of Close-in Super-Earths Driven by Atmospheric Escape. ApJ, 928(2):105, April 2022. doi: 10.3847/1538-4357/ac558c.

Benjamin J. Fulton, Erik A. Petigura, Andrew W. Howard, Howard Isaacson, Geoffrey W. Marcy, Phillip A. Cargile, Leslie Hebb, Lauren M. Weiss, John Asher Johnson, Timothy D. Morton, Evan Sinukoff, Ian J. M. Crossfield, and Lea A. Hirsch. The California-Kepler Survey. III. A Gap in the Radius Distribution of Small Planets. AJ, 154(3):109, September 2017. doi: 10.3847/1538-3881/aa80eb.

A. García Muñoz. Physical and chemical aeronomy of HD 209458b. Planet. Space Sci., 55 (10):1426–1455, July 2007. doi: 10.1016/j.pss.2007.03.007.

A. García Muñoz and P. C. Schneider. Rapid Escape of Ultra-hot Exoplanet Atmospheres Driven by Hydrogen Balmer Absorption. ApJ, 884(2):L43, Oct 2019. doi: 10.3847/2041-8213/ab498d.

A. García Muñoz, A. Youngblood, L. Fossati, D. Gandolfi, J. Cabrera, and H. Rauer. Is π Men c's Atmosphere Hydrogen-dominated? Insights from a Non-detection of H I Lyα Absorption. ApJ, 888(2):L21, January 2020. doi: 10.3847/2041-8213/ab61ff.

Cecilia Garraffo, Jeremy J. Drake, Ofer Cohen, Julian D. Alvarado-Gómez, and Sofia P. Moschou. The Threatening Magnetic and Plasma Environment of the TRAPPIST-1 Planets. ApJ, 843(2):L33, July 2017. doi: 10.3847/2041-8213/aa79ed.

B. Scott Gaudi, Keivan G. Stassun, Karen A. Collins, Thomas G. Beatty, George Zhou, David W. Latham, Allyson Bieryla, Jason D. Eastman, Robert J. Siverd, Justin R. Crepp, Erica J. Gonzales, Daniel J. Stevens, Lars A. Buchhave, Joshua Pepper, Marshall C. Johnson, Knicole D. Colon, Eric L. N. Jensen, Joseph E. Rodriguez, Valerio Bozza, Sebastiano Calchi Novati, Giuseppe D'Ago, Mary T. Dumont, Tyler Ellis, Clement Gaillard, Hannah Jang-Condell, David H. Kasper, Akihiko Fukui, Joao Gregorio, Ayaka Ito, John F. Kielkopf, Mark Manner, Kyle Matt, Norio Narita, Thomas E.

Oberst, Phillip A. Reed, Gaetano Scarpetta, Denice C. Stephens, Rex R. Yeigh, Roberto Zambelli, B. J. Fulton, Andrew W. Howard, David J. James, Matthew Penny, Daniel Bayliss, Ivan A. Curtis, D. L. Depoy, Gilbert A. Esquerdo, Andrew Gould, Michael D. Joner, Rudolf B. Kuhn, Jonathan Labadie-Bartz, Michael B. Lund, Jennifer L. Marshall, Kim K. McLeod, Richard W. Pogge, Howard Relles, Christopher Stockdale, T. G. Tan, Mark Trueblood, and Patricia Trueblood. A giant planet undergoing extreme-ultraviolet irradiation by its hot massive-star host. Nature, 546(7659):514–518, June 2017. doi: 10.1038/nature22392.

Michaël Gillon, Amaury H. M. J. Triaud, Brice-Olivier Demory, Emmanuël Jehin, Eric Agol, Katherine M. Deck, Susan M. Lederer, Julien de Wit, Artem Burdanov, James G. Ingalls, Emeline Bolmont, Jeremy Leconte, Sean N. Raymond, Franck Selsis, Martin Turbet, Khalid Barkaoui, Adam Burgasser, Matthew R. Burleigh, Sean J. Carey, Aleksander Chaushev, Chris M. Copperwheat, Laetitia Delrez, Catarina S. Fernandes, Daniel L. Holdsworth, Enrico J. Kotze, Valérie Van Grootel, Yaseen Almleaky, Zouhair Benkhaldoun, Pierre Magain, and Didier Queloz. Seven temperate terrestrial planets around the nearby ultracool dwarf star TRAPPIST-1. Nature, 542(7642):456–460, February 2017. doi: 10.1038/nature21360.

Sivan Ginzburg, Hilke E. Schlichting, and Re'em Sari. Core-powered mass-loss and the radius distribution of small exoplanets. MNRAS, 476(1):759–765, May 2018. doi: 10.1093/mnras/sty290.

Guillermo Gonzalez. The stellar metallicity-giant planet connection. MNRAS, 285(2):403–412, February 1997. doi: 10.1093/mnras/285.2.403.

Manuel Güdel. X-ray astronomy of stellar coronae. A&A Rev., 12(2-3):71–237, September 2004. doi: 10.1007/s00159-004-0023-2.

G. Guilluy, V. Andretta, F. Borsa, P. Giacobbe, A. Sozzetti, E. Covino, V. Bourrier, L. Fossati, A. S. Bonomo, M. Esposito, M. S. Giampapa, A. Harutyunyan, M. Rainer, M. Brogi, G. Bruno, R. Claudi, G. Frustagli, A. F. Lanza, L. Mancini, L. Pino, E. Poretti, G. Scandariato, L. Affer, C. Baffa, A. Baruffolo, S. Benatti, K. Biazzo, A. Bignamini, W. Boschin, I. Carleo, M. Cecconi, R. Cosentino, M. Damasso, S. Desidera, G. Falcini, A. F. Martinez Fiorenzano, A. Ghedina, E. González-Álvarez, J. Guerra, N. Hernandez, G. Leto, A. Maggio, L. Malavolta, J. Maldonado, G. Micela, E. Molinari, V. Nascimbeni, I. Pagano, M. Pedani, G. Piotto, and A. Reiners. The GAPS programme at TNG. XXII.

The GIARPS view of the extended helium atmosphere of HD 189733 b accounting for stellar activity. A&A, 639:A49, July 2020. doi: 10.1051/0004-6361/20203764410.48550/arXiv.2005.05676.

Akash Gupta and Hilke E. Schlichting. Sculpting the valley in the radius distribution of small exoplanets as a by-product of planet formation: the core-powered mass-loss mechanism. MNRAS, 487(1):24–33, July 2019. doi: 10.1093/mnras/stz1230.

Akash Gupta, Lorraine Nicholson, and Hilke E. Schlichting. Properties of the radius valley around low mass stars: predictions from the core-powered mass-loss mechanism. MNRAS, 516(3):4585–4593, November 2022. doi: 10.1093/mnras/stac2488.

Jacob H. Hamer and Kevin C. Schlaufman. Hot Jupiters Are Destroyed by Tides While Their Host Stars Are on the Main Sequence. AJ, 158(5):190, November 2019. doi: 10.3847/1538-3881/ab3c56.

Matthew Hansen and S. Peng Oh. Lyman α radiative transfer in a multiphase medium. MNRAS, 367(3):979–1002, April 2006. doi: 10.1111/j.1365-2966.2005.09870.x.

Laura M. Harbach, Sofia P. Moschou, Cecilia Garraffo, Jeremy J. Drake, Julián D. Alvarado-Gómez, Ofer Cohen, and Federico Fraschetti. Stellar Winds Drive Strong Variations in Exoplanet Evaporative Outflow Patterns and Transit Absorption Signatures. ApJ, 913(2):130, June 2021. doi: 10.3847/1538-4357/abf63a.

J. D. Hartman, G. Á. Bakos, L. A. Buchhave, G. Torres, D. W. Latham, G. Kovács, W. Bhatti, Z. Csubry, M. de Val-Borro, K. Penev, C. X. Huang, B. Béky, A. Bieryla, S. N. Quinn, A. W. Howard, G. W. Marcy, J. A. Johnson, H. Isaacson, D. A. Fischer, R. W. Noyes, E. Falco, G. A. Esquerdo, R. P. Knox, P. Hinz, J. Lázár, I. Papp, and P. Sári. HAT-P-57b: A Short-period Giant Planet Transiting a Bright Rapidly Rotating A8V Star Confirmed Via Doppler Tomography. AJ, 150(6):197, December 2015. doi: 10.1088/0004-6256/150/6/197.

C. Hayashi, K. Nakazawa, and Y. Nakagawa. Formation of the solar system. In D. C. Black and M. S. Matthews, editors, *Protostars and Planets II*, pages 1100–1153, January 1985.

Gregory W. Henry, Geoffrey W. Marcy, R. Paul Butler, and Steven S. Vogt. A Transiting "51 Peg-like" Planet. ApJ, 529(1):L41–L44, January 2000. doi: 10.1086/312458.

T. O. Husser, S. Wende-von Berg, S. Dreizler, D. Homeier, A. Reiners, T. Barman, and P. H. Hauschildt. A new extensive library of PHOENIX stellar atmospheres and synthetic spectra. A&A, 553:A6, May 2013. doi: 10.1051/0004-6361/201219058.

D. E. Ionov and V. I. Shematovich. Hydrogen-dominated upper atmosphere of an exoplanet: Heating by stellar radiation from soft X-rays to extreme ultraviolet. *Solar System Research*, 49(5):339–345, September 2015. doi: 10.1134/S0038094615050056.

Alan P. Jackson, Timothy A. Davis, and Peter J. Wheatley. The coronal X-ray-age relation and its implications for the evaporation of exoplanets. MNRAS, 422(3):2024–2043, May 2012. doi: 10.1111/j.1365-2966.2012.20657.x.

Brian Jackson, Emily Jensen, Sarah Peacock, Phil Arras, and Kaloyan Penev. Tidal decay and stable Roche-lobe overflow of short-period gaseous exoplanets. *Celestial Mechanics and Dynamical Astronomy*, 126(1-3):227–248, November 2016. doi: 10.1007/s10569-016-9704-1.

M. Jardine, A. Collier Cameron, J. F. Donati, S. G. Gregory, and K. Wood. X-ray emission from T Tauri stars. MNRAS, 367(3):917–927, April 2006. doi: 10.1111/j.1365-2966.2005.09995.x.

James Jeans. *The Dynamical Theory of Gases*. Cambridge Library Collection - Physical Sciences. Cambridge University Press, 4 edition, 2009. doi: 10.1017/CBO9780511694370.

Adam G. Jensen, Seth Redfield, Michael Endl, William D. Cochran, Lars Koesterke, and Travis Barman. A Detection of Hα in an Exoplanetary Exosphere. ApJ, 751(2):86, June 2012. doi: 10.1088/0004-637X/751/2/86.

John Asher Johnson, Kimberly M. Aller, Andrew W. Howard, and Justin R. Crepp. Giant Planet Occurrence in the Stellar Mass-Metallicity Plane. PASP, 122(894):905, Aug 2010. doi: 10.1086/655775.

M. L. Khodachenko, I. F. Shaikhislamov, H. Lammer, and P. A. Prokopov. Atmosphere Expansion and Mass Loss of Close-orbit Giant Exoplanets Heated by Stellar XUV. II. Effects of Planetary Magnetic Field; Structuring of Inner Magnetosphere. ApJ, 813(1):50, November 2015. doi: 10.1088/0004-637X/813/1/50.

M. L. Khodachenko, I. F. Shaikhislamov, H. Lammer, K. G. Kislyakova, L. Fossati, C. P. Johnstone, O. V. Arkhypov, A. G. Berezutsky, I. B. Miroshnichenko, and V. G. Po-

sukh. Lyα Absorption at Transits of HD 209458b: A Comparative Study of Various Mechanisms Under Different Conditions. ApJ, 847(2):126, October 2017. doi: 10.3847/1538-4357/aa88ad.

T. T. Koskinen, R. V. Yelle, P. Lavvas, and N. K. Lewis. Characterizing the Thermosphere of HD209458b with UV Transit Observations. ApJ, 723(1):116–128, November 2010. doi: 10.1088/0004-637X/723/1/116.

Yu. N. Kulikov, H. Lammer, H. I. M. Lichtenegger, N. Terada, I. Ribas, C. Kolb, D. Langmayr, R. Lundin, E. F. Guinan, S. Barabash, and H. K. Biernat. Atmospheric and water loss from early Venus. Planet. Space Sci., 54(13-14):1425–1444, November 2006. doi: 10.1016/j.pss.2006.04.021.

E. P. Kurbatov and D. V. Bisikalo. The role of atmospheric outflows in the migration of hot Jupiters. MNRAS, 506(3):3128–3137, September 2021. doi: 10.1093/mnras/stab1690.

H. Kurokawa and T. Nakamoto. Mass-loss Evolution of Close-in Exoplanets: Evaporation of Hot Jupiters and the Effect on Population. ApJ, 783(1):54, March 2014. doi: 10.1088/0004-637X/783/1/54.

A. M. Lagrange, M. Bonnefoy, G. Chauvin, D. Apai, D. Ehrenreich, A. Boccaletti, D. Gratadour, D. Rouan, D. Mouillet, S. Lacour, and M. Kasper. A Giant Planet Imaged in the Disk of the Young Star β Pictoris. *Science*, 329(5987):57, July 2010. doi: 10.1126/science.1187187.

H. Lammer, F. Selsis, I. Ribas, E. F. Guinan, S. J. Bauer, and W. W. Weiss. Atmospheric Loss of Exoplanets Resulting from Stellar X-Ray and Extreme-Ultraviolet Heating. ApJ, 598(2):L121–L124, December 2003. doi: 10.1086/380815.

Gregory Laughlin. Mining the Metal-rich Stars for Planets. ApJ, 545(2):1064–1073, December 2000. doi: 10.1086/317867.

P. Lavvas and T. Koskinen. Aerosol Properties of the Atmospheres of Extrasolar Giant Planets. ApJ, 847(1):32, September 2017. doi: 10.3847/1538-4357/aa88ce.

A. Lecavelier des Etangs, A. Vidal-Madjar, J. C. McConnell, and G. Hébrard. Atmospheric escape from hot Jupiters. A&A, 418:L1–L4, April 2004. doi: 10.1051/0004-6361:20040106.

A. Lecavelier des Etangs, V. Bourrier, P. J. Wheatley, H. Dupuy, D. Ehrenreich, A. Vidal-Madjar, G. Hébrard, G. E. Ballester, J. M. Désert, R. Ferlet, and D. K. Sing. Temporal variations in the evaporating atmosphere of the exoplanet HD 189733b. A&A, 543:L4, July 2012a. doi: 10.1051/0004-6361/201219363.

A. Lecavelier des Etangs, V. Bourrier, P. J. Wheatley, H. Dupuy, D. Ehrenreich, A. Vidal-Madjar, G. Hébrard, G. E. Ballester, J. M. Désert, R. Ferlet, and D. K. Sing. Temporal variations in the evaporating atmosphere of the exoplanet HD 189733b. A&A, 543:L4, July 2012b. doi: 10.1051/0004-6361/201219363.

M. Leitzinger, P. Odert, R. Greimel, H. Korhonen, E. W. Guenther, A. Hanslmeier, H. Lammer, and M. L. Khodachenko. A search for flares and mass ejections on young late-type stars in the open cluster Blanco-1. MNRAS, 443(1):898–910, September 2014. doi: 10.1093/mnras/stu1161.

Michael B. Lund, Joseph E. Rodriguez, George Zhou, B. Scott Gaudi, Keivan G. Stassun, Marshall C. Johnson, Allyson Bieryla, Ryan J. Oelkers, Daniel J. Stevens, Karen A. Collins, Kaloyan Penev, Samuel N. Quinn, David W. Latham, Jr. Villanueva, Steven, Jason D. Eastman, John F. Kielkopf, Thomas E. Oberst, Eric L. N. Jensen, David H. Cohen, Michael D. Joner, Denise C. Stephens, Howard Relles, Giorgio Corfini, Joao Gregorio, Roberto Zambelli, Gilbert A. Esquerdo, Michael L. Calkins, Perry Berlind, David R. Ciardi, Courtney Dressing, Rahul Patel, Patrick Gagnon, Erica Gonzales, Thomas G. Beatty, Robert J. Siverd, Jonathan Labadie-Bartz, Rudolf B. Kuhn, Knicole D. Colón, David James, Joshua Pepper, Benjamin J. Fulton, Kim K. McLeod, Christopher Stockdale, Sebastiano Calchi Novati, D. L. DePoy, Andrew Gould, Jennifer L. Marshall, Mark Trueblood, Patricia Trueblood, John A. Johnson, Jason Wright, Nate McCrady, Robert A. Wittenmyer, Samson A. Johnson, Anthony Sergi, Maurice Wilson, and David H. Sliski. KELT-20b: A Giant Planet with a Period of P $\sim$ 3.5 days Transiting the V $\sim$ 7.6 Early A Star HD 185603. AJ, 154(5):194, November 2017. doi: 10.3847/1538-3881/aa8f95.

Hiroyuki Maehara, Yuta Notsu, Shota Notsu, Kosuke Namekata, Satoshi Honda, Takako T. Ishii, Daisaku Nogami, and Kazunari Shibata. Starspot activity and superflares on solar-type stars. PASJ, 69(3):41, June 2017. doi: 10.1093/pasj/psx013.

Titos Matsakos, Ana Uribe, and Arieh Königl. Classification of magnetized star-planet

interactions: bow shocks, tails, and inspiraling flows. A&A, 578:A6, June 2015. doi: 10.1051/0004-6361/201425593.

Michel Mayor and Didier Queloz. A Jupiter-mass companion to a solar-type star. Nature, 378(6555):355–359, Nov 1995. doi: 10.1038/378355a0.

T. Mazeh, T. Holczer, and S. Faigler. Dearth of short-period Neptunian exoplanets: A desert in period-mass and period-radius planes. A&A, 589:A75, May 2016. doi: 10.1051/0004-6361/201528065.

John McCann, Ruth A. Murray-Clay, Kaitlin Kratter, and Mark R. Krumholz. Morphology of Hydrodynamic Winds: A Study of Planetary Winds in Stellar Environments. ApJ, 873(1):89, March 2019. doi: 10.3847/1538-4357/ab05b8.

E. R. Micelotta, A. P. Jones, and A. G. G. M. Tielens. Polycyclic aromatic hydrocarbon processing in a hot gas. A&A, 510:A37, Feb 2010. doi: 10.1051/0004-6361/200911683.

A. Mignone, G. Bodo, S. Massaglia, T. Matsakos, O. Tesileanu, C. Zanni, and A. Ferrari. PLUTO: A Numerical Code for Computational Astrophysics. ApJS, 170(1):228–242, May 2007. doi: 10.1086/513316.

Dimitri Mihalas. *Stellar atmospheres*. 1978.

Hiroto Mitani, Riouhei Nakatani, and Naoki Yoshida. Atmospheric Escape of Close-in Giants around Hot Stars: Far-Ultraviolet Radiation and Photoelectric Heating Effect. *arXiv e-prints*, art. arXiv:2005.08676, May 2020.

Hiroto Mitani, Riouhei Nakatani, and Naoki Yoshida. Stellar wind effect on the atmospheric escape of hot Jupiters and their Ly α and H α transits. MNRAS, 512(1):855–860, May 2022. doi: 10.1093/mnras/stac556.

Caroline V. Morley, Jonathan J. Fortney, Mark S. Marley, Channon Visscher, Didier Saumon, and S. K. Leggett. Neglected Clouds in T and Y Dwarf Atmospheres. ApJ, 756(2):172, September 2012. doi: 10.1088/0004-637X/756/2/172.

A. Mortier, N. C. Santos, S. Sousa, G. Israelian, M. Mayor, and S. Udry. On the functional form of the metallicity-giant planet correlation. A&A, 551:A112, March 2013. doi: 10.1051/0004-6361/201220707.

Alessandro Munafò, Nagi N. Mansour, and Marco Panesi. A Reduced-order NLTE Kinetic Model for Radiating Plasmas of Outer Envelopes of Stellar Atmospheres. ApJ, 838(2): 126, April 2017. doi: 10.3847/1538-4357/aa602e.

Ruth A. Murray-Clay, Eugene I. Chiang, and Norman Murray. Atmospheric Escape From Hot Jupiters. ApJ, 693(1):23–42, Mar 2009. doi: 10.1088/0004-637X/693/1/23.

Riouhei Nakatani, Takashi Hosokawa, Naoki Yoshida, Hideko Nomura, and Rolf Kuiper. Radiation Hydrodynamics Simulations of Photoevaporation of Protoplanetary Disks by Ultraviolet Radiation: Metallicity Dependence. ApJ, 857(1):57, Apr 2018a. doi: 10.3847/1538-4357/aab70b.

Riouhei Nakatani, Takashi Hosokawa, Naoki Yoshida, Hideko Nomura, and Rolf Kuiper. Radiation Hydrodynamics Simulations of Photoevaporation of Protoplanetary Disks. II. Metallicity Dependence of UV and X-Ray Photoevaporation. ApJ, 865(1):75, Sep 2018b. doi: 10.3847/1538-4357/aad9fd.

Riouhei Nakatani, Anastasia Fialkov, and Naoki Yoshida. Photoevaporation of Minihalos During Cosmic Reionization: Primordial and Metal-enriched Halos. ApJ, 905(2):151, December 2020. doi: 10.3847/1538-4357/abc5b4.

Joe P. Ninan, Gudmundur Stefansson, Suvrath Mahadevan, Chad Bender, Paul Robertson, Lawrence Ramsey, Ryan Terrien, Jason Wright, Scott A. Diddams, Shubham Kanodia, William Cochran, Michael Endl, Eric B. Ford, Connor Fredrick, Samuel Halverson, Fred Hearty, Jeff Jennings, Kyle Kaplan, Emily Lubar, Andrew J. Metcalf, Andrew Monson, Colin Nitroy, Arpita Roy, and Christian Schwab. Evidence for He I 10830 Å Absorption during the Transit of a Warm Neptune around the M-dwarf GJ 3470 with the Habitable-zone Planet Finder. ApJ, 894(2):97, May 2020. doi: 10.3847/1538-4357/ab855910.48550/arXiv.1910.02070.

Shohei Nishimoto, Kyoko Watanabe, Shinsuke Imada, Tomoko Kawate, and Kyoung-Sun Lee. Statistical and Observational Research on Solar Flare EUV Spectra and Geometrical Features. ApJ, 904(1):31, November 2020. doi: 10.3847/1538-4357/abbacb.

D. W. Norcross. Photoionization of the He metastable states. *Journal of Physics B Atomic Molecular Physics*, 4(5):652–657, May 1971. doi: 10.1088/0022-3700/4/5/006.

Lisa Nortmann, Enric Pallé, Michael Salz, Jorge Sanz-Forcada, Evangelos Nagel, F. Javier Alonso-Floriano, Stefan Czesla, Fei Yan, Guo Chen, Ignas A. G. Snellen, Mathias Zech-

meister, Jürgen H. M. M. Schmitt, Manuel López-Puertas, Núria Casasayas-Barris, Florian F. Bauer, Pedro J. Amado, José A. Caballero, Stefan Dreizler, Thomas Henning, Manuel Lampón, David Montes, Karan Molaverdikhani, Andreas Quirrenbach, Ansgar Reiners, Ignasi Ribas, Alejandro Sánchez-López, P. Christian Schneider, and María R. Zapatero Osorio. Ground-based detection of an extended helium atmosphere in the Saturn-mass exoplanet WASP-69b. *Science*, 362(6421):1388–1391, December 2018. doi: 10.1126/science.aat5348.

P. Odert, N. V. Erkaev, K. G. Kislyakova, H. Lammer, A. V. Mezentsev, V. A. Ivanov, L. Fossati, M. Leitzinger, D. Kubyshkina, and M. Holmström. Modeling the Lyα transit absorption of the hot Jupiter HD 189733b. A&A, 638:A49, June 2020. doi: 10.1051/0004-6361/201834814.

Antonija Oklopčić and Christopher M. Hirata. A New Window into Escaping Exoplanet Atmospheres: 10830 Å Line of Helium. ApJ, 855(1):L11, March 2018. doi: 10.3847/2041-8213/aaada9.

Donald E. Osterbrock and Gary J. Ferland. *Astrophysics of gaseous nebulae and active galactic nuclei*. 2006.

James E. Owen. Atmospheric Escape and the Evolution of Close-In Exoplanets. *Annual Review of Earth and Planetary Sciences*, 47:67–90, May 2019. doi: 10.1146/annurev-earth-053018-060246.

James E. Owen and Fred C. Adams. Magnetically controlled mass-loss from extrasolar planets in close orbits. MNRAS, 444(4):3761–3779, Nov 2014. doi: 10.1093/mnras/stu1684.

James E. Owen and Alan P. Jackson. Planetary evaporation by UV and X-ray radiation: basic hydrodynamics. *Monthly Notices of the Royal Astronomical Society*, 425(4):2931–2947, 10 2012. ISSN 0035-8711. doi: 10.1111/j.1365-2966.2012.21481.x.

James E. Owen and Yanqin Wu. Kepler Planets: A Tale of Evaporation. ApJ, 775(2):105, October 2013. doi: 10.1088/0004-637X/775/2/105.

James E. Owen and Yanqin Wu. The Evaporation Valley in the Kepler Planets. ApJ, 847(1):29, Sep 2017. doi: 10.3847/1538-4357/aa890a.

E. Palle, L. Nortmann, N. Casasayas-Barris, M. Lampón, M. López-Puertas, J. A. Caballero, J. Sanz-Forcada, L. M. Lara, E. Nagel, F. Yan, F. J. Alonso-Floriano, P. J. Amado, G. Chen, C. Cifuentes, M. Cortés-Contreras, S. Czesla, K. Molaverdikhani, D. Montes, V. M. Passegger, A. Quirrenbach, A. Reiners, I. Ribas, A. Sánchez-López, A. Schweitzer, M. Stangret, M. R. Zapatero Osorio, and M. Zechmeister. A He I upper atmosphere around the warm Neptune GJ 3470 b. A&A, 638:A61, June 2020. doi: 10.1051/0004-6361/20203771910.48550/arXiv.2004.12812.

John C. B. Papaloizou and Caroline Terquem. Planet formation and migration. *Reports on Progress in Physics*, 69(1):119–180, January 2006. doi: 10.1088/0034-4885/69/1/R03.

E. N. Parker. Dynamics of the Interplanetary Gas and Magnetic Fields. ApJ, 128:664, November 1958. doi: 10.1086/146579.

J. E. Pringle. Accretion discs in astrophysics. ARA&A, 19:137–162, January 1981. doi: 10.1146/annurev.aa.19.090181.001033.

Keighley E. Rockcliffe, Elisabeth R. Newton, Allison Youngblood, Vincent Bourrier, Andrew W. Mann, Zachory Berta-Thompson, Marcel A. Agüeros, Alejandro Núñez, and David Charbonneau. A Lyα Transit Left Undetected: the Environment and Atmospheric Behavior of K2-25b. AJ, 162(3):116, September 2021. doi: 10.3847/1538-3881/ac126f.

Fernando Santoro and J. Michael Shull. Critical Metallicity and Fine-Structure Emission of Primordial Gas Enriched by the First Stars. ApJ, 643(1):26–37, May 2006. doi: 10.1086/501518.

J. Sanz-Forcada, G. Micela, I. Ribas, A. M. T. Pollock, C. Eiroa, A. Velasco, E. Solano, and D. García-Álvarez. Estimation of the XUV radiation onto close planets and their evaporation. A&A, 532:A6, Aug 2011. doi: 10.1051/0004-6361/201116594.

E. M. Schneiter, A. Esquivel, C. S. Villarreal D'Angelo, P. F. Velázquez, A. C. Raga, and A. Costa. Photoionization of planetary winds: case study HD 209458b. MNRAS, 457 (2):1666–1674, April 2016. doi: 10.1093/mnras/stw076.

Sara Seager and Drake Deming. Exoplanet Atmospheres. ARA&A, 48:631–672, September 2010. doi: 10.1146/annurev-astro-081309-130837.

I. F. Shaikhislamov, M. L. Khodachenko, H. Lammer, K. G. Kislyakova, L. Fossati, C. P. Johnstone, P. A. Prokopov, A. G. Berezutsky, Yu. P. Zakharov, and V. G. Posukh. Two

Regimes of Interaction of a Hot Jupiter's Escaping Atmosphere with the Stellar Wind and Generation of Energized Atomic Hydrogen Corona. ApJ, 832(2):173, December 2016. doi: 10.3847/0004-637X/832/2/173.

Lyman Spitzer. *Physical processes in the interstellar medium*. 1978. doi: 10.1002/9783527617722.

P. J. Storey and D. G. Hummer. Recombination line intensities for hydrogenic ions-IV. Total recombination coefficients and machine-readable tables for Z=1 to 8. MNRAS, 272(1):41–48, January 1995. doi: 10.1093/mnras/272.1.41.

Gy M. Szabó and Sz Kálmán. The sub-Jupiter/Neptune desert of exoplanets: parameter dependent boundaries and implications on planet formation. MNRAS, 485(1):L116–L120, May 2019. doi: 10.1093/mnrasl/slz036.

Gy. M. Szabó and L. L. Kiss. A Short-period Censor of Sub-Jupiter Mass Exoplanets with Low Density. ApJ, 727(2):L44, Feb 2011. doi: 10.1088/2041-8205/727/2/L44.

Feng Tian. Atmospheric Escape from Solar System Terrestrial Planets and Exoplanets. *Annual Review of Earth and Planetary Sciences*, 43:459–476, May 2015. doi: 10.1146/annurev-earth-060313-054834.

George B. Trammell, Zhi-Yun Li, and Phil Arras. Magnetohydrodynamic Simulations of Hot Jupiter Upper Atmospheres. ApJ, 788(2):161, June 2014. doi: 10.1088/0004-637X/788/2/161.

Pascal Tremblin and Eugene Chiang. Colliding planetary and stellar winds: charge exchange and transit spectroscopy in neutral hydrogen. MNRAS, 428(3):2565–2576, Jan 2013. doi: 10.1093/mnras/sts212.

Anjali Tripathi, Kaitlin M. Kratter, Ruth A. Murray-Clay, and Mark R. Krumholz. Simulated Photoevaporative Mass Loss from Hot Jupiters in 3D. ApJ, 808(2):173, Aug 2015. doi: 10.1088/0004-637X/808/2/173.

A. Vidal-Madjar, A. Lecavelier des Etangs, J. M. Désert, G. E. Ballester, R. Ferlet, G. Hébrard, and M. Mayor. An extended upper atmosphere around the extrasolar planet HD209458b. Nature, 422(6928):143–146, Mar 2003. doi: 10.1038/nature01448.

A. Vidal-Madjar, J. M. Désert, A. Lecavelier des Etangs, G. Hébrard, G. E. Ballester, D. Ehrenreich, R. Ferlet, J. C. McConnell, M. Mayor, and C. D. Parkinson. Detection

of Oxygen and Carbon in the Hydrodynamically Escaping Atmosphere of the Extrasolar Planet HD 209458b. ApJ, 604(1):L69–L72, Mar 2004. doi: 10.1086/383347.

A. A. Vidotto and A. Cleary. Stellar wind effects on the atmospheres of close-in giants: a possible reduction in escape instead of increased erosion. MNRAS, 494(2):2417–2428, May 2020. doi: 10.1093/mnras/staa852.

C. Villarreal D'Angelo, M. Schneiter, A. Costa, P. Velázquez, A. Raga, and A. Esquivel. On the sensitivity of extrasolar mass-loss rate ranges: HD 209458b a case study. MNRAS, 438(2):1654–1662, February 2014. doi: 10.1093/mnras/stt2303.

Carolina Villarreal D'Angelo, Alejandro Esquivel, Matías Schneiter, and Mario Agustín Sgró. Magnetized winds and their influence in the escaping upper atmosphere of HD 209458b. MNRAS, 479(3):3115–3125, September 2018. doi: 10.1093/mnras/sty1544.

Carolina Villarreal D'Angelo, Aline A. Vidotto, Alejandro Esquivel, Gopal Hazra, and Allison Youngblood. GJ 436b and the stellar wind interaction: simulations constraints using Ly α and H α transits. MNRAS, 501(3):4383–4395, March 2021. doi: 10.1093/mnras/staa3867.

A. J. Watson, T. M. Donahue, and J. C. G. Walker. The dynamics of a rapidly escaping atmosphere: Applications to the evolution of Earth and Venus. Icarus, 48(2):150–166, November 1981. doi: 10.1016/0019-1035(81)90101-9.

F. Yan, A. Wyttenbach, N. Casasayas-Barris, A. Reiners, E. Pallé, Th. Henning, P. Mollière, S. Czesla, L. Nortmann, K. Molaverdikhani, G. Chen, I. A. G. Snellen, M. Zechmeister, C. Huang, I. Ribas, A. Quirrenbach, J. A. Caballero, P. J. Amado, D. Cont, S. Khalafinejad, J. Khaimova, M. López-Puertas, D. Montes, E. Nagel, M. Oshagh, S. Pedraz, and M. Stangret. Detection of the hydrogen Balmer lines in the ultra-hot Jupiter WASP-33b. A&A, 645:A22, January 2021. doi: 10.1051/0004-6361/20203930210.48550/arXiv.2011.07888.

Fei Yan and Thomas Henning. An extended hydrogen envelope of the extremely hot giant exoplanet KELT-9b. *Nature Astronomy*, 2:714–718, Jul 2018. doi: 10.1038/s41550-018-0503-3.

Roger V. Yelle. Aeronomy of extra-solar giant planets at small orbital distances. Icarus, 170(1):167–179, Jul 2004. doi: 10.1016/j.icarus.2004.02.008.

Michael Zhang, Heather A. Knutson, Lile Wang, Fei Dai, Leonardo A. dos Santos, Luca Fossati, Gregory W. Henry, David Ehrenreich, Yann Alibert, Sergio Hoyer, Thomas G. Wilson, and Andrea Bonfanti. Detection of Ongoing Mass Loss from HD 63433c, a Young Mini Neptune. *arXiv e-prints*, art. arXiv:2106.05273, June 2021.